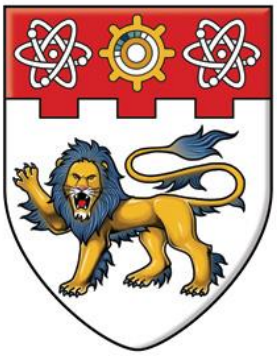

NANYANG TECHNOLOGICAL UNIVERSITY

Thermal Energy Storage by Phase Change Materials in Power Generation

QIN ZHEN

SCHOOL OF MECHANICAL & AEROSPACE ENGINEERING

2016

Thermal Energy Storage by Phase Change Materials in Power Generation

Qin Zhen

School of Mechanical & Aerospace Engineering

A thesis submitted to Nanyang Technological University

in fulfillment of the requirement for the degree of

Master of Engineering

2016

Abstract

Thermal energy storage (TES) is seen as a feasible solution to the energy crisis in the 21st century. This study focuses on the development of a TES unit with PCMs employed in a power cogeneration cycle. Firstly, the thermal analysis of some suitable PCMs were conducted through the differential scanning calorimetry (DSC) technique and the T-history method. Some disagreement was found between their measurement results and the possible reasons were discussed. Besides, it was found that eutectic salts or salts were suitable PCMs to be applied in the temperature range of 200~300 ^{o}C. Secondly, one TES unit with paraffin wax as the PCM was constructed and tested in the laboratory. Three groups of the fan speeds and two groups of the heater power were set and the temperature of the PCM was observed in the two chambers B and D. It was found that at the lower fan speed and the higher heater power working conditions, the PCM would melt faster, and thus achieve a higher TES performance. Thirdly, the Two-D and Three-D time-dependent numerical simulations of the TES unit were conducted in COMSOL Multi-physics. The Three-D simulation counted in the natural convection inside the liquid PCM and was found closer to the experiments. The "sudden jump" of temperature at the end of the PCM melting was successfully simulated. Lastly, a TES unit final design was given and one design with selected parameters was built in COMSOL and numerically simulated. The effects of the gas and oil inlet mass flow rates were evaluated. It was found that the gas inlet mass flow rate has a higher influence on the PCM melting fraction in the steady working condition. In the future work, a more detailed numerical analysis will be done on the aspects of the melting time, the instantaneous heat transfer rate and the charging time needed based on a series of time dependent studies. The PCM conductivity enhancement ways such as adding fins will also be considered in the investigation.

Acknowledgement

During my master's degree study, many people have helped me in one way or another. I would like to express my sincere thanks to them.

Firstly, I would like to thank my supervisor, Dr. Fei Duan, for his consistent guidance, instruction and encouragement. Without his help, my research and personal life would have much reduced quality. His passion about life and work affects me so deeply and his creative thoughts always inspire me with new research ideas.

Secondly, I would like to thank Associate Professor Deng Hongwu from Beihang University (the visiting scholar in NTU) for his valuable advice and guidance to my research. I would also like to thank Dr. Dubey, Dr. Qiu Lu, Dr. Wang Kai, Dr. Ji Chenzhen, Dr. Huang Yi, Dr. Yan Zhibin, Dr. Tong Wei and Dr. Jiao Yanmei for their constantly giving me advice and encouragement. Their friendship is one of the most valuable treasures I got in Singapore.

Thanks also to Dr. He Bin and Miss. Zhong Xin, their kind help through the two years makes me feel accompany and determined. Besides, thanks Mr. Chew Jing Yong and Mr. Jeremy Toh Wei Hong, the previous final year project (FYP) students for their contributions to the experiments.

Furthermore, I am grateful to Mr. Roger Lee Keng Yuen, Mr. Lawrence Ang Koon Teck, Mr. Edward Yeo Boon Chuan, the technicians in the Energy System (ES) Laboratory, for their technical support for a long time.

Special thanks my families, though not around, I can still strongly feel their support. Their love means a lot to me and encourages me to chase my dream.

Last but not least, I would like to thank EMA for their financial support of this research project.

Table of Contents

List of Figures

List of Tables

List of Symbols

A	Duct area, [m^2]
h	Convective heat transfer coefficient, [W/m^2 K]
k	Thermal conductivity, [W/m K]
u	Air velocity, [m/s]
L	Latent heat, [J/kg]
C_p	Specific heat, [J/kg K]
$\dot{m}$	Mass flow rate, [kg/s]
q	Heat transfer rate, [W]
P	Heater power, [W]
Ste	Stefan number, $Ste = \frac{C_p \Delta T}{L}$
T	Temperature, [℃]
$\dot{Q}$	Instantaneous heat transfer rate, [W]
g	Gravity acceleration, 9.8 m/s^2

Greek symbols

α	Thermal diffusivity, [m^2/s]
μ	Dynamic viscosity of fluid, [kg/m s]
ρ	Density, [kg/m^3]
υ	Kinematic viscosity, [m^2/s]

Subscripts

Al	aluminum
CSP	Concentrating solar power plant
DSC	Differential Scanning Calorimetry

HTF	heat transfer fluid
in	inlet
out	outlet
PCM	phase change material
TES	thermal energy storage
TGA	Thermo-gravimetric Analysis
gas	Hot exhaust gas
oil	Heat transfer oil
perchamber	Per PCM chamber

Note: symbols not listed here are either self-explanatory or explained in the context.

Chapter 1: Introduction

1.1 Research Background

In the 21st century, energy crisis has been a serious problem of human beings [1]. The rapid developing industry consumes the earth's natural resources like coal, fossil oil, natural gases at a fast speed. Considering their limited stock, it is meaningful and essential to improve the current energy usage efficiency. While an emerging energy saving way is to use thermal energy storage (TES) with phase change materials (PCMs) to recover waste heat.

As one of the main energy consumers, the power plants burn the fuel to generate electricity in the same way as can produce the high-temperature exhaust gas. The heat recovery from the exhaust gas has a great meaning to improve the power plants' energy usage efficiency, which is a popular research filed in contemporary. Nowadays, the power cogeneration with the waste heat of exhaust gas is a common practice in plants.

In a common thermal power plant cycle, as called gas turbine combined cycle, the gas turbine generates electricity by natural gas combustion. Then, the steam turbine generates electricity by recovering the heat of the exhaust gas emitted by the gas turbine with the help of a heat exchanger. Figure 1.1 presents a diagram of gas turbine combined cycle [2].

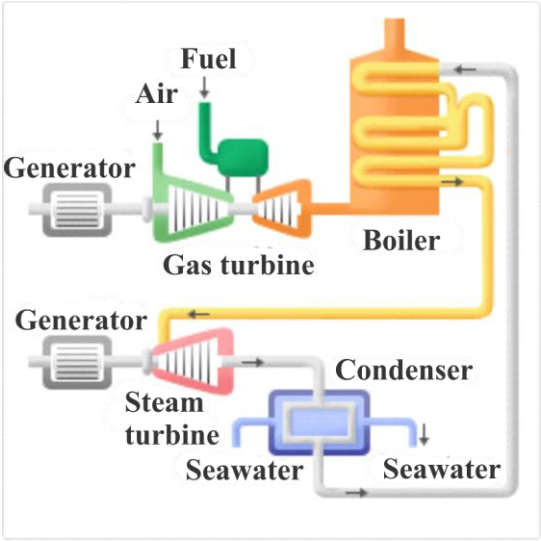

Figure 1.1: Gas turbine combined cycle [2]

Recently, a new power cogeneration cycle has been proposed by combining the gas turbine and Stirling engine linked by a PCM storage tank. The diagram of this innovative hybrid power cogeneration cycle is shown in Figure 1.2. The application of the TES tank in this cycle not only helps recover the waste heat of exhaust gas, but also provides a stable heat source for the Stirling engine.

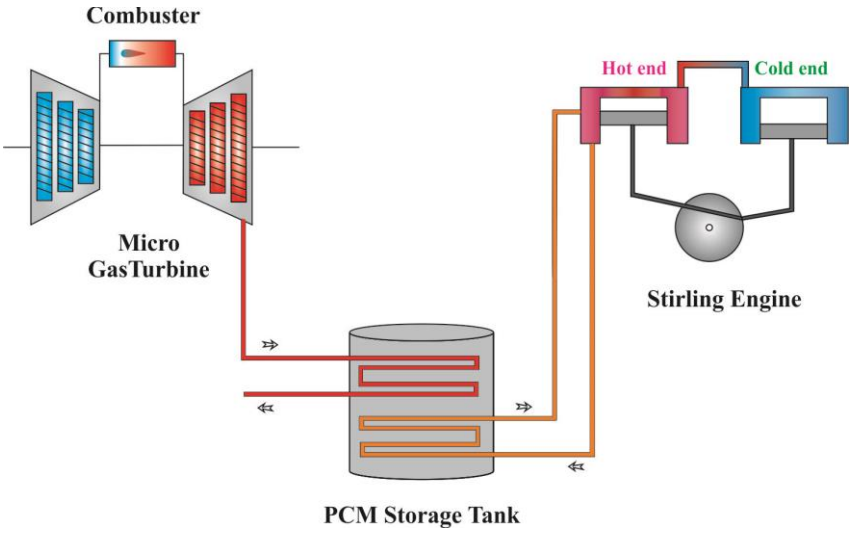

Figure 1.2: The gas turbine and Stirling engine power cogeneration cycle [3]

When involving the TES technology, it is interesting to compare its three branches: sensible heat storage, latent heat storage, and chemical heat storage. Among them, latent heat storage is more widely used because of its large heat storage capacity and low operation requirements. Different from chemical heat storage, latent heat storage involves no chemical reaction, which makes it more safe to be applied. Comparing to use sensible storage materials, the usage of PCMs not only reduces the TES tank volume, but also can smooth the temperature distribution inside the tank with the latent heat during the melting and freezing of the PCM [4].

The TES with PCMs has always been a research hot topic in energy field. Starting from the cold storage with ice, researchers have tried to utilize the materials' latent heat. In nowadays, the TES with PCMs has been widely applied in various industries. Although the TES with PCM technique has had a great development so far, there are still some aspects under developing. For instance, the middle high temperature PCMs, the TES unit that can charge and discharge at same time are two areas in course of development.

1.2 Research Objectives and Scope

Although many efforts have been devoted to the study of the TES systems, as reviewed in Chapter 2, the research is not complete due to the complexity of the TES configurations and the application scenarios, especially the TES unit with PCMs that can charge and discharge at the same time and the corresponding design methodology and the heat transfer characteristics. Currently this aspect of study is not fully developed. This study focuses on the design of a middle high temperature TES unit with PCMs that can be applied to gas turbine and Stirling engine cogeneration cycle, and the heat transfer behaviors prediction of the TES unit with PCMs during the charging and discharging.

To facilitate the study, some PCMs and their thermal properties will be investigated firstly through two popular methods: the differential scanning calorimetry (DSC) and the T-history method. A comparative study will be carried out between the two methods. The difference between the measurement results of the two methods will be explained.

To carry the PCMs for the TES, a proper and effective heat exchanger will be proposed. As a preliminary study and also a validation case for the numerical model, a simple TES unit will be constructed and tested in the laboratory.

Afterwards, a numerical simulation based on the experiments will be conducted and its results will be compared with the experiment results in order to verify the numerical model.

With the verification of the numerical model, the simulation tool can be applied in the evaluation of the final heat exchanger design. The modified opinions will be addressed based on the gas flow filed and the heat transfer performance.

1.3 Layout of Thesis

The thesis is organized in a way that comprises the investigation sequences and the underlying logic. The thesis is divided into 7 chapters in total and the description of the respective chapters is as follows.

Close behind the general introduction in Chapter 1, Chapter 2 reports the literature review about previous work related to the TES with PCMs. Starting from the introduction to the energy storage technique, the review chapter firstly introduces the new developments associated with middle high temperature materials and the new thermal properties characterization method: the T-history method. Whereafter some relevant TES experiments are reviewed. Also, some

numerical investigation studies are presented for reference. Besides, the current applications of the TES in power generation are briefly introduced.

Chapter 3 discusses the materials properties test for the Selected PCMs. Proper PCMs are proposed for the project usage. The results difference of two similar methods for same PCM are discussed and explained.

Chapter 4 presents a preliminary study related to a simple TES unit for hot air heat collection. Its thermal energy storage performance is investigated and the effects of several parameters, such as the fan speed and the heater power are considered. The results are analyzed and the structural improvement opinions are given based on the test results.

Following the experimental study in Chapter 4, Chapter 5 gives a numerical simulation study based on the experiments. The numerical model is validated with the experiments data. A 2D study and a 3D study are carried out in order. The heat transfer process of PCMs during melting is explained based on the numerical simulation results.

In Chapter 6, a design of the final TES system is proposed and the heat exchanger is evaluated with a numerical simulation. The flow field and heat transfer characteristics are studied based the simulation.

Finally, Chapter 7 summarizes current work and proposes recommendations for future studies.

Chapter 2: Literature Review

The present review includes: (i) basic development of energy storage technology, (ii) phase change materials used in the thermal energy storage, (iii) numerical modelling of phase change heat transfer, (iv) experimental work related to TES system, (v) application of TES systems.

2.1 Energy Storage Technology

Since the discovery of electricity, people have sought effective methods to store energy for use on demand. Energy storage systems provide a wide array of technology approaches to manage the power supply in order to create a more resilient energy infrastructure and bring cost savings to utilities and consumers. Figure 2.1 shows different kinds of energy storage systems that are under development. In power generation aspect, TES with PCM is one of the best ways to be applied [1].

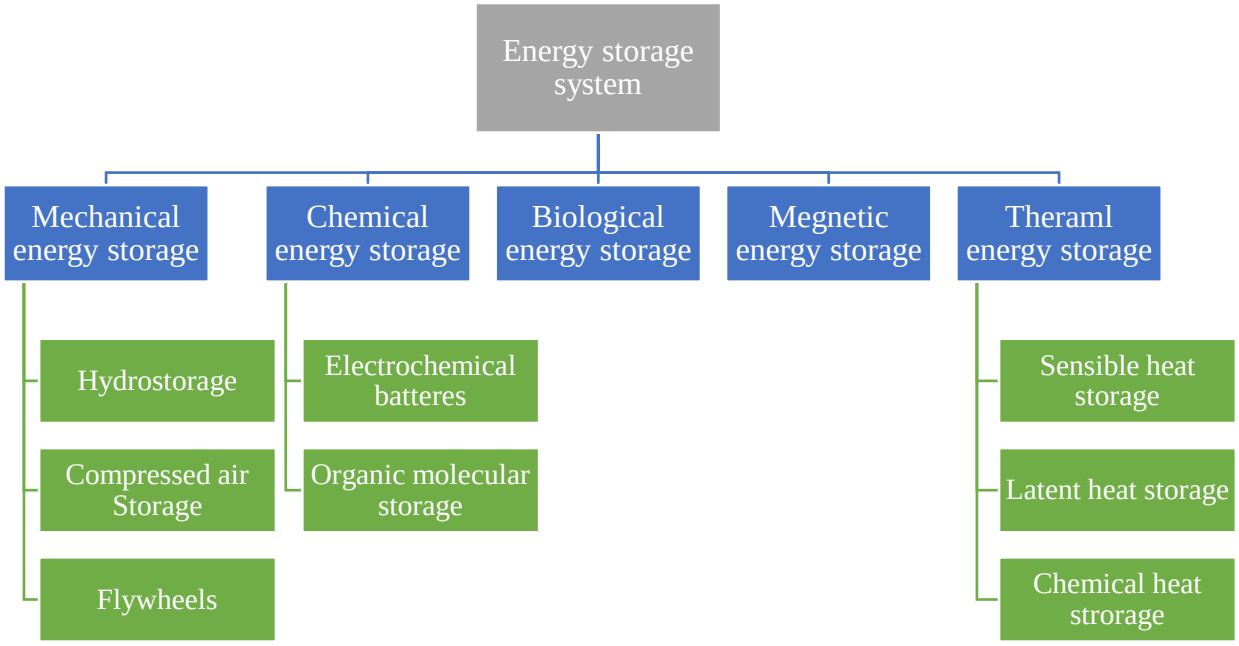

Figure 2.1: Classification of energy storage systems [1]

The TES system has the potential of increasing the effective use of thermal energy equipment and of facilitating large-scale switching. They are normally useful for correcting the mismatch between the supply and demand of energy. There are mainly two types of thermal energy storage systems, sensible storage systems and latent storage systems. Latent storage systems always come with phase change. Several facts have to be considered when deciding on the type and the design of any thermal storage system. A key issue in the design of a thermal energy storage system is its thermal capacity. However, selection of the appropriate system depends on many cost-benefit considerations, technical criteria and environmental criteria.

Thermal energy can be stored nearly isothermally in some substances as the latent heat of phase change and substances used under this technology are called PCM [5]. Storage systems utilizing PCMs can reduce system size compared to single-phase sensible heating systems. However, heat transfer design and media selection are more difficult, and experience with low temperature salts has shown that the performance of the materials can degrade after moderate number of freeze-melt cycles [4].

2.2 Phase Change Materials

2.2.1 Middle High Temperature PCMs

Solid-liquid PCMs are considered to be efficient alternative to sensible thermal energy storage materials. As shown in Figure 2.2, compared to sensible materials, PCM operates at small temperature differences between charging and discharging. Furthermore, these latent heat storages have higher energy densities compared to sensible heat storages [6].

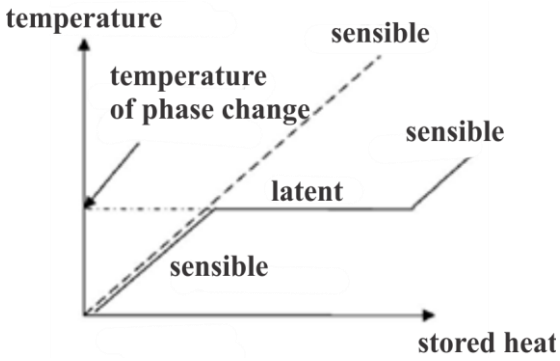

Figure 2.2: Phase change temperature profile of PCM [1]

Figure 2.3 shows the materials family that can be used as PCM in thermal energy storage [6].

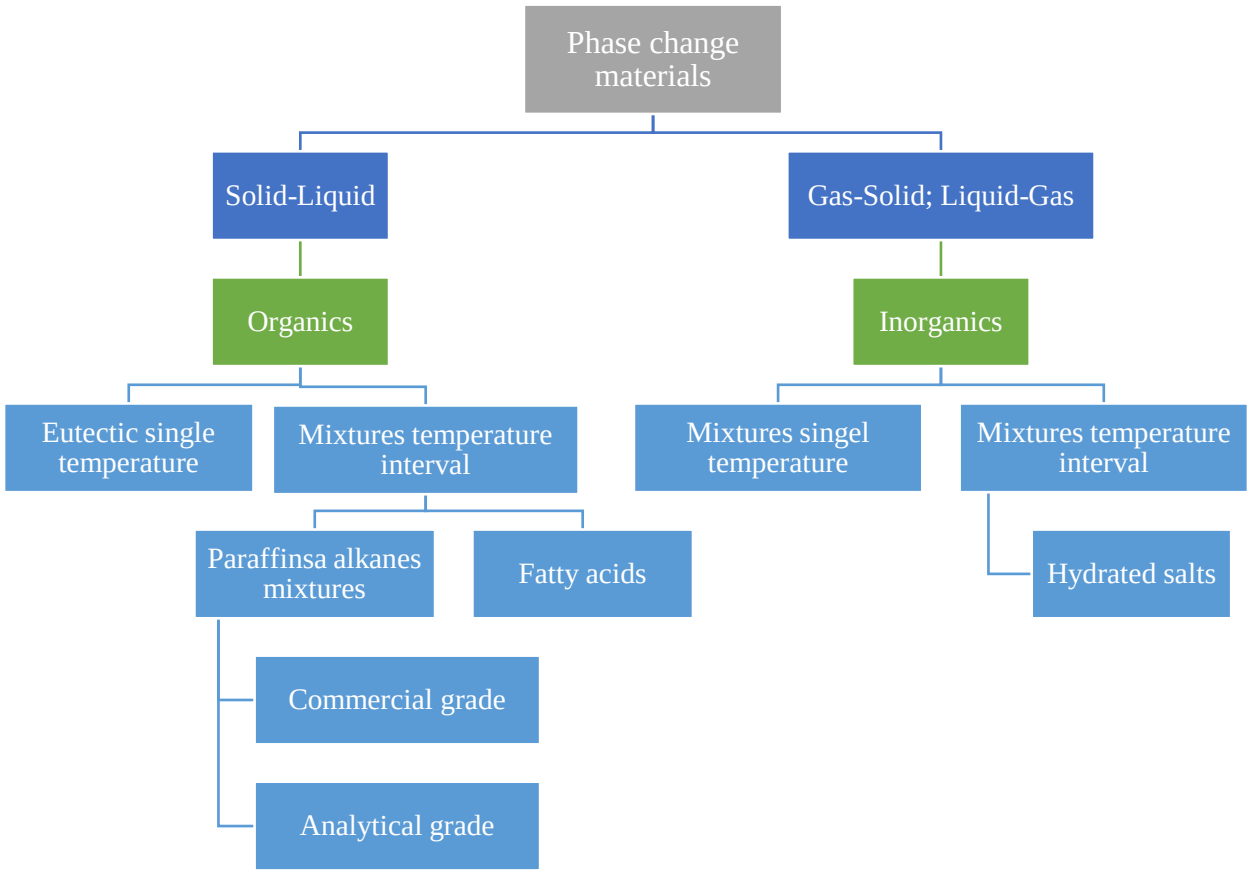

Figure 2.3: Classification of latent heat materials, with phase change solid-liquid [6]

In this thesis, In this thesis, the high temperature is defined as the tempreature range between 100~300 ℃. Many researchers summarized current commercial PCM in this temperature range. Gil et al. summarized current commercially available PCMs, as listed in Table 2.1 and the potential PCMs, as shown in Table 2.2. These tables contain their main thermal properties [5].

Table 2.1: Current commercial PCM materials [5]

Name	Type	Manufacturer	Phase change temperature (℃)	Density (kg/m^3)	Latent heat (kJ/kg)	Specific heat (kJ/kg·K)	Thermal conductivity (W/m·K)
RT110	Paraffin	Rubitherm	112	n.a.	213	n.a.	n.a.
E117	Inorganic	EPS	117	1450	169	2.61	0.70
A164	Organic	EPS	164	1500	306	n.a.	n.a.

Note: n.a.: Not available.

Molten salt is one common kind of PCMs applied in the power generation, especially in thermal power generation like solar power plant. Many researchers have done researches related to molten as PCMs for power generation.

Herrmann et al. made an economic analysis about using molten salt as PCMs in power generation. They found that the inorganic nitrate salt mixtures were proper storage materials for power plant. Because the salts offer a favorable density, which is around 1880 kg/m^3, and specific heat, around 1.5 kJ/kg·K, chemical reactivity, which is very low, and a low vapor pressure and low cost, for 0.4~0.9 USD/kg [7].

Table 2.2: Organic materials with potential use as PCM [5]

Compound	Melting temperature (℃)	Heat of fusion(kJ/kg)	Heat of fusion(kJ/L)
Isomalt $((C_{12}H_{24}O_{11}\cdot 2H_2O)+(C_{12}H_{24}O_{11}))$	147	275	n.a.
Adipic acid	152	247	n.a.
Dimethylol propionic acid	153	275	n.a.
Pentaerythritol	187	255	n.a.
AMPL $((NH_2)(CH_3)C(CH_2OH)_2)$	112	28.5	2991.4
TRIS $(NH_2)(CH_3)C(CH_2OH)_3$	172	27.6	3340 kJ/kmol
NPG $((CH_3)_2C(CH_2OH)_2)$	126	44.3	4602.4 kJ/kmol
PE $(C(CH_2OH)_4)$	260	36.9	5020 kJ/kmol

Note: n.a.: Not available.

Wang introduced the melting point of individual nitrate salts and multi-component nitrate systems, as shown in Table 2.3 [8]. One of the common PCMs in the solar power generation is solar salt, which is the mixture of $NaNO_3$ and KNO_3 at weight ratio 6:4, and has the freezing point of 221 ℃. In spite of its relatively high melting point, the low cost makes it widely used in solar energy collection field. Another commonly used salt mixture is called HTEC, which is a ternary system of $NaNO_3$, KNO_3 and $NaNO_2$ and has a freezing point of 141 ℃. This combination brings the melting point down but the lack of combination of optimum thermal properties limits its further application.

2.2.2 Thermal Conductivity Enhancement of PCMs

Although the usage of PCM is attracting because of its high energy storage density, most PCMs have low thermal conductivity, and that will restrain the heat transfer rate during charging

and discharging process. Many researchers have investigated the effects of adding conductive nanoparticles on the thermal conductivity of PCMs.

Table 2.3: Melting point of various nitrate salt systems [8]

Compound	Melting Point (℃)	Compound	Melting Point (℃)
$LiNO_3$	253	$NaNO_3$-$NaNO_2$	141
$NaNO_3$	307	$NaNO_3$-KNO_3-$Ca(NO_3)_2$	133
KNO_3	334	$LiNO_3$-KNO_3-$NaNO_3$	120
$Ca(NO_3)_2$	561	KNO_3-$Ca(NO_3)_2$-$LiNO_3$	117
$Sr(NO_3)_2$	570	$LiNO_3$-KNO_3-$NHNO_3$	92
$Ba(NO_3)_2$	590	KNO_3-$NHNO_3$-$AgNO_3$	52
$NaNO_3$-$NaNO_2$	221		

Xiao et al. added different mass rates of expanded graphite (EG) to binary nitrate salts consisting of $NaNO_3$ and KNO_3 (6:4) by aqueous solution method adopting ultrasonic. Four techniques, X-ray diffraction (XRD), scan electron microscope (SEM), energy dispersive spectrometer (EDS), transmission electron microscope (TEM) were applied to characterize and investigate the morphology, chemical composition of the composite PCMs. Figure 2.4 presents the SEM images for binary salt and the composite PCMs. They concluded that the EG had enhanced thermal conductivity to 4.884 W/(m ·K) at 2 % EG inclusion. However, the latent heat has been reduced by almost 11.0 %. [9]

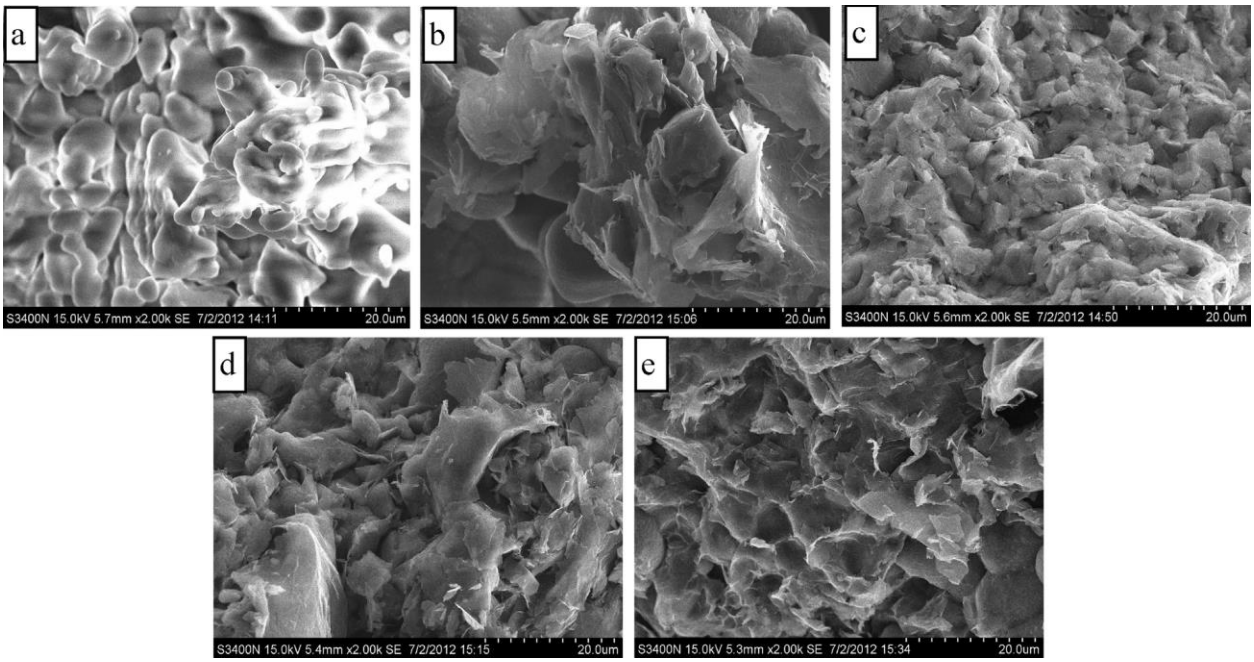

Figure 2.4: The SEM images of binary molten salt and composite PCM samples at room temperature. a) binary salt. b) to e): composite PCM [9]

Different from EG, Zhao et al. put a highly conductive additive expanded natural graphite treated with sulfuric acid (ENG-TSA) into the binary salt, $KNO_3/NaNO_3$ nitrate mixture. Samples with different densities and mass fractions of ENG-TSA addictive were prepared. Several thermal properties, thermal conductivity, phase transition properties, thermal stability and respective micro structures were evaluated. The results showed that the thermal conductivity has been improved and the highest effective thermal conductivity was 50.75 W/(m K), almost 110 times larger than the thermal conductivity of the salt powder. A slight decrease of latent heat was observed from the measurements. However, no obvious variation was observed in the phase change temperature. Figure 2.5 presents the thermal conductivity of different samples. Figure 2.6 shows the SEM images of the pure addictive and PCM composite. They found through the SEM investigation that the ENG-TSA has a uniform layer structure and thus it had a good thermal

performance in the direction of perpendicular to compression. In the PCM composite, the addictive establishes the effective heat transfer matrix, which helped the heat transfer more efficiently [10].

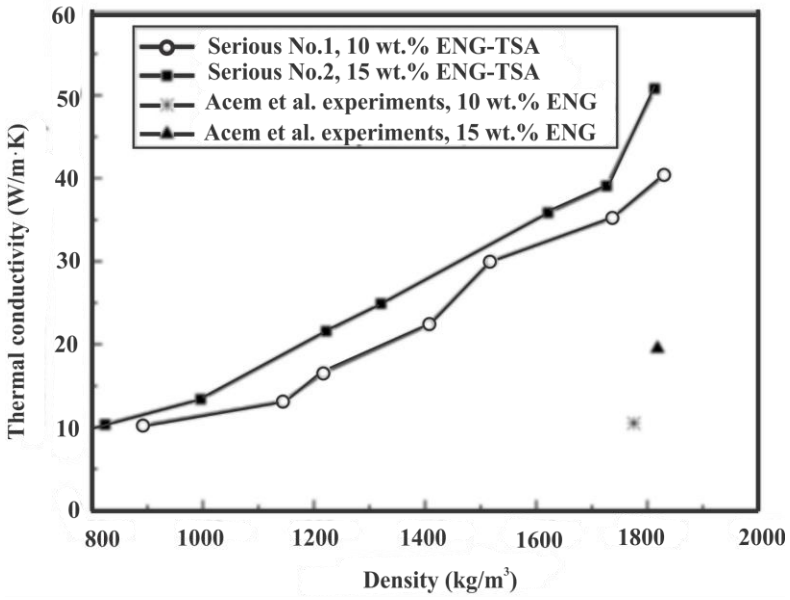

Figure 2.5: Thermal conductivity vs density of composite samples [10]

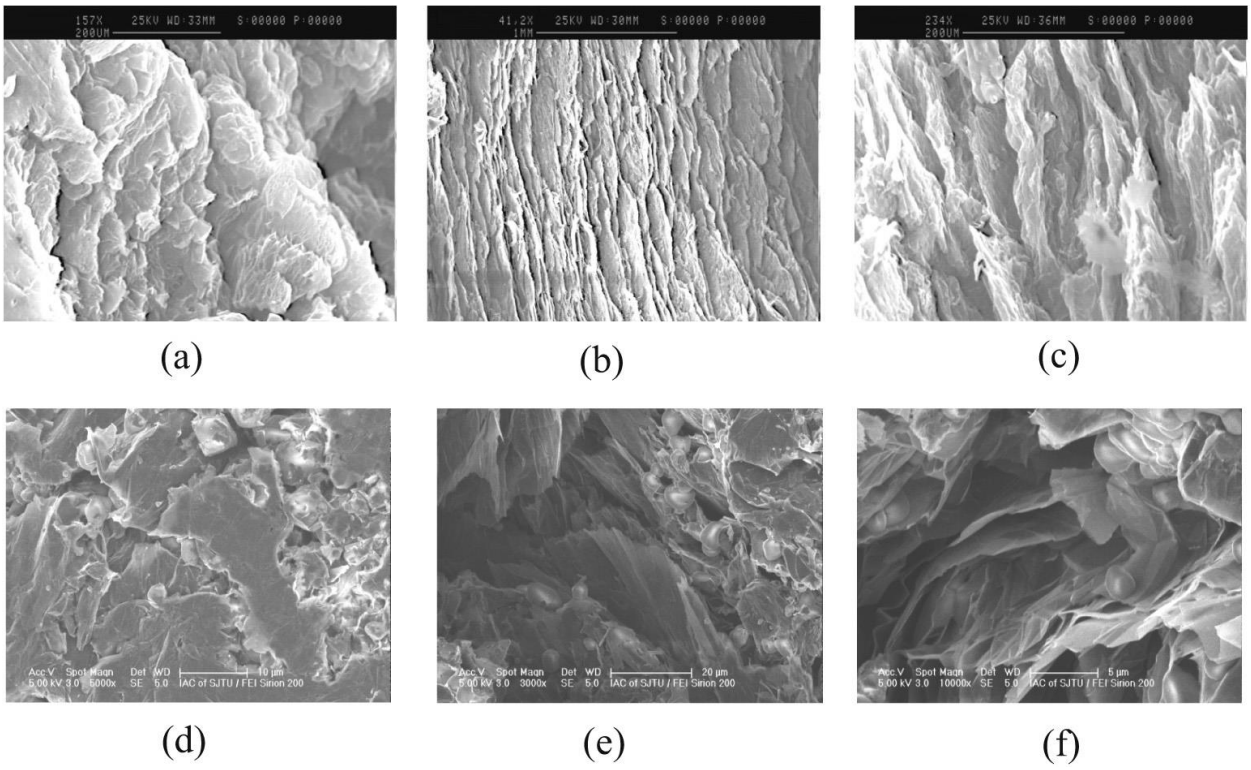

Figure 2.6: SEM pictures for consolidated samples of pure ENG-TSA a) to c) and nitrates/ENG-TSA d) to f) [10]

Another way to enhance thermal conductivity is to add chloride as addictive. Peng et al. prepared the nitrate salt composite by statical mixing method. The composite consisted of KNO_3, $NaNO_3$, $NaNO_2$ and addictive A of the chlorides. The experiments found that with 5 % addictive, the composite had a better conductivity, thermal stability and its operating temperature increased from 500 ℃ to 550 ℃, in comparison of the ternary salt without addictive, as shown in Figure 2.7. The lower freezing point was obtained and the loss of nitrite content was observed [11].

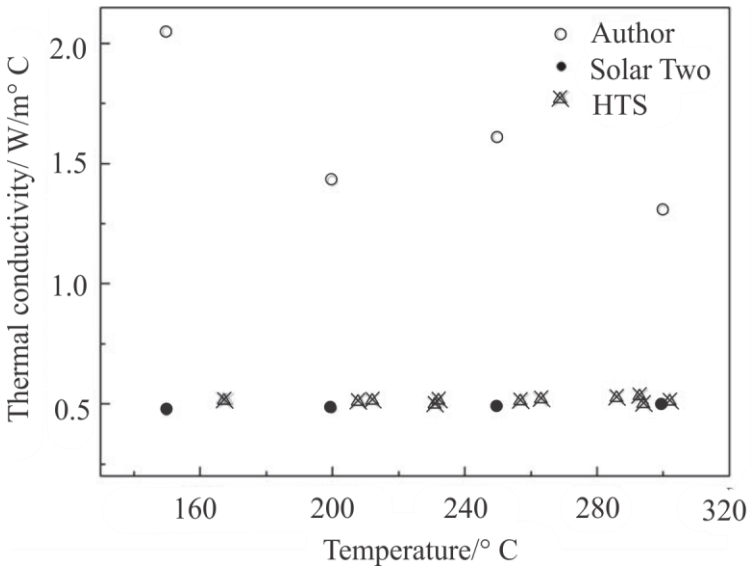

Figure 2.7: Thermal conductivity of molten salts [11]

Based on previous review, PCM composites with graphite can generate heat conductivity up to 100 times higher than a pure PCM. Those composites can be used to create compact TES systems when space is limited.

2.2.3 T-history Method and Its Development

The properties of PCM will affect its performance in application field. Table 2.4 shows the basic characteristics considered when choosing appropriate PCMs.

The energy storage capacity of a PCM is defined by the enthalpy variation between two temperatures and it involves the both sensible and latent heat. Since it is desired to study the heat transfer process from PCM storage system to the heat transfer fluid, it is also indispensable to study the evolution of thermal properties with temperature. Thus the enthalpy vs temperature curves are required. Several researchers have been devoted to the development of appropriate evaluation methodologies [11–18].

Table 2.4: Main characteristics of energy storage materials [6]

Thermal Properties	Physical properties	Chemical properties	Economic properties
Phase change temperature fitted to application	Low density variation	Stability	Cheap and abundant
High change of enthalpy near temperature of use	High density	No phase separation	
High thermal conductivity in both liquid and solid phases (although not always)	Small or none undercooling	Compatibility with container materials. No toxic, no flammable, no pollutant.	

Analysis techniques used to study phase change are mainly conventional calorimetry, differential scanning calorimetry (DSC) and differential thermal analysis (DTA) [6]. Among the studies related to DSC, Flaherty characterized hydrocarbons and natural waxes [20]. Giavarini characterized the petroleum products [21]. DSC is the most used method for determining the storage capacity because it is one of the most common commercial devices.

Another emerging popular method to determine the thermal properties of PCMs is T-history method, proposed by Zhang and Jiang [22] and improved by Marin et al. [12].Until now, the T-history method has been implemented by several scientists to measure the enthalpy vs temperature curves of PCM during melting and freezing. This method can be applied to study some properties like sub-cooling, hysteresis and phase change temperature range [16], [18], [23].

Comparing to DSC technique, it is useful to obtain the heat of fusion and specific heat of various PCMs simultaneously. In addition, the physical properties of the samples obtained by T-history method will be similar of those bulk materials used in practical systems as it uses larger sample size in conducting the experiment.

The original T-history method applied a water bath to raise the PCM candidates and reference samples to the required temperature and thereafter to obtain the cooling curve [22]. Figure 2.8 presents the original setup of Zhang and Jiang.

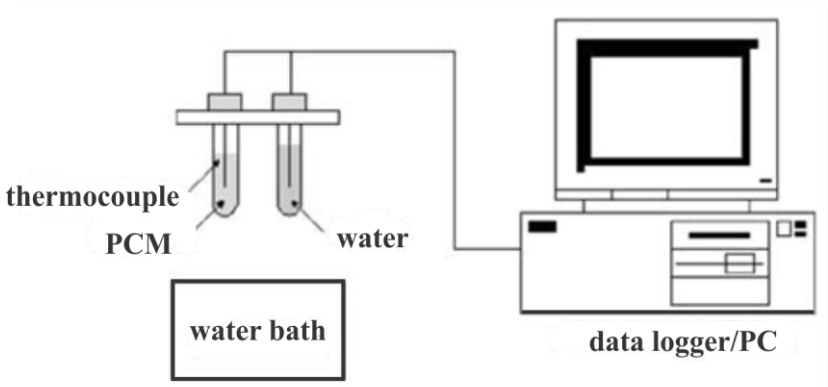

Figure 2.8: Original T-history method experiment setup by Zhang et al. [22]

The original T-history method uses water bath to raise the temperature of the PCM candidates and reference samples to the required melting temperature and thereafter to obtain the cooling curve. However, in this way this method can only be applied to PCM candidates that has a melting point lower than 100 ℃. For middle high and high temperature PCMs, water bath will not be a feasible option to melt the selected PCMs. In addition, distilled water was used as a reference sample in Yinping's experiments as the thermos-physical properties of water is well known [22]. As water will boil at 100 ℃ under normal pressure. So the reference material is also not suitable for high temperature application.

Facing these problems, researches have been carried out to improve the original T-history method. Rathgeber et al. designed a T-history experiment setup for temperatures between 40 °C and 200 °C [24], as shown in Figure 2.9, in order to get an accurate enthalpy-temperature curve. The author adopted a three step procedure, consisting of an indium calibration, a measurement of

the specific heat of copper and measurements of three PCMs. The author proved the success of the experiments by comparing the T-history enthalpy curves to literature data and DSC step measurements and good agreement has been found.

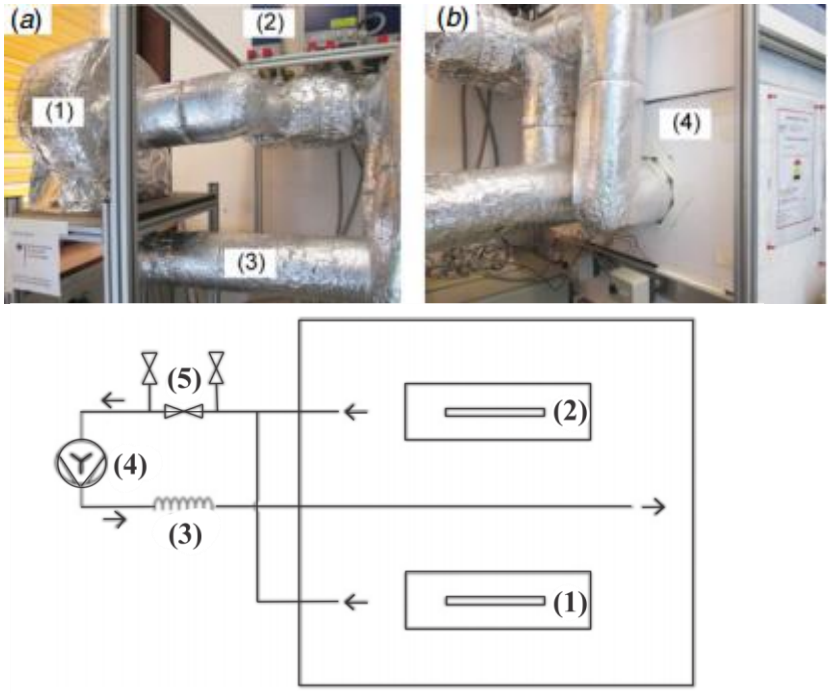

Figure 2.9: T-history installation controlled ambient with electric heater for high temperature application and its diagram [24]

Considering the less application of T-history method for phase change slurry (PCS) available in literature, Buttitta et al. applied T-history method to investigate the thermal properties of phase change slurries in solar power generation. The PCS author tested in the paper is based on micro-encapsulated n-eicosane suspended in water. The experiment results were compared with theoretical data. Also, the creaming phenomenon was discussed. In this experiment, the thermostatic bath was applied as the temperature steady environment, although

the temperature is not higher than 100 ℃. Figure 2.10 presents the enthalpy versus temperature curves [25].

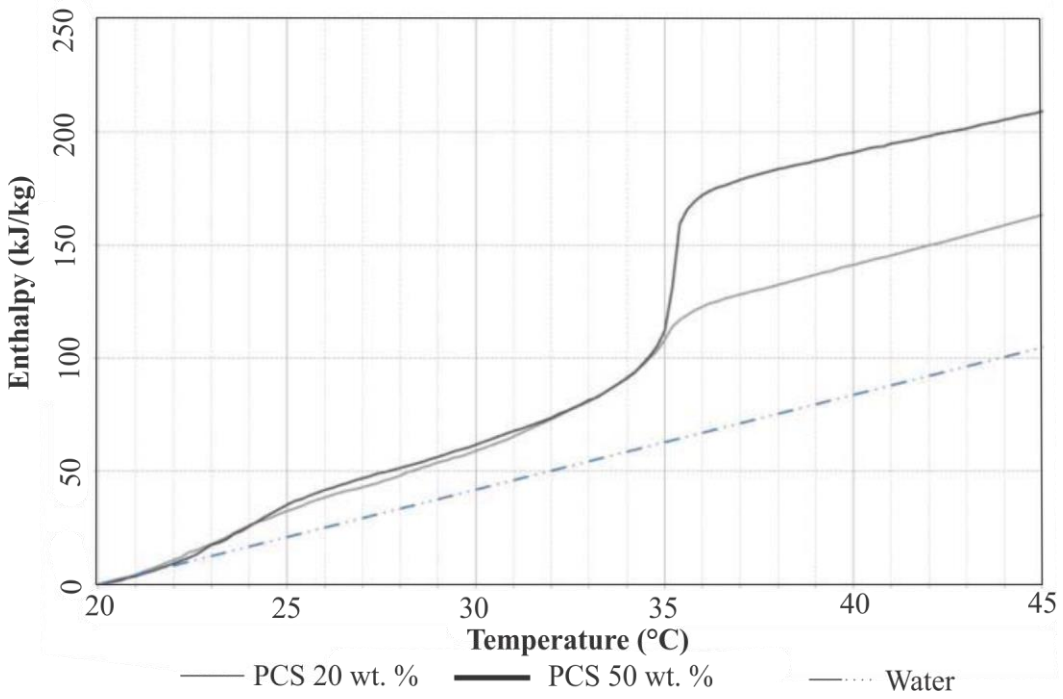

Figure 2.10: Enthalpy vs temperature curves [25]

Back in 2003, Marin et al. has made an improvement to the original T-history method. The authors further developed the evaluation procedure for determining c_p, and h as the dependent value of temperature. Most important of all, the author proposed to present the measurement results in the way of enthalpy-temperature curves. It has a great impact on the T-history method development in the later days [12]. Figures 2.11 and 2.12 are the authors' results.

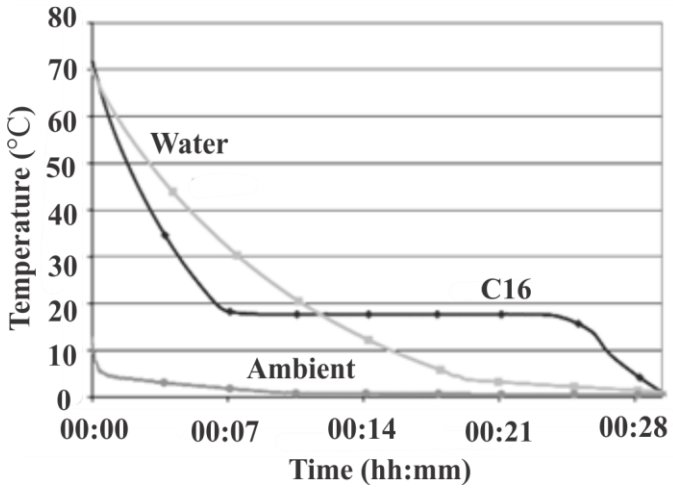

Figure 2.11: Experimental temperature-time curve obtained for paraffin C_{16} [12]

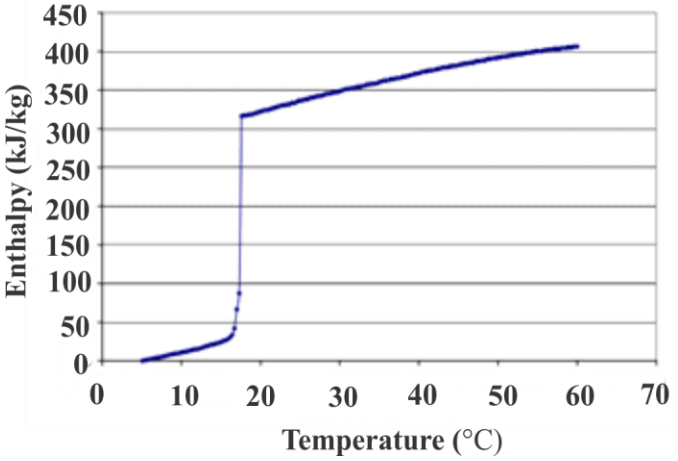

Figure 2.12: Enthalpy-temperature curve [12]

2.3 Numerical Simulation Study Related to Latent Heat Storage

Nowadays it is of great interest for researchers to use simulation tool to investigate the melting and freezing behavior of PCMs in the TES unit or to evaluate the TES unit's performance. The great advantage of simulation is fast and low cost in comparison with experimental investigation.

Common two methods to describe phase change problems are enthalpy method and modified heat capacity method. Both of them are used with fixed domain methods. Some review about mathematic models and numerical methods to phase change problems can be seen in Ref. [26]. Conduction and convection heat transfer both exist in melting and solidification. Numerical simulations of phase change problems can be divided into two categories: conduction dominated and conduction/convection controlled. However, convection heat transfer in liquid PCM needs to be considered in order to make the simulation closer to the reality.

2.3.1 Enthalpy Method

The enthalpy method can be applied to three dimensional phase change problems. Shamsundar and Sparrow proposed this method to solve solidification problem in a convectively cooled container. In the authors' simulation, implicit finite difference and Gauss-Seidel iterative method was selected [27]. According to Liu et al. [26], compared to the effective heat capacity method, the main disadvantage of enthalpy method is the difficulty of handling super cooling and temperature oscillation problems, while the effective heat capacity is hard to deal with PCMs with narrow phase change temperature range.

One of the research hotspot in latent heat storage area is to investigate the effect of high thermal conductive nanoparticles in the PCMs on the thermal conductivity. For this purpose, some researchers have carried out numerical simulation to see how the performance was improved of heat collection after adding nanoparticles.

Recently, Das et al numerically investigated the melting behavior of PCM composites in a single shell and tube TES unit [28]. The PCMs they investigated are organic alkane n-eicosane and n-eicosane/graphene nanosheets with different fractions. They chose water as the heat

transfer fluid. With the two dimensional axi-symmetric CFD model based on enthalpy-porosity method, the metling behavior was studied. The numerical simulation showed that higher inlet temperature decreases the melting time due to accelerated natural convection. Also, they found that the inclusion of graphene nanosheets significantly decreases the melting time. The melting time reduced significantly around 41 % at 2 vol% graphene loading, as shown in Figure 2.13.

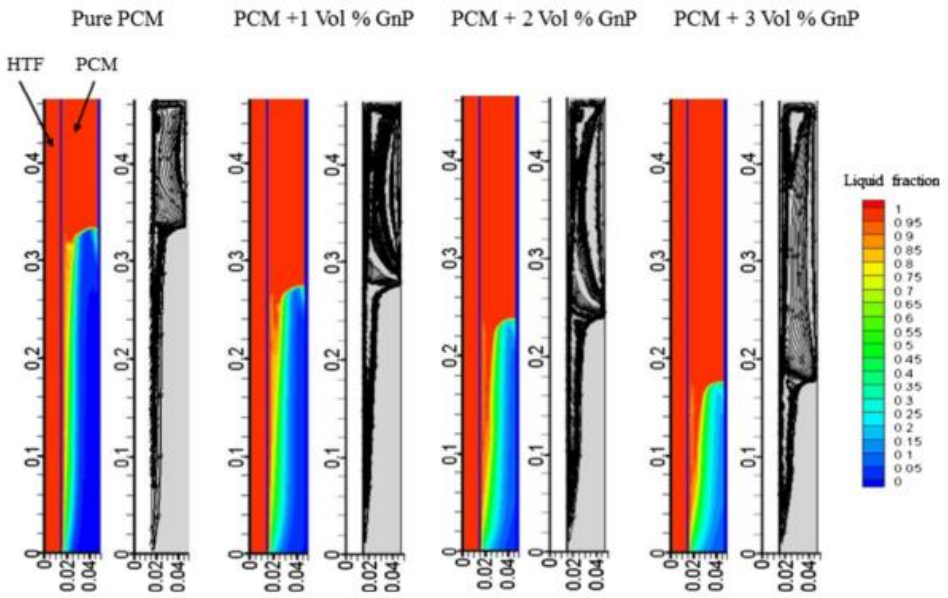

Figure 2.13: Effect of Gnp loading on melting at 4800 s with HTF = 60 ℃ [28]

2.3.2 Apparent Heat Capacity Method

In heat capacity method, the main variable, different from enthalpy method, is temperature. The strategy is to recover some kind of modified heat transfer equation. To take into the effect of latent heat, a high specific heat is added in a narrow interval of temperature. Bonacina proposed the following equivalent physical constants as shown below [29]:

$$C_{eq} = \frac{L}{2\nu} + \frac{C_s + C_l}{2} \quad \text{for} \quad |T - T_m| \le \nu \tag{2.1}$$

$$k_{eq} = k_S + \frac{k_L - k_S}{2}[T - (T_m - \nu)] \quad \text{for} \quad |T - T_m| \le \nu \tag{2.2}$$

It is found that the result is relatively independent of the regularization parameter ν when one phase problem is involved. In contrast, numerical results are strongly affected for general two phase Stefan problems. Comini et al. adapted this technique to finite element method (FEM), obtaining an equivalent heat capacity as the derivative of enthalpy with respect to temperature [30].

As to thermal energy storage systems, different structural geometries have been studied. The cylinder-tube geometry is the more widely used. He and Zhang solved numerically a mathematical model describing the unsteady freezing problem coupled with forced convection. The method of finite difference was used to solve the equations. Center-difference was used to solve the equations. Center–difference and fully implicit scheme was successful in this work. Three stages treatment leaded to solution of phase change process equations. Their results were compared with experimental values. Figure 2.14 shows the schematic of the heat exchanger [31].

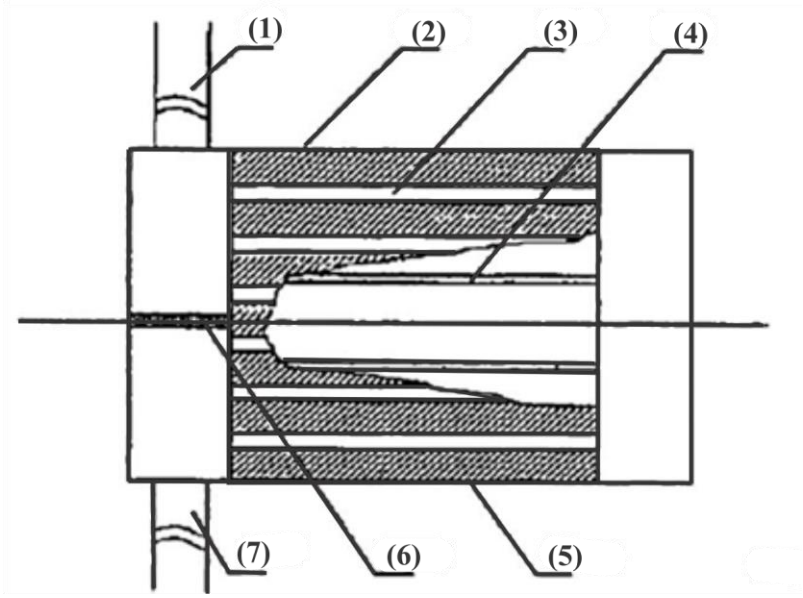

Figure 2.14: Schematic of the heat exchanger investigated.(1)Tube for gas entrance;(2)PCM;(3)Tube for heat transfer;(4)Electric heater;(5)Shell;(6)Baffle-board;(7)Tube for gas exit [31]

Buschle et al. employed the “Modelica” software. For the simulation, the storage tube was discretized into control volumes in the axial direction, as shown in Figure 2.15 [32]. The PCMs around the storage tube elements were further discretized in the radial direction. Three ways to calculate the enthalpy in the “Modelica.Media” models were compared. The first method was the linear interpolation using “If-, Else if-and Else-clauses”; the second method was the usage of the arc tangent function; and the third method was the usage of the error function.

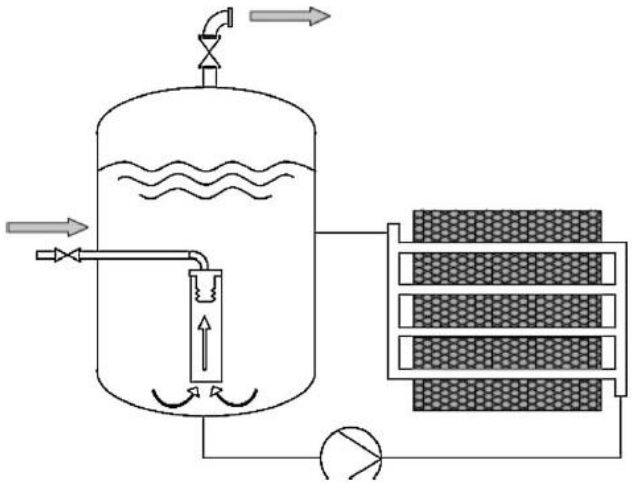

Figure 2.15: PCM enhanced steam accumulator [32].

Gong and Mujumdar developed a finite element model to simulate the cyclic thermal process involved as a results of alternating meting and freezing processes. The physical model consists of a tube which is surrounded by an external coaxial cylinder made up of several segments of different PCMs with different melting points, as shown in Figure 2.16. Semi-discrete equations using standard Galerkin finite element method was used. In their numerical results they indicate that the heat transfer rate can be greatly enhanced using multiple PCMs as compared with a single PCM. They also applied this model to space-based activities [33].

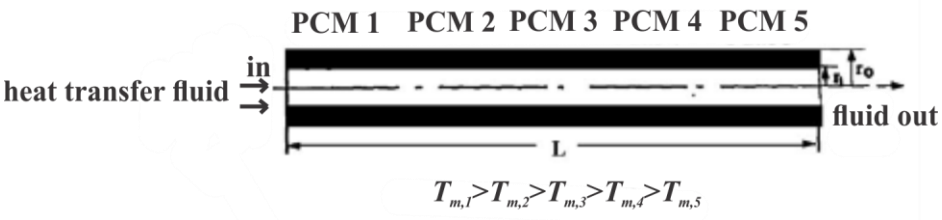

Figure 2.16: Physical model of the tube segmented PCM cylinders structure [33]

Cui et al. analyzed the energy transfer of the heat receiver cavity, as shown in Figure 2.17. They developed a heat balance model of the solar heat receiver, a cavity radiation mathematical model and a working fluid tube heat transfer model. The enthalpy formulation of the heat transfer equation was used for the tubes. The system was studied as a three-dimensional cylindrical coordinate using the finite volume method was a simple explicit scheme. They conclude that the design of the working fluid tube needs to be further improved in order to increase the liquid PCM fraction and reduce both the gas outlet temperature variation and the system mass [34].

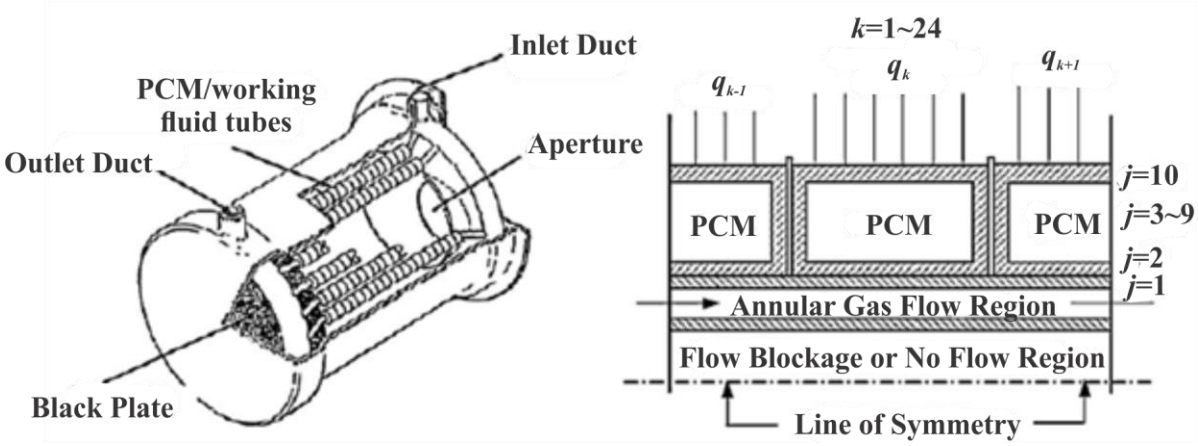

Figure 2.17: Solar heat receivers. Right: Schematic of encapsulated PCM tube configuration with annular gas flow [34]

Based on enthalpy method, Cui et al. developed a numerical model of the unit heat exchanger tube, as shown in Figure 2.18. The model considered PCM solid or liquid heat resistance and the influence of the void. The enthalpy method energy equation was used with some assumptions: phase change takes place at a distinct temperature. Conservation of the energy was expressed in three-dimensional cylindrical coordinate. The comparison with experimental results showed higher values of the simulated results [35].

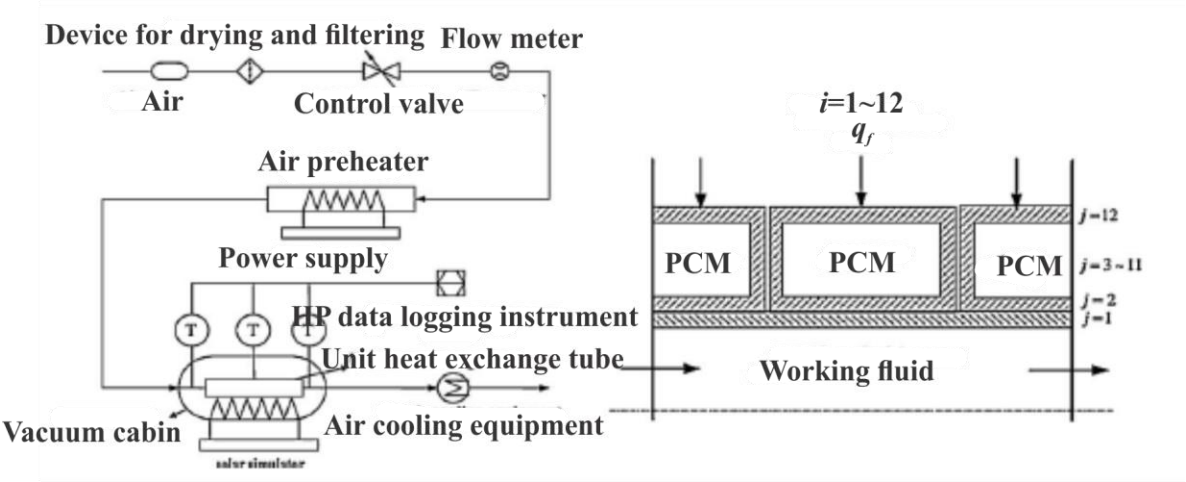

Figure 2.18: Left: Scheme of experiment system. Right: Schematic of PCM tube configuration [35]

Guo and Zhang used the phase change package of "ANSYS Fluent'' (enthalpy-porosity technique) to perform the numerical simulations. Transient two dimensional heat conduction problems were solved using the Fluent 6.2 software when heat was extracted from the PCMs during the discharging process. They pointed out that adding aluminum foils was an efficient way to enhance the heat transfer, as shown in Figure 2.19 [36].

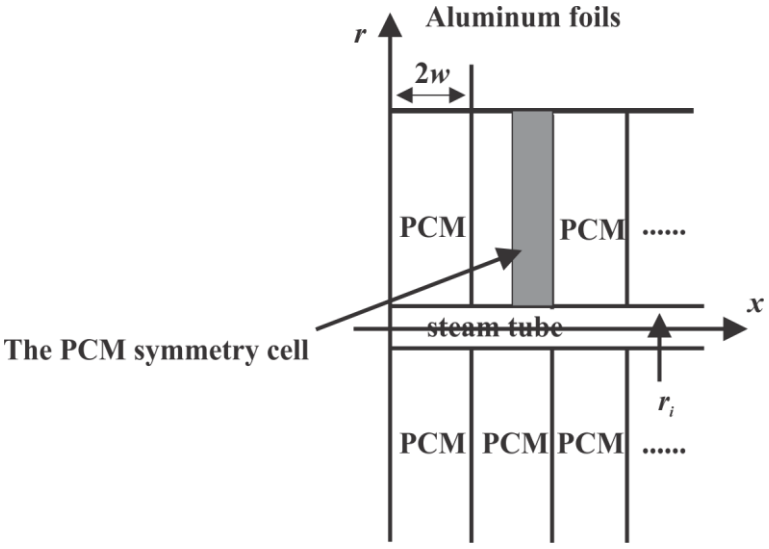

Figure 2.19: Layout of the problem studied by Chaxiu and Wujun [36]

Yimer and Adami developed a two dimensional transient analytical model based on the enthalpy method, as shown in Figure 2.20. They presented a dimensionless analysis. Two dimensional finite difference representations were used: radial and angular variations, and radial and axial variations. The Gauss–Seidel iterative method with successive over-relaxation (SOR) was used to solve the nonlinear simultaneous difference equations. Some parametric studies were shown also [37].

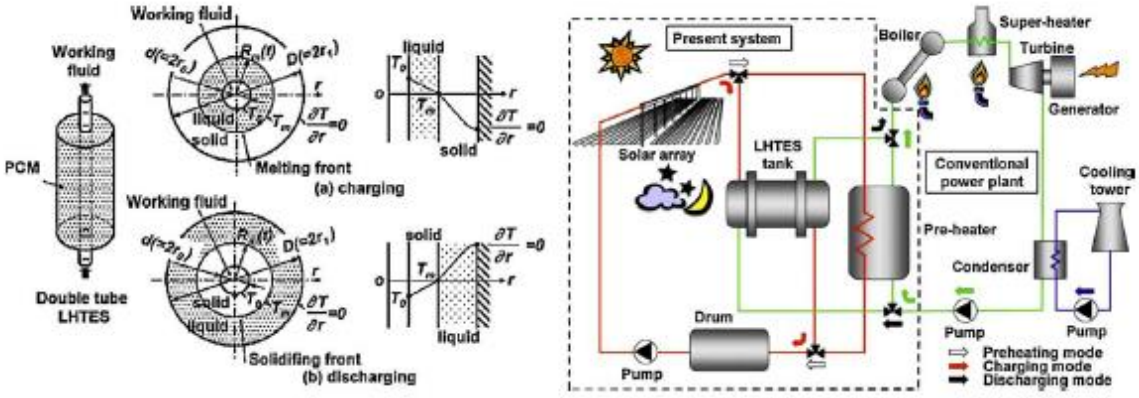

Figure 2.20: Left: Scheme of PCM tube configuration. Right: Layout of the plant [37]

2.4 Experimental Work Related to Latent Heat TES System

PCMs as the storage media for thermal energy, are always put into different kinds of containers for energy storage. Among all of the encapsulation containers, slab geometry and cylindrical geometry are commonly used. Many researchers have done both numerical and experimental work to heat transfer process of PCMs in different containers. Generally, PCMs have low thermal conductivity and expand on melting therefore, the design of a suitable heat exchanger is an important component of a latent heat storage system. Various kinds of heat exchangers were tried by a number of researchers and are a given as following.

Kabbara and Abdallah experimentally investigated the performance of a thermal storage unit with phase change materials encapsulated in cylinders, as shown in Figure 2.21 [38]. Air was the heat transfer fluid that flowed across the tube banks to charge and discharge the storage system. The storage capacity and heat transfer rate to PCM of this system was analyzed. The aim of this experiment was to offer a solid ground for scaling up and implementation on solar residential domestic heating applications.

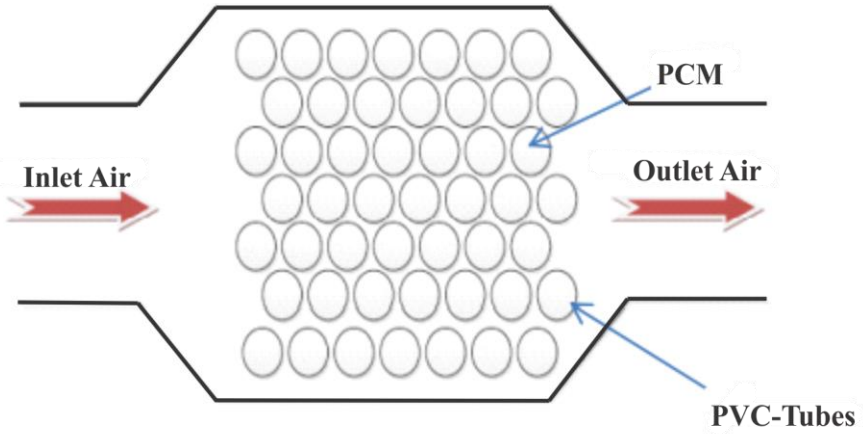

Figure 2.21: General Layout of the thermal storage unit [38]

Some researchers are dedicated into the transient heat transfer for PCM during phase change. Zhang et al. used temperature-change hot chamber method (TCHCM), an experimental procedure to validate transient heat transfer mathematical models that involve phase transitions. The models validated are enthalpy and the effective heat capacity methods. The mathematical models fit well with the experimental data. The author proves that TCHCM is a simple, effective, and can fully validated heat transfer mathematical models involving phase transitions. The experimental device was shown in Figure 2.22 [39].

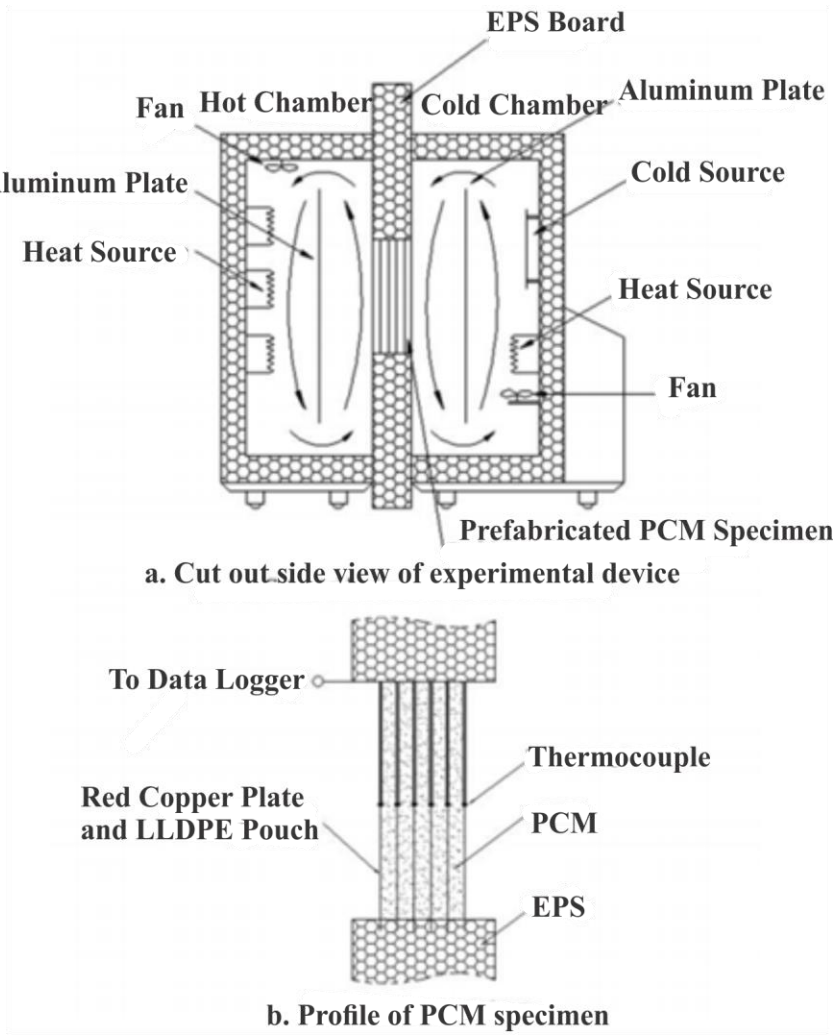

Figure 2.22: Experimental device [39]

Some researchers have done small scale TES energy storage test. Thapa et al. fabricated a small scale TES device that collects and stores heat in a PCM. The author used icosane wax as PCM. A physical device is constructed on the millimeter scale to examine specific effects of low-cost thermal conductivity enhancements that include copper foams and other metallic inserts, as shown in Figure 2.23. Numerical methods are used to compare with experiments data and the results fit well. Results show that the system capable of extending thermoelectric operation

several minutes through the use of thermal energy storage techniques within the effective conductivity ranges [40].

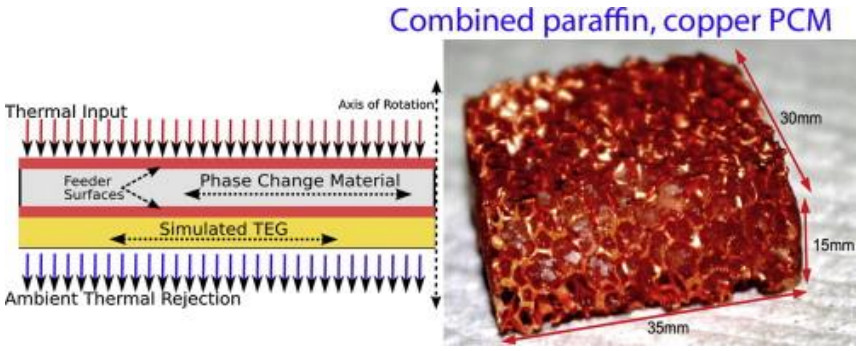

Figure 2.23: The schematic of the TES device and the duocel copper foam for conductivity enhancement [40]

At the aspect of energy building, Kuznik et al. experimentally evaluate the capacity of PCM to stabilize the internal environment when there are external temperature changes and solar radiations. The schematic of the test chamber and thermal probe positions are shown in Figure 2.24. The results showed that the PCM covered walls effectively stabilized the internal environment [41].

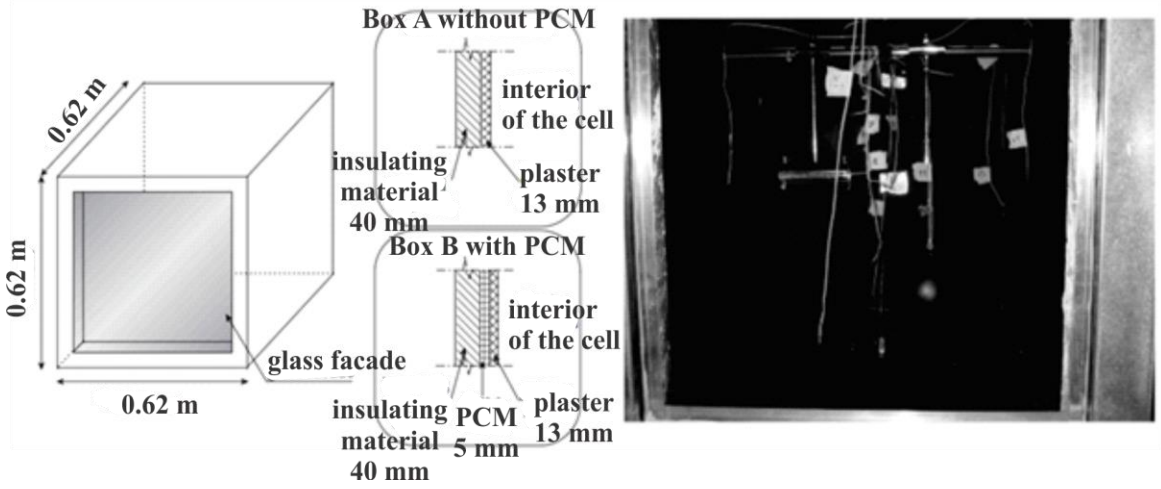

Figure 2.24: Left: Experiment test cells. Right: Measurement probes inside MIROBAT [41]

Stefan number is commonly used in heat and mass transfer problems during solidification and melting and describes the relationship between sensible heat and latent heat.

$$Ste = C_{p,l}(T - T_m) / L \tag{2.3}$$

where *Ste* is the Stefan number, $C_{p,l}$ is the specific heat capacity of liquid PCM, T_m is the melting point of PCM, and L is the latent heat of PCM. From the equation, as the sensible heat increases, the Stefan number increases and when latent heat increases, Stefan number decreases and vice versa.

2.5 Applications of TES Systems in Power Plant

PCMs have been used for various thermal storage applications since 1980s, and they have recently been used as a storage media for heat storage in power generation, especially in solar power plant. In 2009, Gil et al. summarized the state of art on different storage concepts and all materials considered in literature or plants [5]. The models of such systems are also reviewed. According to the authors, high temperature storage concept in solar power plants can be classified as active or passive systems, as shown in Figure 2.25.

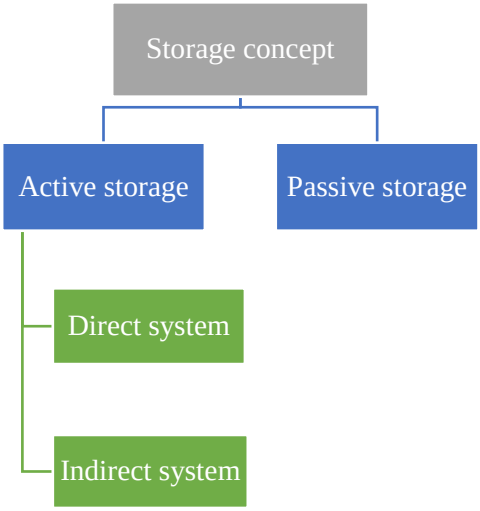

Figure 2.25: Scheme of classification of different storage systems according the storage concept [5]

2.5.1 Active Storage Systems

From the study of Gil et al., in an active direct system, most solar systems use heat transfer fluid both as a heat transfer medium and a storage medium [5]. The use of molten salts or steam as a heat transfer fluid or storage materials at the same time eliminates the need for an expansive heat exchanger. It allows the solar power plant to be operated in a higher temperature than common heat transfer fluid allow. The cost of thermal energy storage system can be reduced and the performance is improved. From the study of Kearney et al. [42], molten salt as a heat transfer fluid can make economic sense only if the solar plant included a thermal storage system.

One of the active direct systems is the two tanks direct system, which consists in a storage system where the heat transfer fluid is directly stored in a hot tank, in order to use it during cloudy periods or nights. The cooled heat transfer fluid is pumped into cold tank [7]. Figure 2.26 shows the scheme of the solar power plant, molten salt ($NaNO_3$ and KNO_3) as heat transfer fluid. Solar Tres is placed on Fuentes de Andalucia, near to Seville (Spain) and was built during 2008.

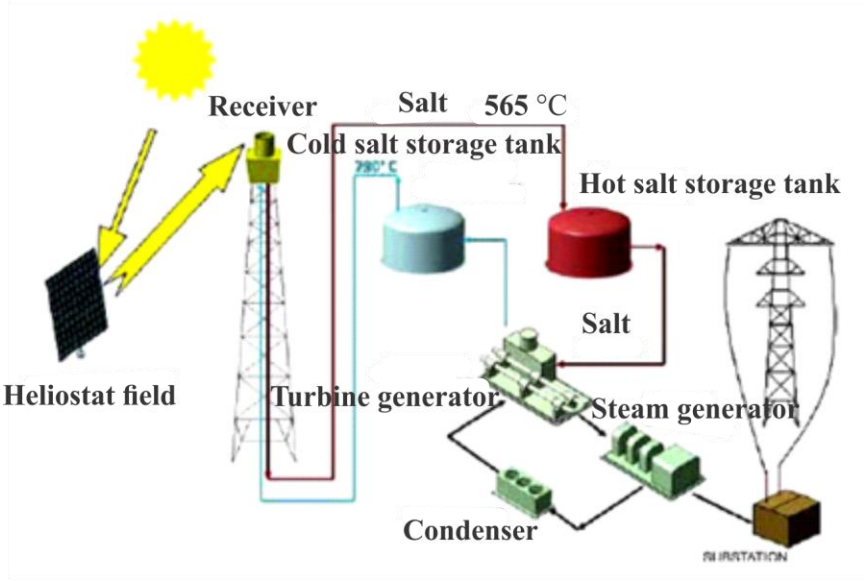

Figure 2.26: Scheme of installation of a central tower power plant (Planta Solar Tres), with direct two-tanks and mineral oil like storage systems [5]

The active indirect storage systems have single tank system (also called thermocline system) besides two tanks systems. The two tanks system is different from active direct systems because the heat transfer fluid circulating in the solar filed is different from the one for the storage medium (thermal energy storage medium). In two tanks indirect system, the two tank contains energy storage medium heat transfer fluid, while a second heat fluid (generally oil), heated the heat transfer fluid through the oil to salt heat exchanger. In Figure 2.27, heat from the heat transfer fluid is absorbed in the oil-to-salt heat exchanger by thermal energy storage media, normally molten salts. During a thermal energy storage charge cycle, a portion of the oil from the collector field is directed to the oil to salt heat exchanger, while the oil cools from the nominal inlet temperature of 391 ℃ to an outlet temperature of about 298 ℃. Nitrate salt from the cold storage tank flows in a counter current arrangement through the exchanger. The heat transfer salt is heated from an inlet temperature of 291 ℃ to an outlet temperature of 384 ℃, and then stored

in the hot storage tank. During the discharge cycle, the oil and salt flow paths are reversed in the oil to salt heat exchanger. Heat flows from salt to the oil, which provided thermal energy to the steam generator.

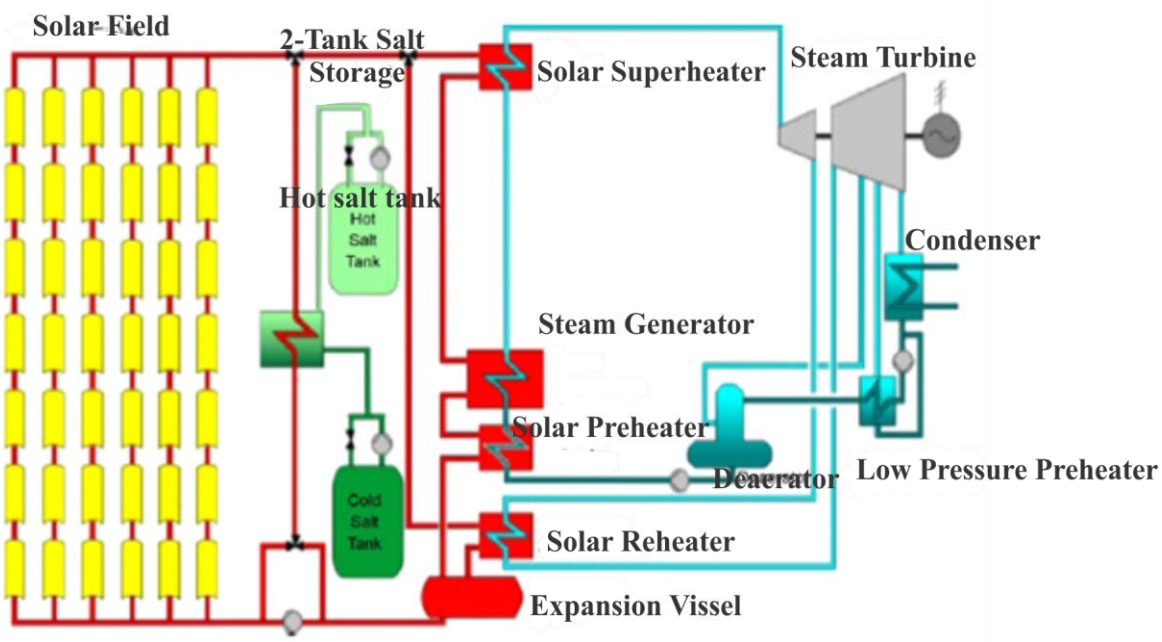

Figure 2.27: Scheme of installation of a parabolic through power plant, with two tanks storage systems [7]

Another popular indirect storage system is the single tank system, where hot and cold fluid store in the same tank. The single tank system is cheaper than two tank system. In the single tank, hot and cold fluids are separated because of the stratification, and the zone between the hot and cold fluids is called the thermocline.

The thermocline storage system features the hot fluid on top and the cold fluid in the bottom. In these systems, the heat transfer fluid which arrives from the solar field passes through a heat exchanger, heating the thermal storage fluid media. This fluid is stored in a single tank. Usually a filler material is used to help the thermocline effect. Experimental studies performed up to now found that this filler material acts as the primary thermal storage medium, but selection of other

storage and filler materials can change this. In 2005, Sandia National Laboratories identified quartzite rock and silica sands as potential filler materials [43]. Results demonstrated that both materials appear able to withstand the molten salt environment quite well (No significant deterioration). Thermocline system has an advantage that most of the storage fluid can be replaced with a low cost filler material, for example, quartzite rock and sand, as shown in Figure 2.28.

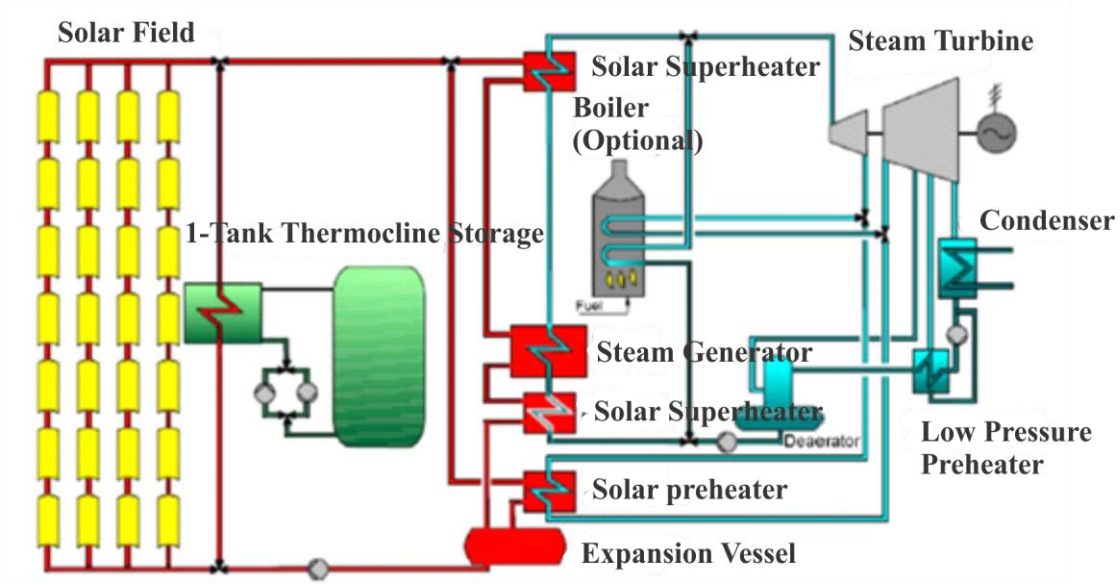

Figure 2.28: Installation scheme of a parabolic through power plant, with single tank storage system [7]

2.5.2 Passive Storage Systems

In a passive storage system, the heat transfer medium passes through the storage only for charging and discharging. The storage medium itself does not circulate. Passive systems are generally dual medium storage systems (these systems are also called regenerators). Solid storage materials like concrete and castable materials and PCMs are mainly used for passive storage systems. Figure 2.29 shows one case that use concrete storage. In this passive system, the

solar energy is transferred from the heat transfer fluid to solid storage material system. The storage material contains a tube heat exchanger to transfer the thermal energy from the heat transfer fluid to the storage. This heat exchanger demands a significant share of the investment costs. The design of its geometry parameters like tube diameter, number of pipes and tube arrangement is important for the final result.

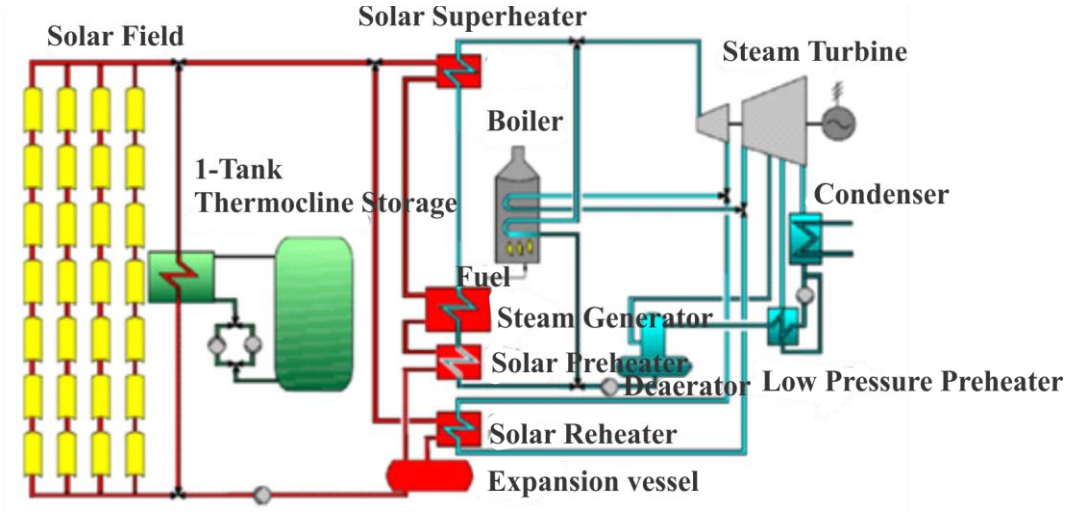

Figure 2.29: Scheme of a parabolic through power plant, with concrete (or castable ceramics) storage system [5]

Apart from sensible materials, phase change materials are another kind of storage material. The melting temperature of PCM is within the temperature range of charging and discharging temperature of heat transfer fluid.

2.6 Summary

This chapter introduces the different aspects of studies related to the TES with PCMs. Start from the introduction to the classification of PCMs, the TES systems with PCMs are briefly

reviewed, and the phase change current modelling methods are discussed. Parts of the experiments related to thermal energy storage are presented.

Chapter 3: Thermal Analysis of Phase Change Materials

3.1 Introduction

As PCMs are the main components of latent heat TES system, their thermal properties such as the latent heat, the heat capacity, and the melting point will greatly affect the system heat storage performance. These three thermal properties are also the main consideration when designing the storage system's size and geometry. In order to know the specific values of these properties, the Differential Scanning Calorimetry (DSC) method and the T-history method are commonly adopted. This chapter investigates the results difference from the two methods and proposes materials for project application.

3.2 Differential Scanning Calorimetry Test

The DSC method is a mature thermal analysis technology, in which the difference in the amount of heat required to increase the temperature of a sample and a reference is measured as the function of temperature. Both the sample and reference materials are maintained at nearby the same temperature during the DSC test. Generally, the temperature program for a DSC analysis is designed such that the sample holder temperature increase linearly as a function of time. With DSC, the thermal properties of melting point, the latent heat of fusion and the heat capacity of PCM can be obtained.

3.2.1 Experiment Setup and Procedures

The instrument for DSC test in this experiment is the TA Q200, which is located in the Material Lab 2, School of Mechanical and Aerospace Engineering, Nanyang Technological University. The materials are normally weighted 0 ~ 10 mg as the samples. An aluminum pan

from Perkin Elmer serves as the sample container to hold the sample materials. Another one empty pan is used as the reference, as shown in Figure 3.1. The sample pan and reference pans are heated and cooled inside Q 200 chamber under the different heating and cooling rates. The data was processed using an external program: TA Universal Analysis. Appropriate cycles were selected for analysis.

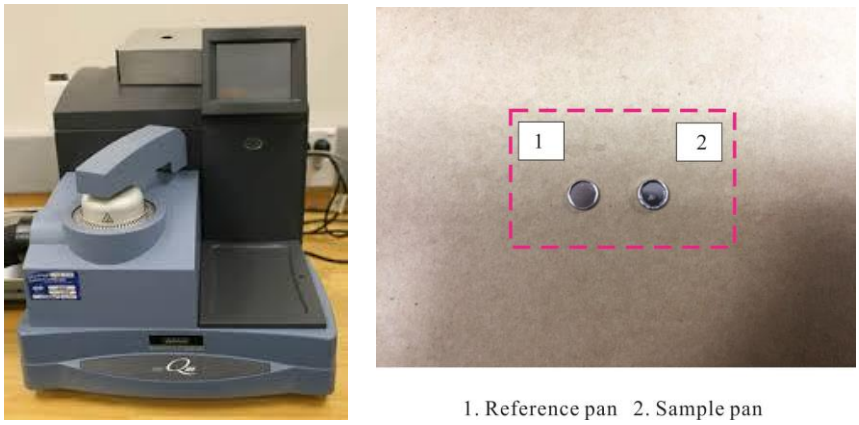

Figure 3.1: TA Q200 and aluminum pan used for DSC test

3.2.2 Results and Discussion

To conduct the DSC test, some commercial PCMs were applied in the tests. The results of the tests were applied on the choice of PCM for later experiments and the future project use. Both organic and inorganic materials were used in the tests.

3.2.2.1 Organic Phase Change Materials

1) Paraffin Wax

As a common commercial and cheap PCM, paraffin wax is applied widely in low temperature TES system [6]. In this study, paraffin wax, made by VWR, Singapore was tested.

6.9 mg paraffin wax was measured by high precision weight balance (accuracy: ± 0.0001 g) and then put in the sample aluminum pan. The heating rate set for the sample was as slow as 5 ℃/min to provide the accurate information. Figure 3.2 shows the melting part in the DSC curve of 6.9 mg paraffin wax under the heating rate of 5 ℃/min. It shows that paraffin wax has a glass transition from 29.09 ℃ to 33.92 ℃. The melting period comes from 45.01 ℃ to 61.73 ℃, and absorbs 128.20 J/g as its latent heat.

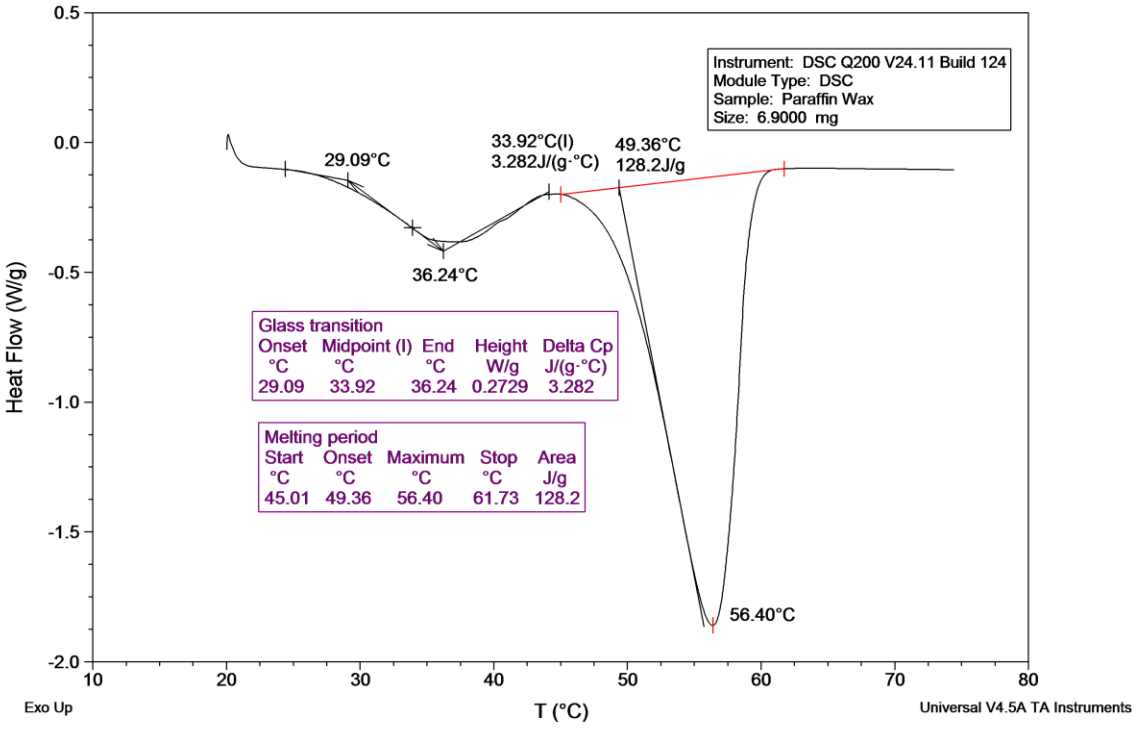

Figure 3.2: The DSC melting curve of 6.9 mg paraffin wax under the heating rate 5 ℃/min

2) D-Mannitol

Another organic material used for the test is D-Mannitol made by Sigma Aldrich. 7.5 mg D-Mannitol was used for test. To know the effect of the different heating rates, two different heat rates were applied in this test. The DSC melting curve under two different heating rates were

compared. The test result is shown in Figure 3.3. The heating rate was set at 10.00 ℃/min for two cycles, and in each cycle the material is heated up from 30 ℃ to 280 ℃, then cooled down from 280 ℃ to 30 ℃. As seen in Figure 3.4, comparing the two cycles of the melting processes, under the same heating rate, the melting point and the latent heat showed different values. In the second cycle, the latent heat decreased nearly 50 J/g. Comparing with the first cycle, the melting range of the second cycle reaches 37 ℃, increasing for 15 ℃.

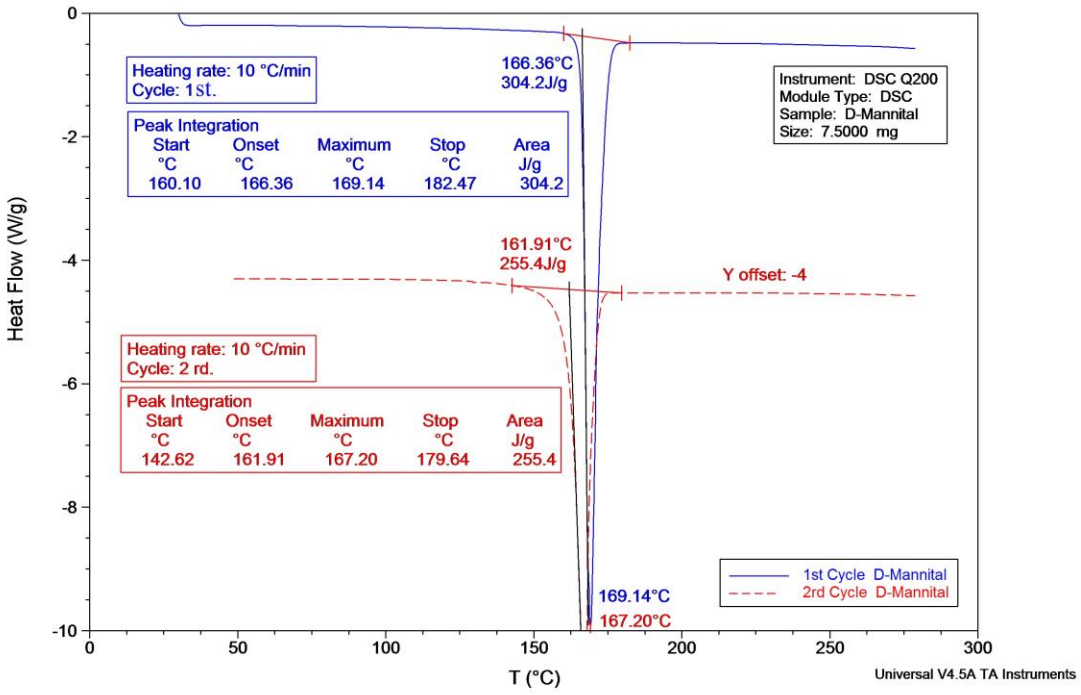

Figure 3.3: DSC curve for 7.5 mg D-Mannitol under two different heating rates

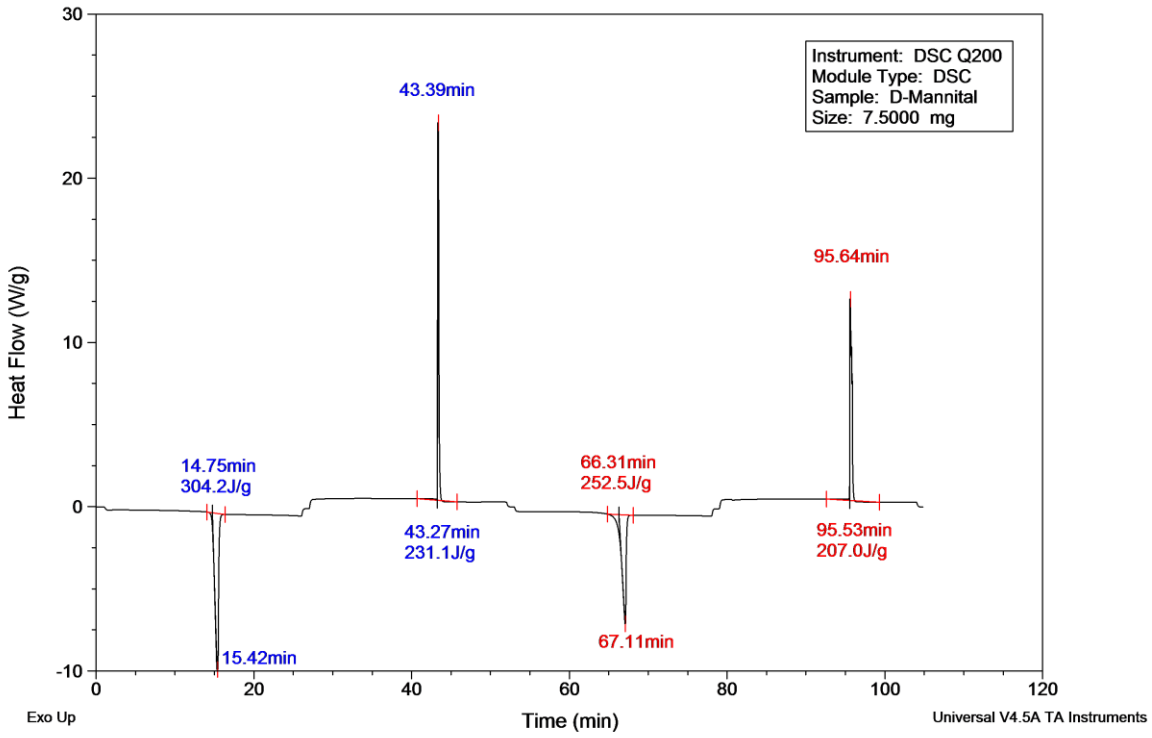

Figure 3.4: Heat flow versus time for 7.5 mg D-Mannitol

3.2.2.2 Inorganic phase change materials

1) Lithium Nitrate: $LiNO_3$

For the DSC test of $LiNO_3$, due to its high melting point and high latent of heat, the heating rate was set to 20 ℃/min. Figure 3.5 shows the result. From Figure 3.5, the melting range of $LiNO_3$ is from 232.21 ℃ to 275.13 ℃. While for freezing, the freezing range is from 250.25 ℃ to 220.70 ℃. The melting and freezing show different phase change behaviors, which means that in the choice of the PCM for the real application, it is considerate to consider the effect of difference between the melting range and the freezing range. Besides, the measurement results showed that the latent heat for melting is 304 J/g and the latent heat for freezing is 325 J/g. The

difference between them is 21 J/g. The reason for this difference may be because of the difference in the specific heat of the solid state and the liquid state respectively.

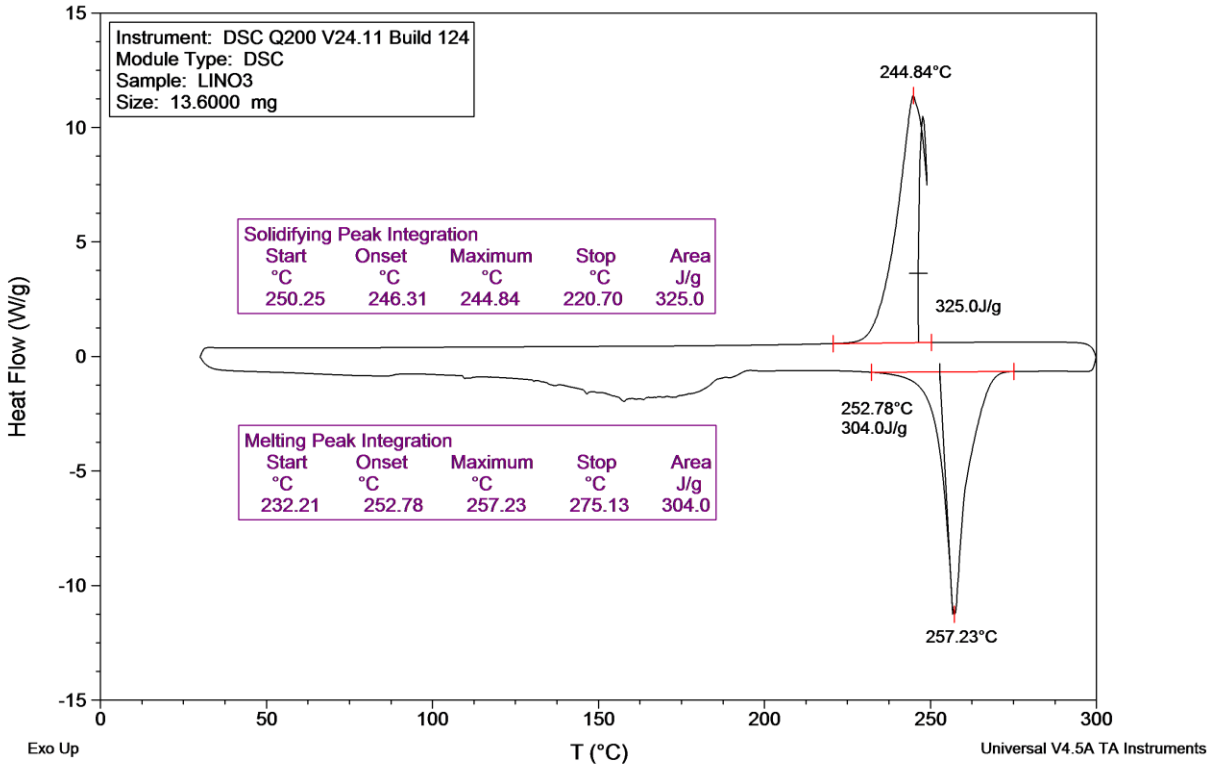

Figure 3.5: DSC curve for 13.6 mg $LiNO_3$ under heating rate 20 ℃/min

2) Potassium Nitrate: KNO_3

Potassium nitrate (KNO_3) is often used for the synthesis of gunpowder (Sulphur, char and KNO_3). It is also one of the important PCMs in the high temperature TES applications [5]. The measurement was carried out in DSC with a heating rate of 30 ℃/min for the temperature range of 30 ~ 300 ℃, 10 ℃/min for 300~400 ℃ severally. The test result was shown in Figure 3.6. Comparing with the test results by NETZSCH Company, as shown in Figure A-2, Appendix A, the second melting phase change peak has 3 ℃ difference and 6 ℃ difference for the first peak [44].

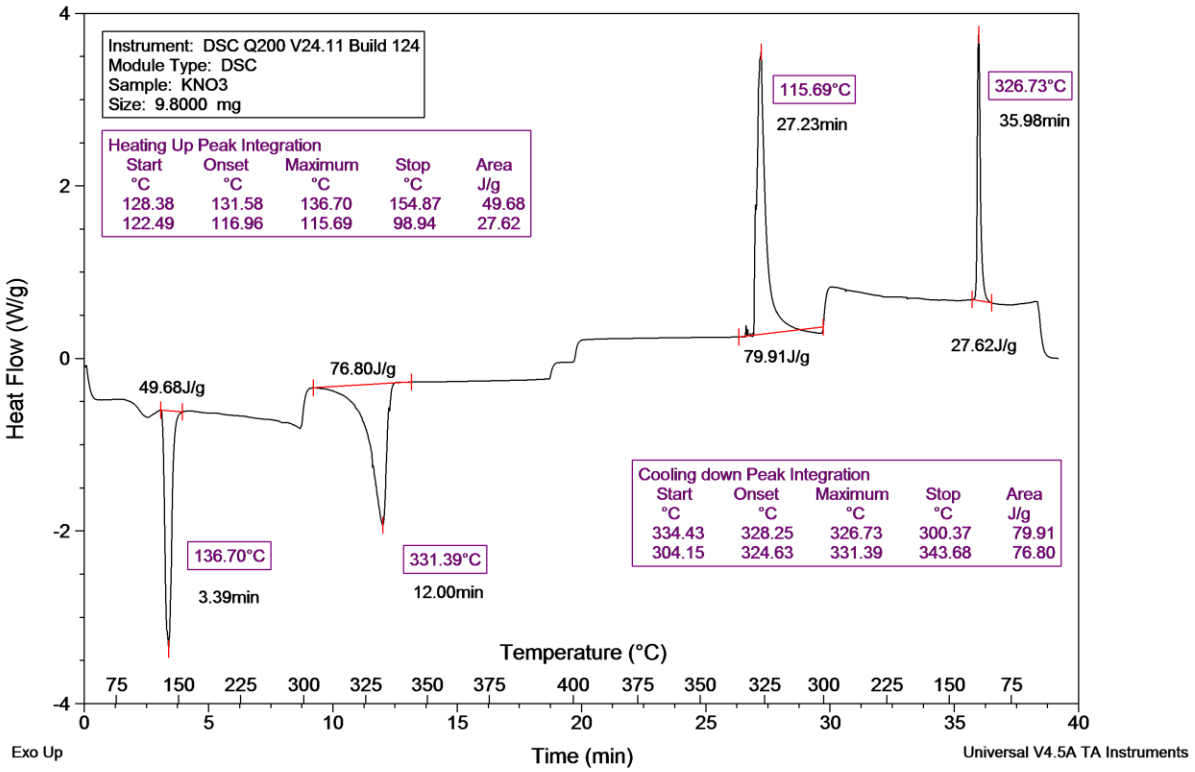

Figure 3.6: The DSC curves for 9.8 mg KNO_3 under heating rate 30 ℃/min for 30~300 ℃, 10 ℃/min for 300~400 ℃

3) Binary Salt mixture: KNO_3-$LiNO_3$ (60 %-40 % wt.)

Salt mixtures are commonly applied in the high temperature TES applications as PCMs. The two or more different salts can create a mixture that has a lower melting range [45]. This finding has a great importance because researchers can adjust the components based on the different TES application operating temperature ranges. As a trial, a salt mixture of $LiNO_3$ and KNO_3 was tested. The DSC result for KNO_3-$LiNO_3$ (60%-40% wt.) is shown in Figure 3.7. The weight ratio transferred from this molar ratio is 50.5 % to 49.5 %, thus making it easier to compare with literature. Zhang et al. plotted the phase diagram of KNO_3-$LiNO_3$, as shown in Appendix A-1, Appendix A [46]. According to the Zhang et al., the liquidus temperature for 50 %

mole fraction KNO_3 is 154.85 ℃, which is 428 K. The liquidus temperature for 5 ℃/min is 158.48 ℃. Their close value proves the DSC test accuracy at the low heating rate.

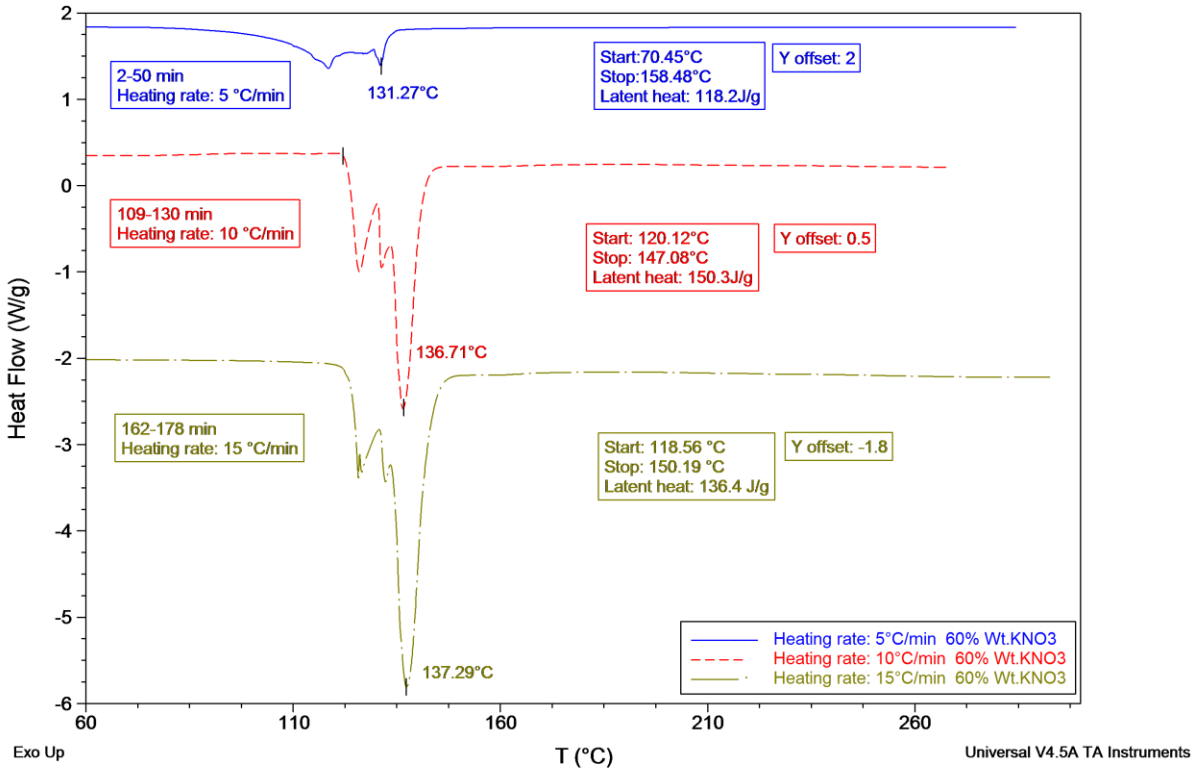

Figure 3.7: DSC melting curve for 13mg KNO_3-$LiNO_3$ (60%-40% wt.) mixture under three different heating rates

3.3 T-history Method Experiment

The T-history method was firstly developed by Zhang et al. [22]. This method enables researchers to obtain the melting point, the latent heat of fusion, the degree of sub-cooling, the thermal conductivity and the specific heat of several PCM samples simultaneously. The T-history method is similar to the DSC method from the function angle. However, compared to light DSC sample weight (normally at 0~20 mg range), T-history method has a relative heavier

weight sample, normally more than 10 g. In the real application, the PCM is commonly applied in a large amount, nor in a small amount. Thus the T-history method shows the behavior of the PCM close to reality. The main objective of the experiment is to identify the cooling curve with respect to time of different PCMs. Melting point, heat of fusion can be obtained through analyzing the cooling curve.

3.3.1 Experimental Setup and Procedures

The sample materials were grinded with a mortar and transferred to a test tube for melting. The test tube is inserted into an aluminum heating block on a heating plate, as shown in Figure 3.8. To observe the temperature increase of the PCM, a calibrated K type thermocouple was placed inside the PCMs. After the PCMs were observed fully melt, the retort stand was removed from the heating block and the PCMs were cooled back to the ambient temperature, as shown in Figure 3.9. The cooling curves of PCMs' temperature were recorded for further analysis.

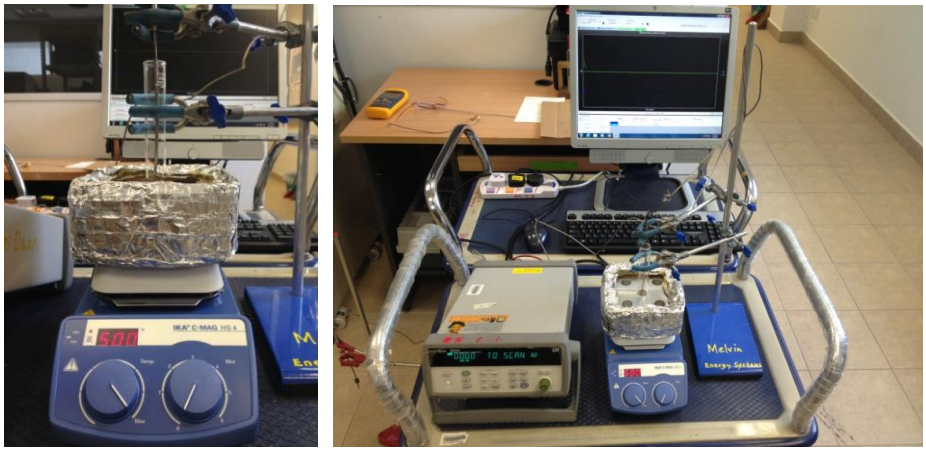

Figure 3.8: The modified T-history method set-up

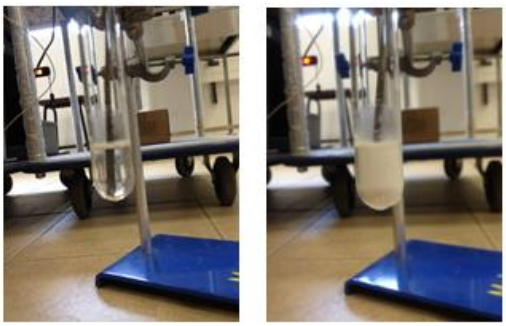

Figure 3.9: Cooling process of PCMs in the test tube

The thermocouples applied were calibrated before carrying out the experiments. The calibration will ensure that results obtained are accurate and reduces the error from the measurement. The test probes were inserted into a bath calibrator containing thermal oil. The temperature of the calibrator was manually controlled to increase from 30 ℃ to 90 ℃, with a step of 15 ℃ between each temperature level. A reverse cooling process was done afterwards, with same temperature interval. Three thermocouples were tested and the results were shown in Figure 3.10 as follows. As the respective test thermocouples temperature difference varied around ± 0.96 °C, the tested thermocouples' accuracy was acceptable for above mentioned experiment.

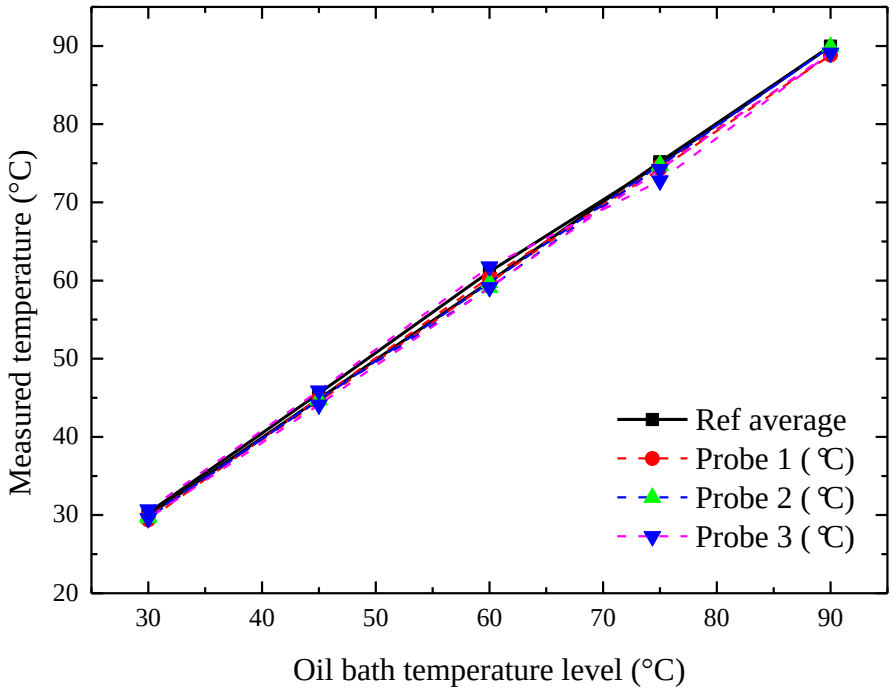

Figure 3.10: The thermocouples calibration results

3.3.2 T-history Analysis for Reference Material: KNO_3

The T-history analysis uses the lumped capacitance method to obtain the thermal properties of the PCMs [12]. To regard the sample to have a uniform temperature distribution, the Biot number (*Bi*) of the test sample has to be less than 0.1. In this experiment, the Biot number is influenced by the characteristic length of the tube, L_c, which in this experiment is the radius of the test tubes, *r*, heat transfer coefficient between the PCMs and the environment, *h*, and the thermal conductivity of the sample PCMs, *k*, as shown in Equation 3.1. The following calculations were done to ensure that the analysis can be assumed as the lumped capacitance method.

$$Bi = \frac{hL_c}{k} \tag{3.1}$$

KNO_3 was firstly chosen to be the reference material as it has a high melting point of 334 ℃ according to well know literature [4]. It does not undergo any phase transition in the temperature range of the T-history experiment. Figure 3.11 shows the cooling curve of KNO_3, from which the heat transfer coefficient h_1 can be determined.

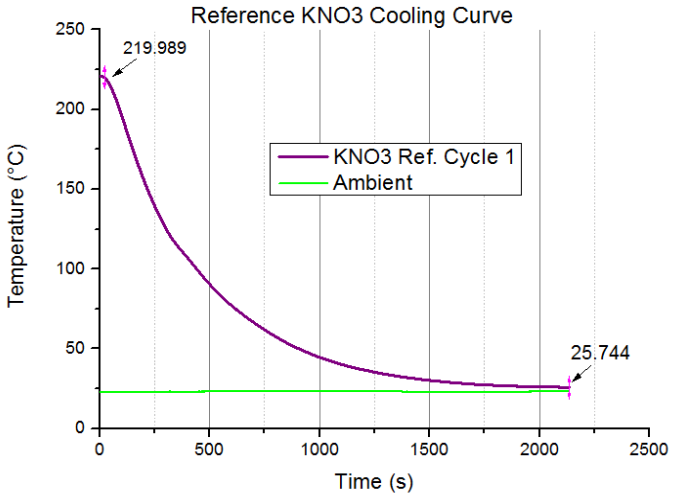

Figure 3.11: Cooling curve for KNO_3 as reference material

The general equation used for the experiment is shown in Equation 3.2. The heat stored by reference material and tube equals the heat loss by convection.

$$(m_t c_{p,t} + m_r c_{p,r})(T_0 - T_s) = hA_c A \tag{3.2}$$
$$A = \int_{t_0}^{t_1} (T_m - T_{amb})dt$$

where m_t is the mass of test tube, which is 0.062 kg (measured), $c_{p,t}$ is the mean specific heat of Pyrex test tube, which is 750 J/kg·℃, m_r is the mass of reference KNO_3, which is 0.01 kg (measured), $c_{p,r}$ is the mean specific heat of KNO_3 = 1210 J/kg·℃, T_0 is the initial temperature in the cooling process, which is 220.0 ℃ (measured), T_f is the final temperature, which is 25.7 ℃

(measured), A is area under temperature-time graph, which is 136444.69 (Obtained using OriginPro).

Another parameter to determine is the convective heat transfer area. The test tube filled with KNO_3 was assumed to be the cylinder as shown in Figure 3.12. The diameter of the test tube is approximately 0.02 m and KNO_3 was filled to the height of 0.041 m. Therefore, the convective heat transfer area, A_c, can be obtained to be 0.0032 m^2.

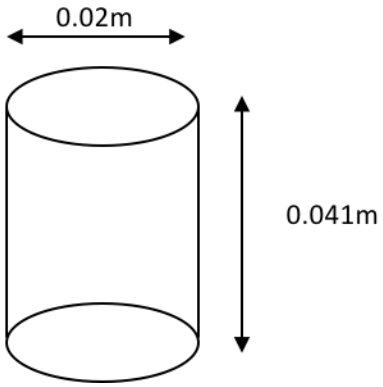

Figure 3.12: The cylinder assumed for calculation

Substituting the known values, the heat transfer coefficient can be derived, h_1, as shown in Equation 3.2. The heat stored by KNO3 and tube equals the heat loss by convection. h_1 was calculated to be 26.05 $W/m^2 \cdot ℃$.

In order to obtain an accurate heat transfer coefficient, the same experiment was conducted thrice using KNO_3 as the reference material. The repeated cycle 2 and 3 were plotted together with cycle 1 for comparison. All 3 curves appear to have a similar trend whereby temperature decreases at a decreasing rate, shown in Figure 3.13.

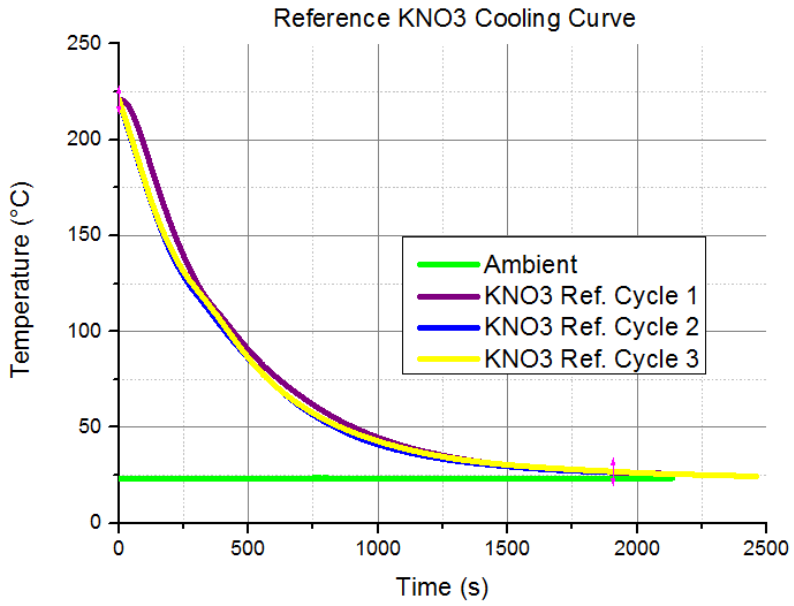

Figure 3.13: KNO_3 cooling curves for respective cycles

Three calculation results are shown in Table 3.2. The Biot number is calculated by Equation 3.1. The L_c in the equation can be calculated as follows. As mentioned before, the Biot number has to be less than 0.1 in order to apply the lumped capacitance method. Substituting in the h_{avg} and L_c in Equation 3.1, the thermal conductivity of the reference material has to be larger than 0.934 W/m K.

Table 3.1: Heat transfer coefficients for multiple tests

	h_1 (W/m^2 °C)	h_2 (W/m^2 °C)	h_3 (W/m^2 °C)	h_{avg} (W/m^2 °C)	L_c (m)	k (W/m^2 k)
Value	26.05	28.05	25.13	26.41	0.0036	$\geq$ 0.94

The heat transfer coefficient obtained using KNO_3 as the reference material was approximately 26.4 W/m^2.℃. One of the purposes of the experiment was to analyze the thermal properties of $LiNO_3$-KNO_3 eutectic salt mixture which has an average thermal conductivity of 0.52 W/m^2.℃. From the average heat transfer coefficient, the minimum required thermal

conductivity was calculated to be 0.94 W/m^2 ℃. As a result, the minimum thermal conductivity in order to assume the lumped capacitance method is out of the acceptable range as the eutectic salt mixture of $LiNO_3$-KNO_3 is only 0.52 $W/m^2 \cdot$℃

However, cross referencing with related research papers, the natural convective heat transfer coefficient of air should be within the range of 2 to 20 $W/m^2 \cdot$℃ [47]. One of the possible reasons for the above error may be caused by the agglomeration phenomenon of powdered KNO_3. Agglomeration of powdered KNO_3 was observed during the process of cooling, as shown in Figure 3.14. With the fine particles lumped into larger pieces, the thermocouples may not be directly in contacted with the reference material. In addition, agglomeration allows air gap to appear in the reference sample, therefore, affecting the recordings of temperature and the heat transfer.

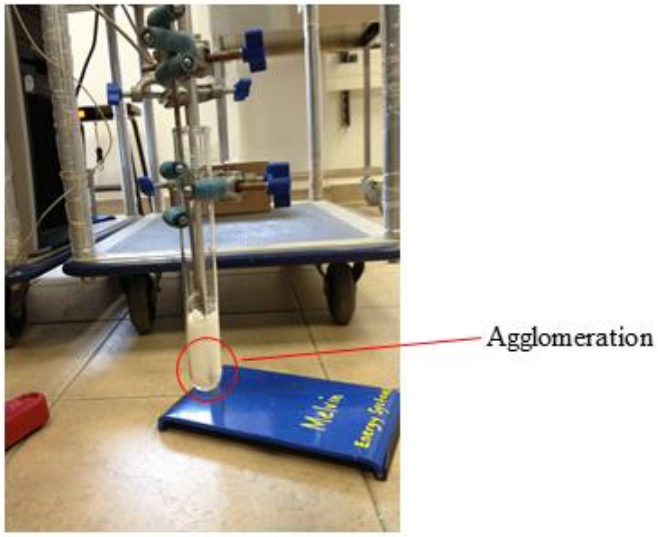

Figure 3.14: Agglomeration during cooling

3.3.3 T-history Analysis for Reference Material: H_2O

Previously, when the experiment was conducted using powdered KNO_3 as the reference material, the heat transfer coefficient obtained does not coincide with research articles and the thermal conductivity exceed the acceptable range. As such the lumped capacitance method cannot be assumed. To ensure the Biot number less than 0.1, together with the materials used in the experiment such as the test tubes and PCM samples, the same experiment above was conducted using distilled water.

Although the temperature range tested using distilled water does not coincide with the operating temperature of the PCMs, the main purpose of the reference sample is to obtain the heat transfer coefficient of the surrounding and to ensure that the Biot number is less than 0.1. The three cycle experiment results are shown in Figure 3.15. While the corresponding calculation results are presented in Table 3.2.

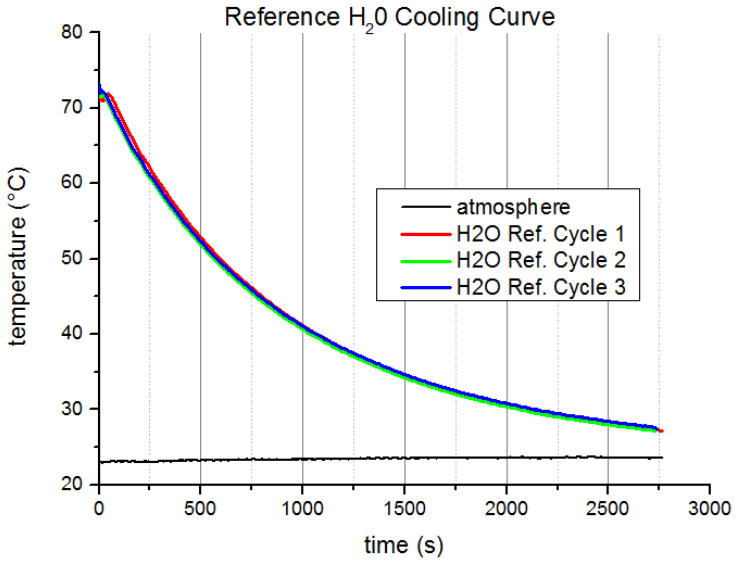

Figure 3.15: Reference H_2O cooling curve

Table 3.2: Calculation results for water experiment

	m_t (kg)	$C_{p,f}$ (J/kg ℃)	m_r (kg)	$C_{p,r}$ (J/kg ℃)	T_0 (℃)
Value	0.114	750	0.02	4186	71.9
	T_f (℃)	A (m^2)	A_c (m^2)	h_1 (W/m^2 ℃)	h_2 (W/m^2 ℃)
Value	27.1	107856.81	0.00534	13.12	12.94
	h_3 (W/m^2 ℃)	h_{avg} (W/m^2 ℃)	L_c (m)	k_{min} （W/m^2 K)	
Value	13.09	13.05	0.0036	0.466	

The average natural heat transfer coefficient obtained was approximately 13.05 W/m^2 ·℃ and this figure falls within the range described in different research articles [47]. Using the heat transfer coefficient obtained, the minimum thermal conductivity has to be around 0.466 W/m^2 ·℃. Since the thermal conductivity of $LiNO_3$-KNO_3 eutectic salt has an average value of 0.52 W/m^2 ·℃, the lump capacitance method can be applied to this modified T-history method.

3.3.4 T-history Analysis for Phase Change Materials

Similarly, the analysis of the PCM samples was done using the lumped capacitance method. However, the cooling process of the PCMs now involves a period of phase transition. As a result, the analysis of the PCM had to be broken down into three main sections before phase change, phase changing process and after phase change.

To determine the temperature point where phase change completed, a first derivative curve with respect to the cooling was plotted. According to literature readings, the minimum point of the first derivation curve can be regarded as the end of phase change [22]. This is because the temperature keeps constant or decreases gradually during the release of latent heat. However, the temperature decreases exponentially with only sensible heat. This can be shown in Figure 3.16.

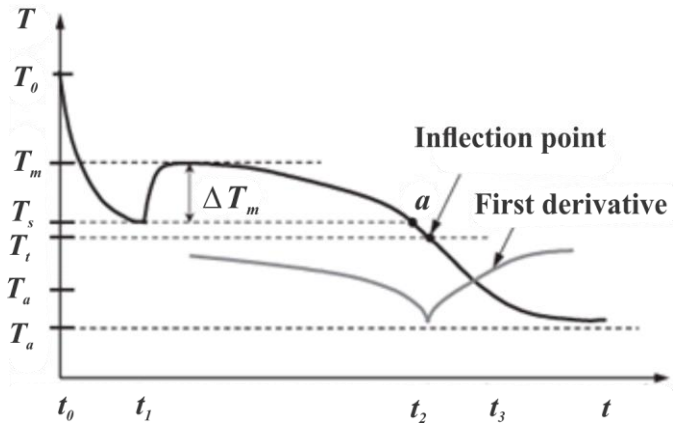

Figure 3.16: Using the first derivative to determine end of phase change process [22]

3.3.4.1 KNO_3-$LiNO_3$ (50 %-50 % wt.)

1) T-history Experiments

Figure 3.17 shows the cooling curve of KNO_3-$LiNO_3$ (50%-50% wt.) eutectic mixture. The green line represents the first derivative of the cooling curve while the red line symbolizes the ambient temperature. The beginning of the phase change temperature was estimated to be 118.44 ℃. The estimation was done by locating the point when the gradient of the cooling curve reached zero. The end of phase change temperature is approximately 103.17 ℃ and was established by using the first derivative curve as shown below. Similar experiments were conducted five times to improve the experimental accuracy, as shown in Appendix B.

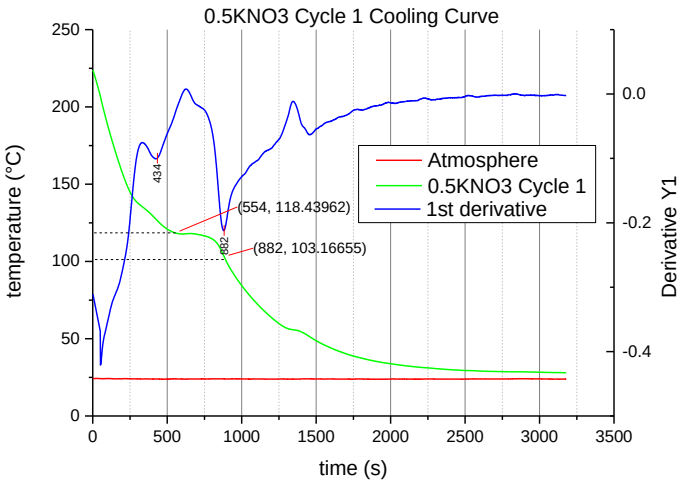

Figure 3.17: KNO_3-$LiNO_3$ (50%-50% wt.) cooling curve

From the five cooling curves of the previous section, a table which shows the phase change temperature was generated below in Table 3.3. $T_{m,1}$ represents the temperature when phase change begins while $T_{m,2}$ represents the end of phase change. An average temperature range is calculated using the 5 cooling curves obtained earlier and the phase change temperature range is between 98.60 ℃ and 116.16 ℃.

Table 3.3: Phase change range results for 0.5 KNO_3-$LiNO_3$

Test Cycle	1	2	3	4	5	6
$T_{m,1}$ (℃)	118.4	118.4	117.6	113.9	112.4	116.2
$T_{m,2}$ (℃)	103.2	103.4	93.2	95.2	98.0	98.6

2) DSC Experiments

The corresponding DSC results are shown in Figures 3.18 and 3.19. The average heat transfer temperature range is from 106.3 ℃ to 112.4 ℃, and the average heat of fusion is 118.68 kJ/kg.

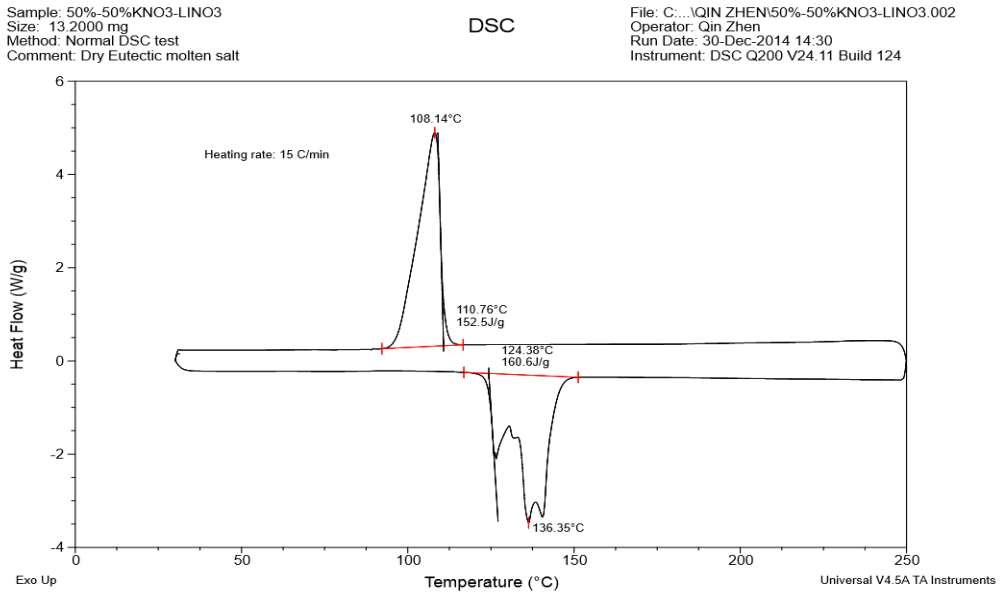

Figure 3.18: The 1st cycle of DSC experiment for KNO_3-$LiNO_3$ (50%-50% wt.)

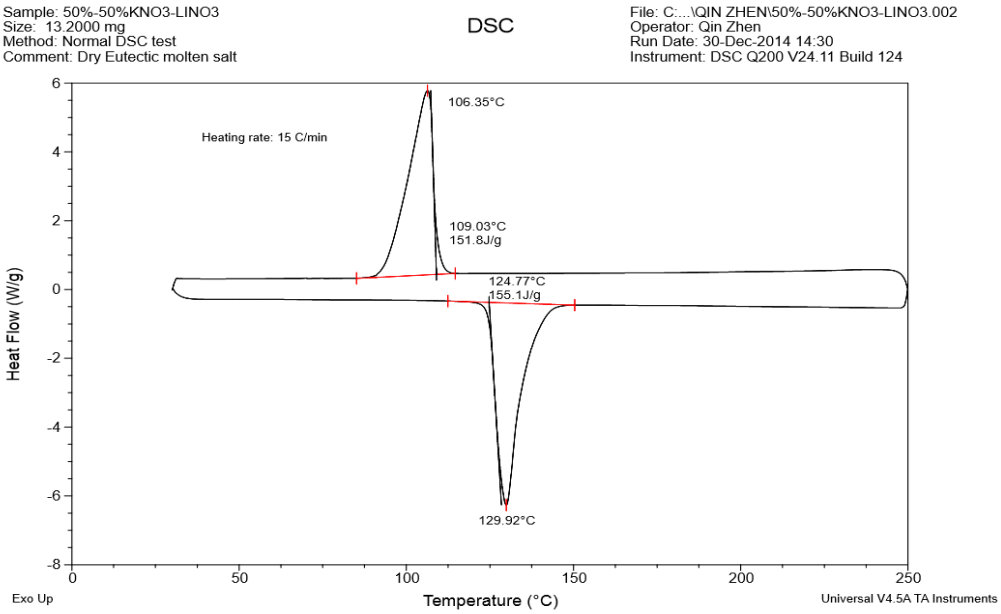

Figure 3.19: The 2nd cycle of DSC experiments for KNO_3-$LiNO_3$ (50%-50% wt.)

The results obtained with the DSC experiments of KNO_3-$LiNO_3$ (50%-50% wt.) had an average phase change temperature range between 106.3 ℃ to 112.4 ℃. On the other hand, the

T-history experiment method displayed a phase change range of 98.6 to 116.2 ℃. DSC method presented a temperature difference of around 6.1℃ while it was observed that the T-History method had a temperature difference of approximately 17.6 ℃.

3.3.4.2 KNO_3-$LiNO_3$ (60 %-40 % wt.)

1) T-history Experiments

Figure 3.20 shows the cooling curve of KNO_3-$LiNO_3$ (60 %-40 % wt.) eutectic mixture. The green line represents the cooling curve of the eutectic mixture, and the blue line represents the first derivative of the cooling curve while the red line represents the ambient temperature. The beginning of the phase change temperature was estimated to be around 111.72 ℃. The estimation was done by locating the point when the gradient of the cooling curve reached zero. The end of the phase change temperature is approximately 88.10 ℃ and was established by using the first derivative as shown below. Similar experiments were conducted five times and the results of the rest cycles were collected in Appendix B. Corresponding phase change temperature is shown in Table 3.4, where the average start and end of the melting range are 91.56 and 107.06 ℃.

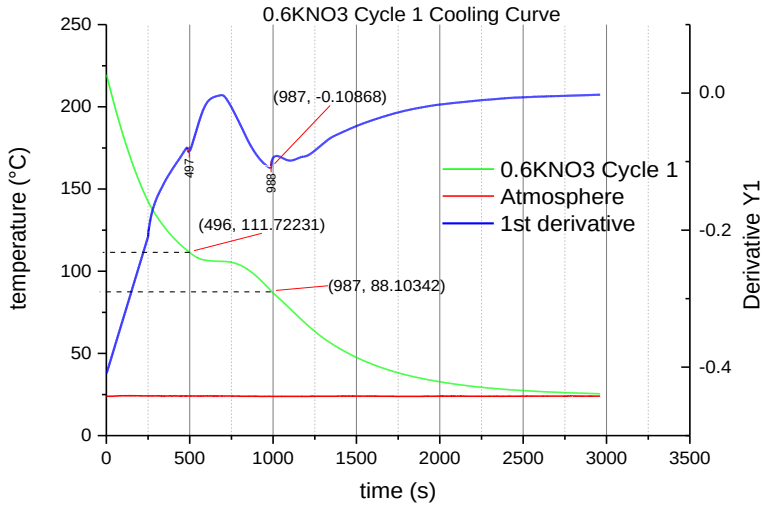

Figure 3.20: KNO_3-$LiNO_3$ (60 %-40 % wt.) 1st cycle cooling curve

Table 3.4: Phase change temperature for KNO_3-$LiNO_3$ (60 %-40 % wt.)

Test Cycle	$T_{m,1}$ (℃)	$T_{m,2}$ (℃)
1	111.7	88.1
2	107.5	96.9
3	106.5	88.3
4	107.1	93.6
5	102.5	90.8
Average	107.1	91.6

2) DSC Experiments

While the DSC results for KNO_3-$LiNO_3$ (60 %-40 % wt.) is shown in Figure 3.21. The average phase change temperature range is from 92.7 to 116.6 ℃.

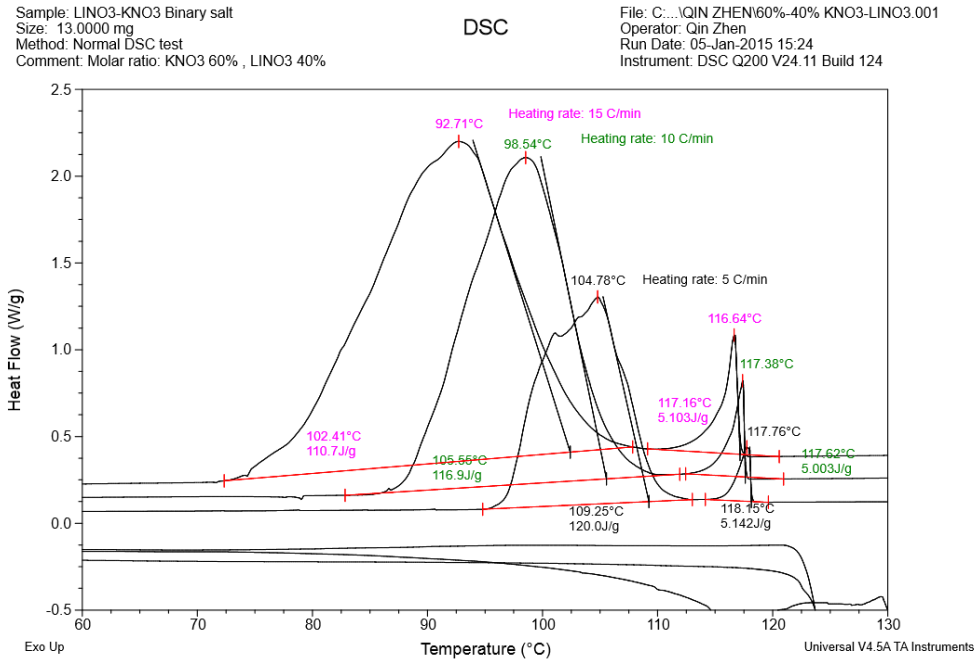

Figure 3.21: DSC experimental results for KNO_3-$LiNO_3$ (60 %-40 % wt.)

In addition, the phase change temperature range obtained using DSC and T-history method were 92.7 ℃ to 116.6 ℃ and 91.6 ℃ to 107.1 ℃ respectively. The temperature difference for the beginning and end of phase change is around 23.9 ℃ for using DSC method. On the other hand, the temperature difference is around 15.5 ℃ for the T-history method.

The heat of fusion obtained using the T-history method for the eutectic mixture of KNO3-$LiNO_3$ (60 %-40 % wt.) had an approximate value of around 85.43 kJ/kg. The same eutectic mixture of PCM conducted using the DSC method provided an average value of around 118.68 kJ/kg.

The difference in the temperature range between the two methods may be due to the following reasons. Firstly, there is a vast difference between the mass of PCM sample used for

the DSC and T-history method. DSC method used PCM with an only a mere mass of 0.0132 g while T-history method experiment was conducted with PCM of around 10 g. Secondly, DSC method was done with the samples enclosed in the calorimeter while the modified T-history method exposed the PCM samples to natural convection in room temperature. This resulted in uncertainties such as the varying room temperature, and changes in heat transfer coefficient with respect to time. Thirdly, the rate of cooling was controlled using the DSC method. A total of 3 different rates of cooling were conducted using the DSC method and the average value was taken. On the other hand, the rate of cooling for the T-history method was a free variable which varies with time. Lastly, the ratio of the eutectic mixture used in the DSC and T-history method may not be exactly similar. Therefore, these may cause a difference between the results of the T-history method and DSC method.

In addition, experimental errors in the T-history method may increase experimental inaccuracy. During the preparation of eutectic mixture, impurities may be deposited into the test samples during the process of grinding and drying. With impurities in the test sample, the results obtained may not be the actual results for the pure eutectic PCM. Secondly, when transferring the test sample into a test tube, there is a slight reduction of mass, thus affecting the overall experimental results. Lastly, when conducting the experiment in room temperature, it is difficult to ensure that environmental conditions remain constant throughout the whole experiment.

3.4 Summary

This chapter presents both the DSC and the T-history method experiments on some PCMs. The material test of paraffin wax shows its low melting point below 100 ℃ and can be applied as the low-temperature PCM in the experiment. While eutectic salts are favorable in the

high-temperature application. The measurement results of the two methods are compared and their difference is discussed. Both two methods are important for the selection of PCM. To apply T-history method on a high-temperature PCM, an oil bath can be considered as the heating source, which is more stable than the current heating block way. In the modified T-history method experiment, it was also found that the initial cooling temperature for PCM and the reference material can be different. The discrepancies of thermal properties obtained between the T-history method and the DSC test showed the difference between the small-scale materials and the bulk materials. In conclusion, the modified T-history method is capable of obtaining the thermal physical properties of bulk PCMs used in the actual application. It is also a cheaper and efficient alternative experimental method which increases the testing range of the test samples.

Chapter 4: Experimental Study on A Latent Heat Thermal Energy Storage Unit

4.1 Introduction

In the innovative gas turbine and Stirling engine cogeneration cycle, heat energy is extracted from the hot turbine exhaust gas, stored in the latent heat TES storage tank, then transferred to the heat transfer oil, which flows pass through the Stirling engine hot end heat exchanger as the heat source. Comparing to the conventional gas-liquid heat exchanger, the TES unit, which is the heat exchanger with the PCM, can stabilize the oil output temperature due to the latent heat of PCM. As the intermediate for energy storage, the TES tank plays a key role in the thermal energy transfer loop and its design significantly affects the energy storage rate and the Stirling engine power output. In this chapter, as the preliminary experimental study, one small heat exchanger with PCM for hot air thermal energy storage was fabricated and tested in the lab platform on its TES efficiency.

4.2 Experimental Preparations, Setup and Procedures

4.2.1 TES Unit Design

Various structures of TES unit have been proposed in the literature. Among them, the cuboid PCM encapsulation structure is popular due to its simple structure for fabrication, large contact area and small pressure drop. The cuboid design is adopted in the project since the pressure drop for the TES unit needs to be less than the back pressure of the turbine. An experimental prototype of TES unit was designed and manufactured, shown in Figure 4.1. The

TES unit consists of one stainless steel shell and five aluminum chambers filled with the PCMs. The two labeled chambers, B and D had four thermocouples to measure the PCM's temperatures individually. The thermocouples were labeled 101, 102, 301 and 302 for chamber B and 111, 112, 311 and 312 for chamber D. The position of each of the thermocouples is shown in Figure 4.2.

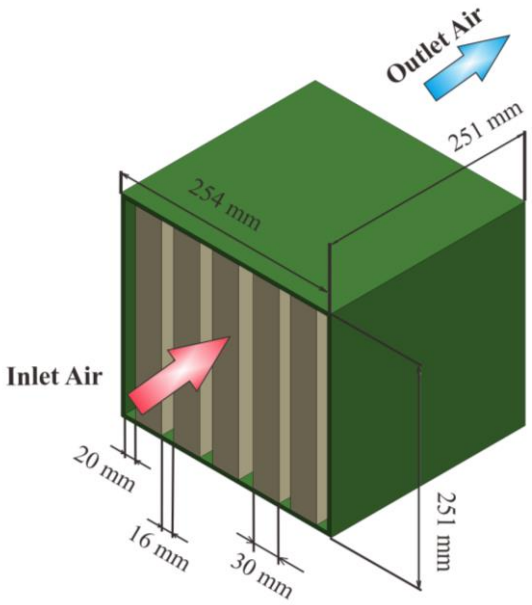

Figure 4.1: Schematic of TES unit with PCM

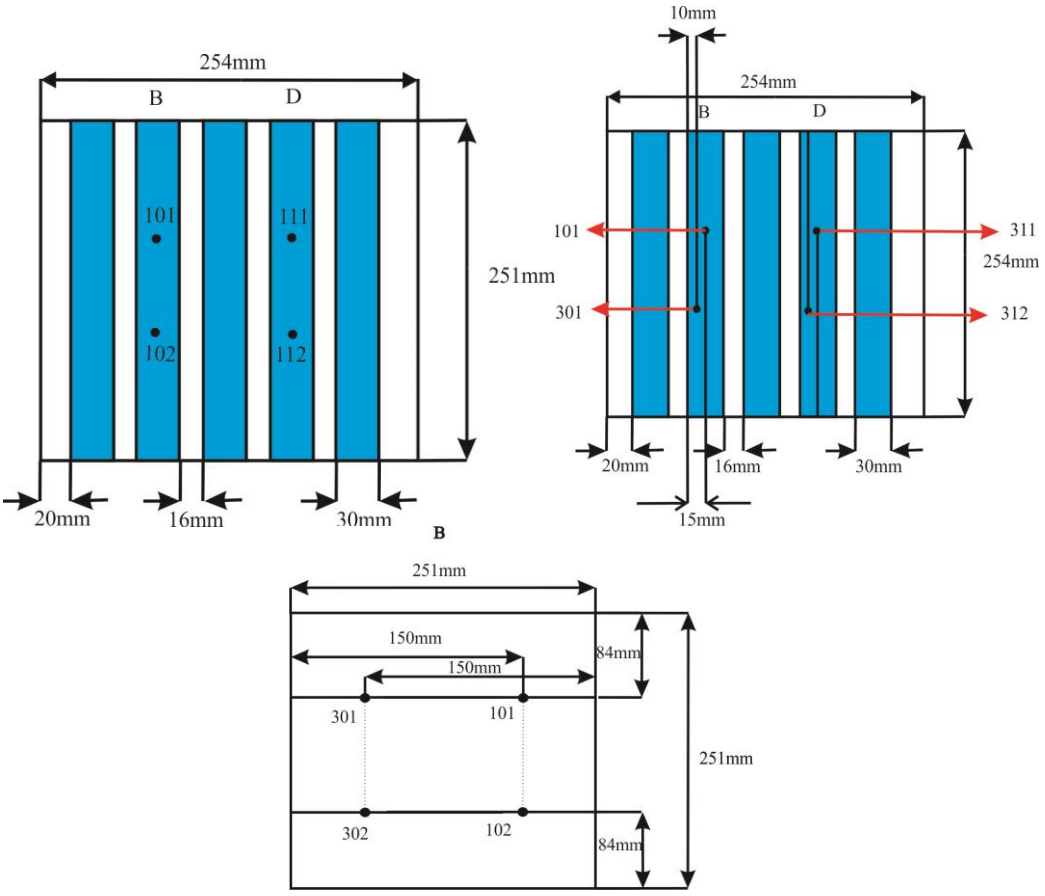

Figure 4.2: The Front view of the TES unit; b) The Top view of the TES unit; c) The Side view of the TES unit

4.2.2 PCM Selection

A PCM with a low melting point is needed to be filled in the TES unit as the storage media. To cooperate with the maximum temperature accessible in the lab platform, paraffin wax, whose melting range is near 50 ℃ is chosen to be the PCM in this experiment. The corresponding heating part of the DSC test result of the paraffin wax bought from VWR, Singapore is shown in Figure 4.3 and Table 4.1 shows the physical properties of the commonly used paraffin wax.

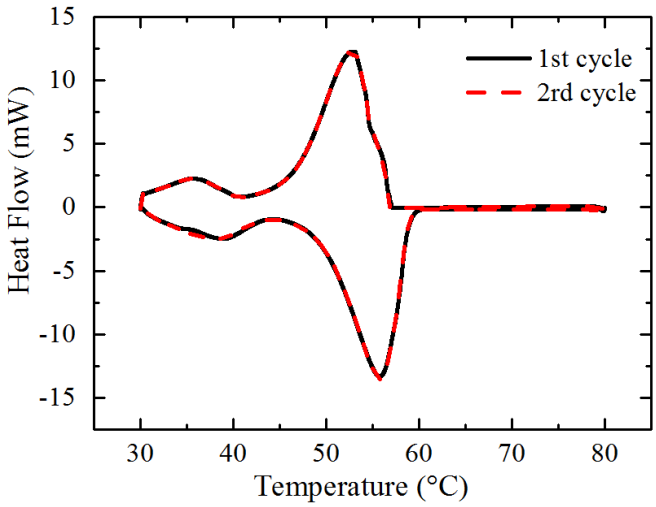

Figure 4.3: DSC curve of 6.9 mg paraffin wax under the heating rate 5 ℃/min.

Table 4.1: Physical properties of paraffin wax

Physical properties	Melting point (°C)		Freezing point (°C)	Latent heat (kJ/kg)	density (kg/m^3)	
Value	55.8		53	210	860 (Solid)	780 (Liquid)
Physical properties	Specific heat (kJ/kg K)		Thermal conductivity (W/m K)		Dynamic viscosity (N s/m^2)	
Value	2.9 (Solid)	2.1 (Liquid)	0.24 (Solid)	0.15 (Liquid)	0.205	

4.2.3 Experimental Setup

The test platform was modified from an air conditioning test unit. In the middle of the air duct, the original evaporator part was removed and then the designed TES unit can be integrated into the system. The test platform consists of a plastic duct with the rectangular cross section area, two power controllable coil heaters, a velocity adjustable axial fan and several mixers. The cross section dimension of the duct is 245 x 259 mm and the front wall of the duct is made of

PMMA and is removable. The two heaters are extended fin electric heating element type and are 1.0 kW each nominally at 220 V. There are one voltmeter and one ammeter for each heater and the fan respectively. The fan speed is adjusted by its controller on the panel. A damper at the duct outlet orifice can be adjusted to different positions in order to control the recirculation process. The mixers in the setup help the air to be more uniform. The schematic and the real experimental system are shown in Figure 4.4 and Figure 4.5 respectively. In this system, the air heated by the heaters would serve as the heat source to simulate the hot exhaust gas in the final project. In the experiment, the fan speed is set to be at the maximum for starting. The controller cannot be set below a certain value since it is essential that there is always some air flow through the duct to prevent over-heating. To prevent the heat loss, the temperature measurement part of the duct was insulated with Armacell class 0 armaflex of 13 mm thickness.

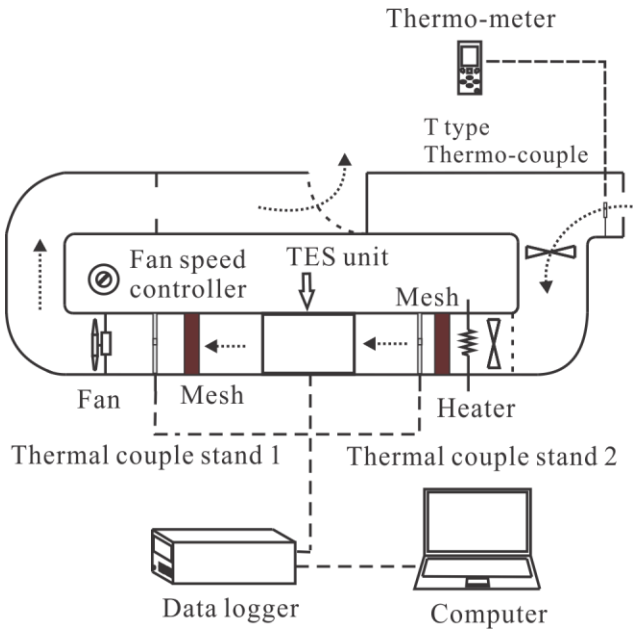

Figure 4.4: The experimental system schematic diagram.

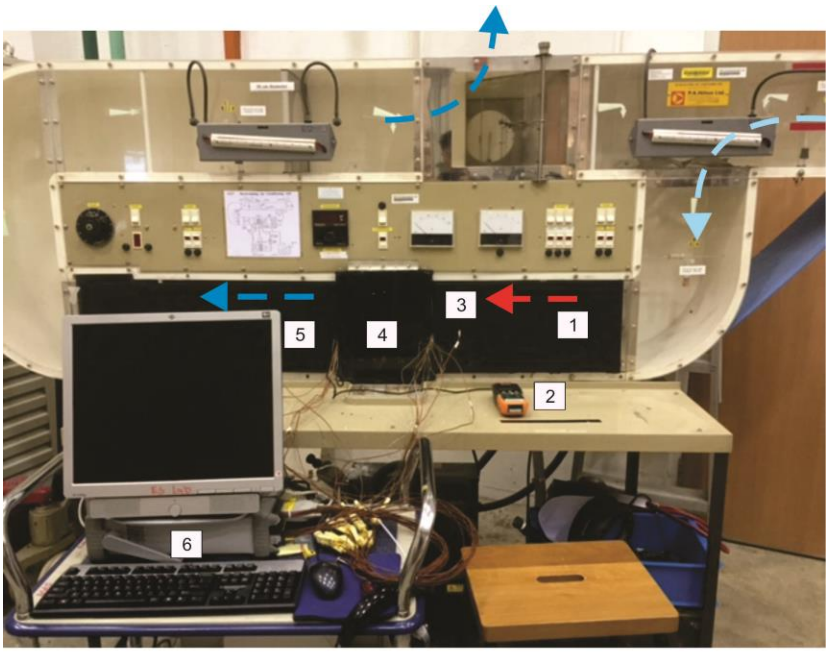

1-Pre heaters 2-Thermo-anemometer 3-Thermal couple for inlet air temperature
4-Thermal energy storage unit 5-Thermal couple for outlet air temperature
6-Data acquisition system

Figure 4.5: The actual setup of the test system

The Type K thermocouples were selected in the experiment as their working temperature range (-270~1260 °C) was suited for the working temperature range of the experiment, which is below 100 °C. To ensure the temperature measurement results are accurate enough, calibration was done firstly before the application. A similar calibration process was carried out following Section 3.3.1 previously. Figure 4.6 presents part of the calibration results. The results show that the thermocouples have an accuracy of ±0.5 ℃, which fits our requirement.

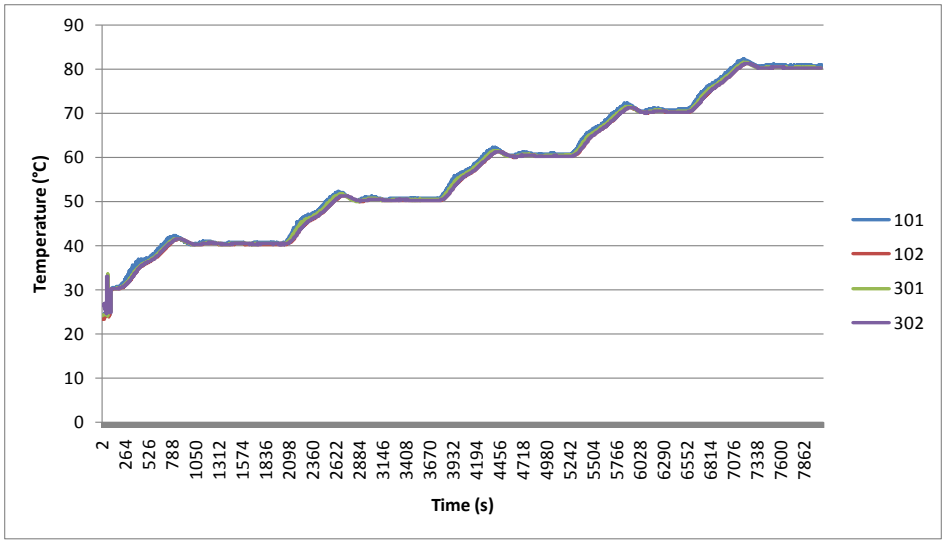

Figure 4.6: Calibration test results of the applied thermocouples

4.2.4 Experimental Procedures

In order to investigate the proper conditions required for the PCM to undergo phase change, a range of operating conditions were employed. A total of three fan speeds (25, 35, 45 rpm) and two heater powers (1, 2 kW) were used. The experiment was carried out for each fan speed and heater power. The charging process was started by setting the desired fan speed and turning on the desired heater power. After 4 h of the charging process, the heater was being switched off. After another 4 h, the discharging process was completed and the whole process was finished.

To compare the effectiveness of PCM in thermal energy storage, water and air were being used. PCM in chamber D was removed and replaced with water. The conditions were being fixed at 25 rpm and 2 kW and the experiment was also carried out for 8 h. After that, the water was being removed and an empty chamber was placed into the TES unit as shown in Figure 4.7 below. The similar procedures were repeated and results were being obtained from the data logger for analysis.

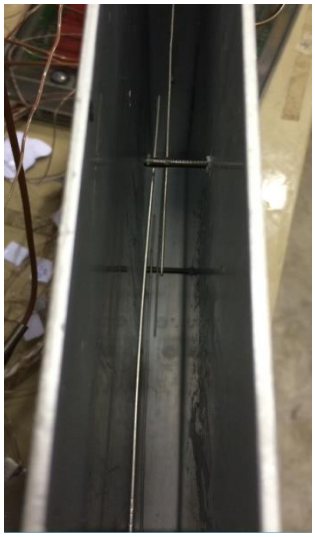

Figure 4.7: The empty PCM chamber

4.3 Insulation Performance Tests

Although with a careful insulation outside the wall of the air duct, heat loss in the experiment should not be overlooked, considering the relatively high temperature of the hot air and heaters. Heat loss mainly occurred around the heaters and succedent duct with the environment during the experiment. The objectives of carrying out the insulation performance tests are to determine the heat loss coefficient around the heaters α_1, and the heat loss coefficient in the test duct section α_2. The two parameters are important to calculate air mass flow rate and the heat transfer rate from air into the TES unit. The experiment setup is presented in Figure 4.8. The TES unit is not integrated into the duct during the insulation performance test, and the temperature data was taken by the DAQ system at the 9 inlet thermocouple positions and the 9 outlet thermocouple positions.

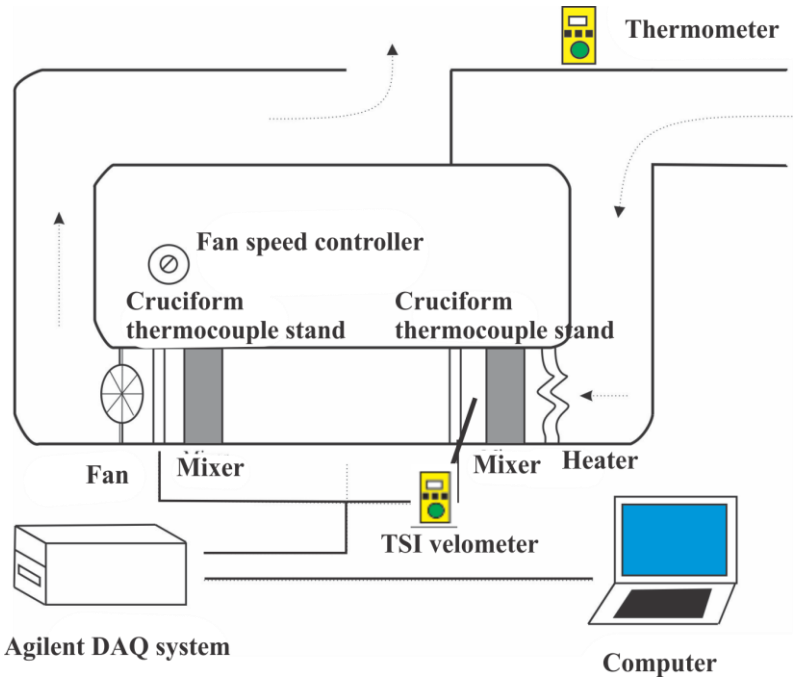

Figure 4.8: Schematic diagram of the insulation test setup

In the Insulation tests, fan speed was at 55 rpm and the heater power was at 1 kW at the beginning of the experiment. After the temperature was stablized, the heater power was increased to 2 kW. Once the air temperature had become stable again, the fan speed was reduced to 45 rpm and the heater power was reduced to 1 kW. This process was continued till the fan speed was reduced to 25 rpm at 10 per reduction and heater power at 2 kW.

4.3.1 The Heat Loss Coefficient Around Heaters α_1

The heat loss coefficient around the heaters α_1 can be determined through Equations (4.1) to (4.5) below.

$$Q_{heater} = Q_{eff} + Q_{loss} \tag{4.1}$$

$$Q_{eff} = C_p \dot{m} \left(T_{ave\ inlet} - T_{amb}\right) \tag{4.2}$$

$$\dot{m} = \rho v A_{duct} \tag{4.3}$$

$$Q_{loss} = \alpha_1 \left(T_{ave,1} - T_{amb}\right) \tag{4.4}$$

$$\alpha_1 = Q_{loss} / \left(T_{ave} - T_{amb}\right) \tag{4.5}$$

Where the Q_{heater} is the total heater power, Q_{eff} is the effective heater power used to heat up the air, Q_{loss} (W) is the part of heater power lost to the environment, C_p is the specific heat of air, m is the mass flow rate of air, $T_{ave,inlet}$ is the average temperature of air passing after heaters, T_{amb} is the ambient environment temperature, $T_{ave,1}$ is the average value of $T_{ave,inlet}$ and T_{amb}, which can be used to calculate α_1. The unit of heat loss coefficient α_1 is W/℃, which reveals the amount of heater power lost to the environment per unit temperature difference between hot air around the heater and the ambient.

Reading from the voltage and ampere meter, for the 1 kW heater, the average working voltage is 235 V and the average working current is 4.62 A. The measurement results mean that the real heating power for the 1 kW heater is 1085.7 W. Same method was also applied to the 0.5 kW heater, while the working voltage and current is 230 V and 2.21 A. Calculation shows that the real working power for 0.5 kW is 508.3 W. The reading accuracy of the voltage and ampere meter is ± 1 V and ± 0.1 A respectively.

The calculated heat loss coefficients under the tested working conditions are summarized in Table 4.1. Calibrated for different working conditions, the average heat loss power percentage, which symbolizes the amount of heater power lost to the environment during the heating is 23.2 %

± 2.4 %, and the average heat loss coefficient is 46.7 W/℃ ± 26 W/℃. The TSI hot-wire anemometer (accuracy: ± 5%) was put in the center of the duct after the heater for the air velocity measurements. The average value of the measured velocities was used as the average velocity under a working condition. Afterwards, the measured velocity was used to calculate the actual air flow mass flow rate. Also, an ideal mass flow rate estimated from the energy balance equation of air passing the heater was also calculated and compared with the measured air mass flow rate, as shown in Figure 4.9. The ideal condition was assuming no heater power loss and all the heater power was transferred into the internal energy of the air. As seen from Figure 4.9, when the fan speed was set at the same level, the measured mass flow rate had a little variation under different heater power. With the increasing fan speed, both the measured mass flow rate and the ideal mass flow rate increased. Besides, the measured mass flow rate was always lower than the ideal mass flow rate, which fit the fact that there existed heat loss in the test system.

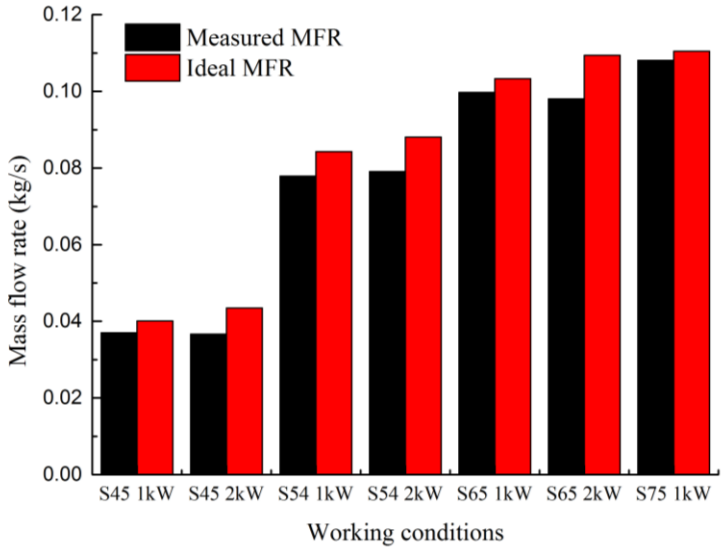

Figure 4.9: Comparison of measured mass flow rate with the ideal mass flow rate

Table 4.2: Calculated heat loss coefficients α_1 in the insulation tests

Working conditions	Heat loss power percentage	Heat loss coefficient α_1 (W/℃)
Fan speed: 45; Heater power: 1 kW	21.7 %	20.7
Fan speed: 45; Heater power: 2 kW	23.7 %	23.0
Fan speed: 54; Heater power: 1 kW	24.5 %	50.9
Fan speed: 54; Heater power: 2 kW	24.3 %	51.2
Fan speed: 65; Heater power: 1 kW	21.8 %	55.8
Fan speed: 65; Heater power: 2 kW	25.5 %	67.7
Fan speed: 75; Heater power: 1 kW	20.8 %	57.2
Average value	23.2 %	46.7

4.3.2 The Heat Loss Coefficient in The Duct α_2

The heat loss in the duct affects the calculation of TES instantaneous heat transfer rate, which is one of the parameters to evaluate the TES unit heat storage performance. Thus a similar insulation performance test is necessary to determine the heat loss coefficient in the duct α_2. A similar analysis to calculate α_2 has been done as the way to determine α_1. The equations needed are as follows.

$$Q_{loss} = \alpha_2 (T_{ave,2} - T_{amb}) \tag{4.6}$$

$$Q_{loss} = C_p \dot{m} (T_{ave,in} - T_{ave,out}) \tag{4.7}$$

$$T_{ave,2} = (T_{ave,in} + T_{ave,out}) / 2 \tag{4.8}$$

$$\dot{m} = \rho v A_{duct} \tag{4.9}$$

$$\alpha_2 = Q_{loss} / (T_{ave,2} - T_{amb}) \tag{4.10}$$

Figure 4.10 presents the average inlet temperature of the 9 thermocouples in the inlet stand and the average outlet temperature in the outlet stand during the insulation performance tests. The temperature difference was much higher for the 2 kW than the 1 kW at all fan speeds. Table 4.3 presents the results of insulation performance test in the duct. The average heat loss power and average heat loss coefficient α_2 are calculated. Results show that the average loss power in the duct to the environment is 63.4 W ± 30.8 W and the average heat loss coefficient α_2 is 5.3 W/℃ ± 2.9 W/℃. The α_2 is useful to predict the heat loss in the duct.

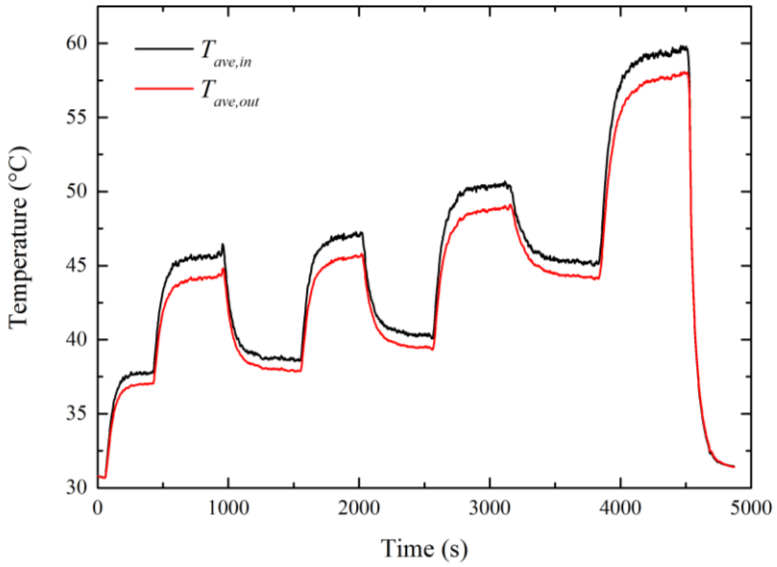

Figure 4.10: Temperature history of average inlet temperature and outlet temperature to determine α_2

It is interesting to compare the temperature distribution in the two thermocouple stands. Through analyzing the temperature distribution, the heat loss may have a reasonable explanation. Two working conditions are chosen to be investigated. The heater power was set at 2 kW and the air velocity fluctuates from 1.65~1.75 m/s measured by the hot-wire anemometer, (brand: TSI, accuracy: ± 5%). Figure 4.11 showed the temperature measurement results in the thermocouple 9 inlet positions and the 9 outlet positions. The main temperature difference comes from

thermocouple point 107. The maximum difference reaches 8.6 ℃. While for each point, the maximum standard deviation is ± 0.39 ℃. The average inlet temperature is 53.43 ℃, while the outlet average temperature is 51.47 ℃. The difference between them is 1.96 ℃, which occupies 3.7 % of the inlet average temperature. The reason for the temperature difference in the horizontal second point and the fifth vertical point may be caused by the position differences of the thermocouple test points.

Table 4.3: Calculated heat loss coefficients α_2 in insulation tests

Working conditions	Heat loss power (W)	Heat loss coefficient α_1 (W/ ℃)
Fan speed: 45; Heater power: 1 kW	53.1	2.4
Fan speed: 45; Heater power: 2 kW	35.5	0.8
Fan speed: 54; Heater power: 1 kW	52.8	5.2
Fan speed: 54; Heater power: 2 kW	94.0	4.7
Fan speed: 65; Heater power: 1 kW	61.5	7.5
Fan speed: 65; Heater power: 2 kW	126.8	8.0
Fan speed: 75; Heater power: 1 kW	61.9	8.1
Average value	63.4	5.3

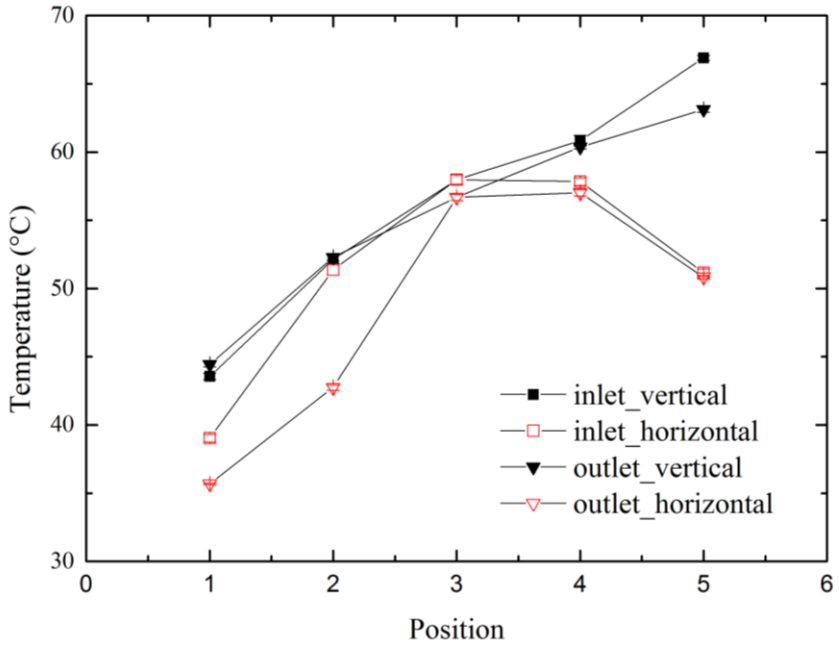

Figure 4.11: Insulation performance temperature results

In conclusion, the heat loss to the surroundings was kept minimal at high fan speed and low heater power. Even at low fan speed and high heater power, the heat loss to the surroundings was relatively low. Therefore, current insulation was effective in insulating the system. In addition, from the insulation experiment, the heat loss coefficient will be considered to make the TES performance investigation more accurate.

4.4 Results and Discussion

Three parameters were changeable in the experiments: the heater power, the fan speed, which controls the mass flow rate of air and the storage media. The detailed tested working conditions are listed in Table 4.4. The PCM inside temperatures, the instantaneous charging and discharging power, the heat stored in the test unit, and the charging or discharging efficiency were investigated.

Table 4.4: Tested working conditions summary

Heater power/ kW	Fan speed/ RPM	Storage media
1	25	Water
2	35	Air (empty chamber)
	45	Paraffin wax (VWR)

4.4.1 Effect of Heater Power on PCM Melting

The heat load in the test, which is the heater power, will affect the temperature increase of the inlet air. The higher heater power would cause a higher air temperature. The PCM melting curves of the same position (chamber D, position: 311) under two heater powers were compared, as shown in Figure 4.12. The fan speed was 25 rpm at both working conditions. It is clear that the increasing heater power significantly increased the PCM melting rate. At the end of the PCM charging process, the highest temperatures of position 311 at 1 kW and 2 kW are 52.4 ℃ ± 0.5 ℃ and 62.6 ℃ ± 0.5 ℃ respectively. A "sudden jump" of temperature appeared under 2 kW at around 11625 s. The cause of this phenomenon may be because the natural convection uniformized the temperature distribution inside the liquid paraffin wax, while it would cause a temperature gradient between the unmelted solid paraffin wax and the liquid one. When the solid paraffin fin melted, its temperature would be quickly uniformized and this process was measured by the thermocouple at this position, thus causing such temperature jump. It is interesting to discover the relationship of the appearance of the sudden jump with the hot surface temperature in the future work.

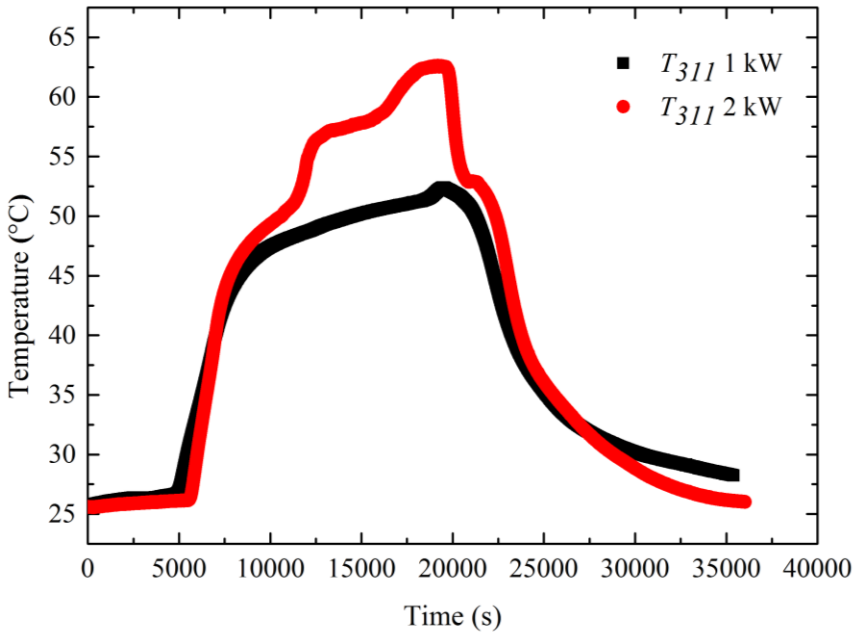

Figure 4.12: Temperature history of the PCM at position 311 of chamber D under 1 kW and 2 kW heater power at fan speed 25 rpm

To make a more comprehensive comparison, the temperature curves of PCM at positions 311 and 312 of chamber D under 1 kW and 2 kW heater power at fan speed 25 rpm are presented in Figure 4.13. It can be seen that at 1 kW, the melting curve of PCM at 311 has nearly no difference with the one at position 312, except that at the end of heating at position 311, there existed a trend to appear the temperature jump. The appearance of the sudden jump means the paraffin wax at the specific position has been completely melted. From this finding, it can be concluded that the under a uniform heating boundary condition, the upper PCM would melt firstly due to the natural convection inside the liquid PCM. This conclusion can be verified from the temperature curves at 1 kW, where the temperature curve of position 311 experienced the temperature jump firstly. It was also found that the temperature jump temperature is not changeless. Observed from the temperature curve of position 312 at 2 kW. The paraffin wax

temperature increased to around 55.1 ℃ ± 0.5 ℃ before the temperature jump. While the blue line experienced the temperature jump at around 51.0 ℃ ± 0.5 ℃.

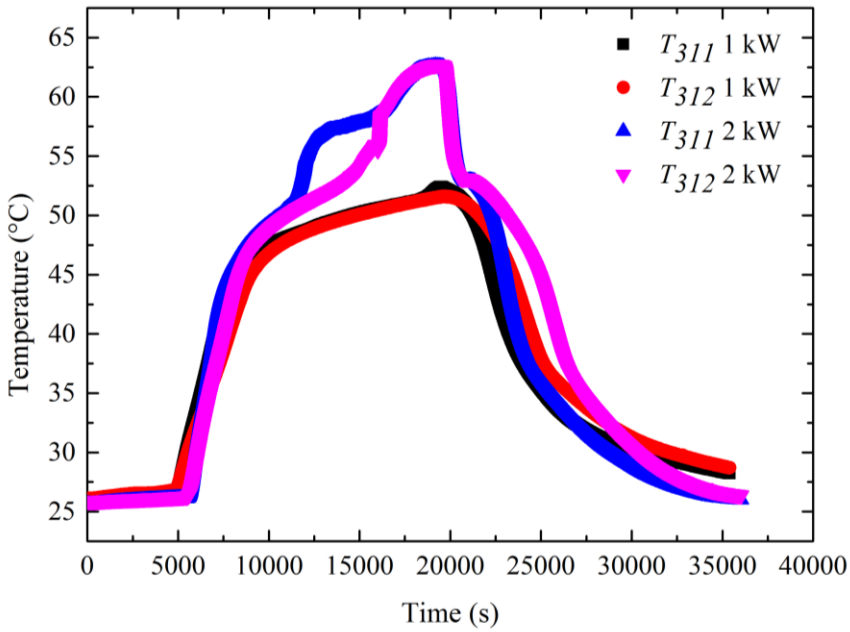

Figure 4.13: Temperature history of the PCM at positions 311 and 312 of chamber D under 1 kW and 2 kW heater power at fan speed 25 rpm

4.4.2 Effect of Fan Speed On PCM Melting

Another controllable parameter is the fan speed, which affects the mass flow rate of the air directly. Figures 4.14 and 4.15 present the comparison of the PCM temperatures at the middle section and the one-third section under different fan speeds in chamber D. The heater power was at 2 kW for these working conditions. It is shown from both Figures 4.14 and 4.15 that at lower fan speed, the PCM would melt faster. While at a lower speed at 25 rpm and 35 rpm, the sensible heating parts of the PCM temperature curves were nearly the same, except the melting curves. At 45 rpm, the PCM inside the chamber D did not experience the phase change or partially melting

and were not completely melt during the experiment. While different from the effect of the heater power, the fan speed also affects the cooling part of the PCM. Under a faster fan speed, the PCM would freeze faster. In Figures 4.14 and 4.15, it is shown that the PCM in 45 rpm decreased to the room temperature firstly, the 35 rpm case coming second the 25 rpm case coming last. It is also interesting to found that the upper position 112 always has a faster freezing rate than the lower position 112.

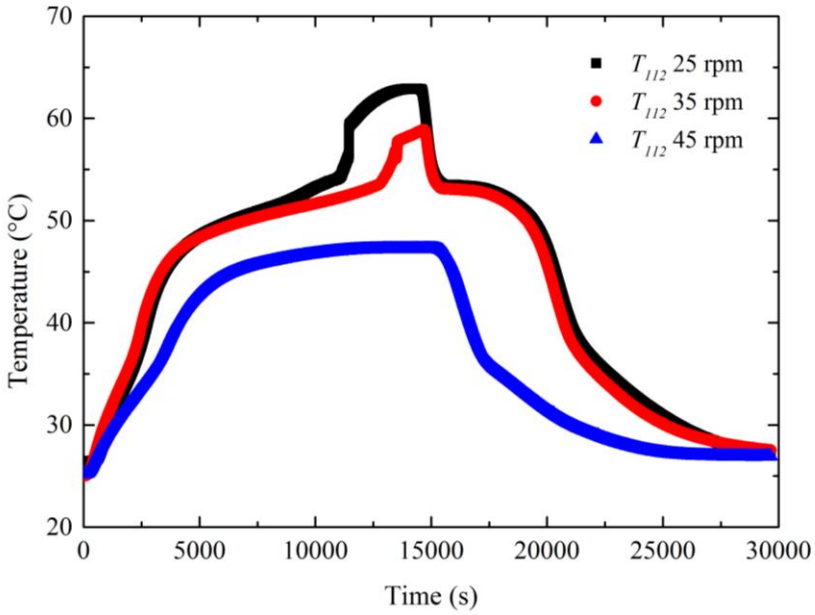

Figure 4.14: Comparison of the PCM temperatures at the middle section

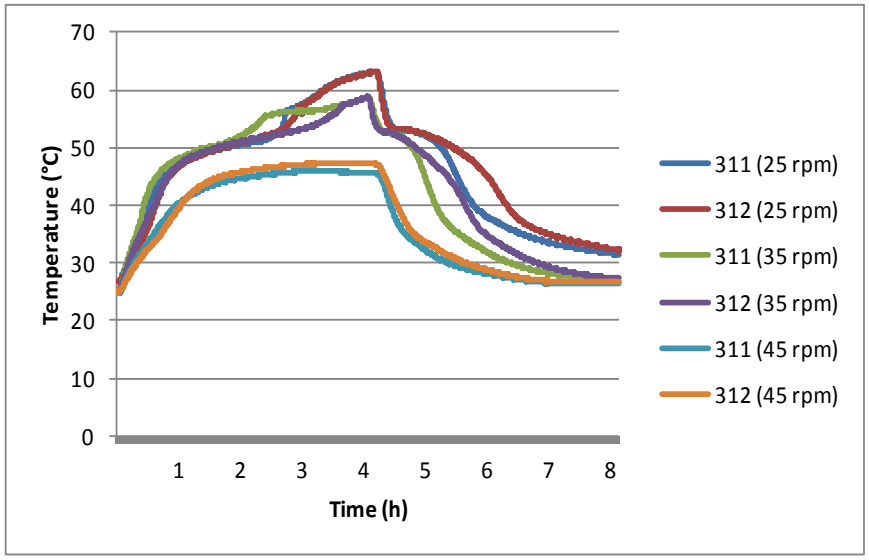

Figure 4.15: Comparison of the PCM temperatures at the one-third section

4.4.3 Instantaneous Heat Transfer Rate to The TES Unit

To investigate the TES unit performance over time, the instantaneous heat transfer rate was required. Therefore, to calculate the instantaneous heat transfer rate, a few equations were required. Firstly, by the first law of the thermodynamics, the following equation can be obtained. This equation is based on the quasi-steady conditions assumption.

$$\dot{Q}_{ins} = \dot{m} C_{p,air} (\bar{T}_{inlet} - \bar{T}_{outlet}) \tag{4.11}$$

where Q_{ins} is the instantaneous heat transfer rate, $\bar{T}_{inlet}$ and $\bar{T}_{outlet}$ is the average inlet and outlet temperatures. The air mass flow rate was calculated based on Equation (4.9) and the calculated heat loss coefficients. In the calculation, the specific heat and density of air are assumed constants, where the $C_{p,air}$ was 1.005 kJ/kg and the ρ_{air} was 1.225 kg/m^3.

Figure 4.16 presents the calculated instantaneous heat transfer rate at different working conditions. It is shown that during charging, the highest instantaneous heat transfer rate was at 25

rpm and 2 kW, followed by 35 rpm and 2 kW and then 45 rpm and 2 kW, 25 rpm 1 kW, 35 rpm 1 kW and lastly 45 rpm 1 kW. This result was expected as the highest temperature was recorded at 25 rpm and 2 kW. The energy stored per unit time decreased over time as the temperature difference between the PCM and inlet air decreased. As the temperature difference decreased, the heat transfer rate also decreased and thus lesser energy was being stored.

During discharging, the positive instantaneous heat transfer rate turned negative as energy was being released. Two distinct groups can be separated by the heater powers. Those at 1 kW measured a lower instantaneous heat transfer rate as compared to those at 2 kW which is similar to the charging process. For all the working conditions, the instantaneous heat transfer rate gradually increased close to 0 W. Similar to the charging process, the energy stored per unit time gradually increased to 0 as the temperature difference between the PCM and inlet air decreased. As the temperature difference decreased, the heat transfer rate also decreased resulting in lesser energy being released.

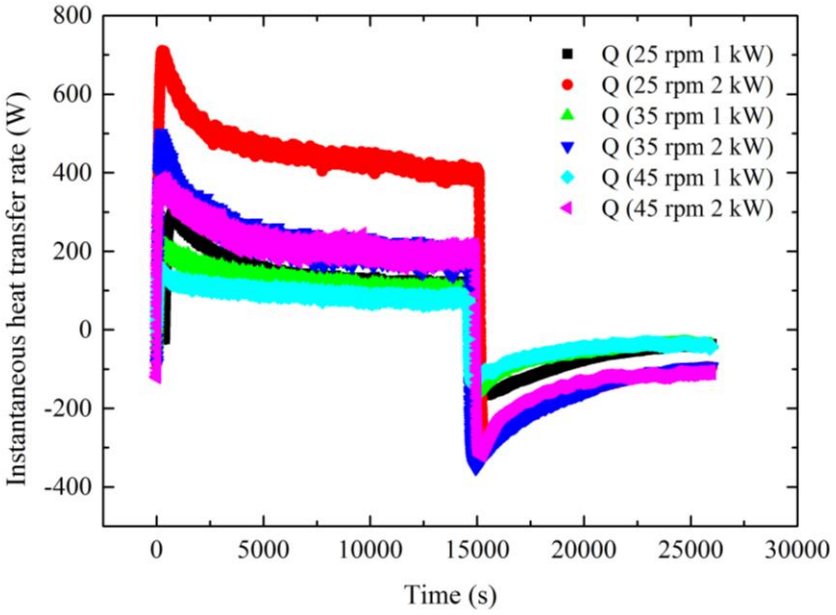

Figure 4.16: Instantaneous heat transfer rate of the TES unit at different working conditions

In conclusion, the most energy stored per unit time was at 25 rpm and 2 kW which proved that it was the most optimal working condition compared to the others. In addition, the heater power affected the instantaneous heat transfer rate significantly as compared to the fan speed.

4.4.4 Comparison of Paraffin Wax to Water and Air

To investigate the effectiveness of paraffin wax in thermal energy storage, comparison with water and air were made. To show the drastic difference between paraffin wax and water and air, the optimal condition was chosen. The fan speed and heater power were set to 25 rpm and 2 kW respectively. Figures 4.17 and 4.18 below shows the comparison of paraffin wax, water, and air at the stated conditions.

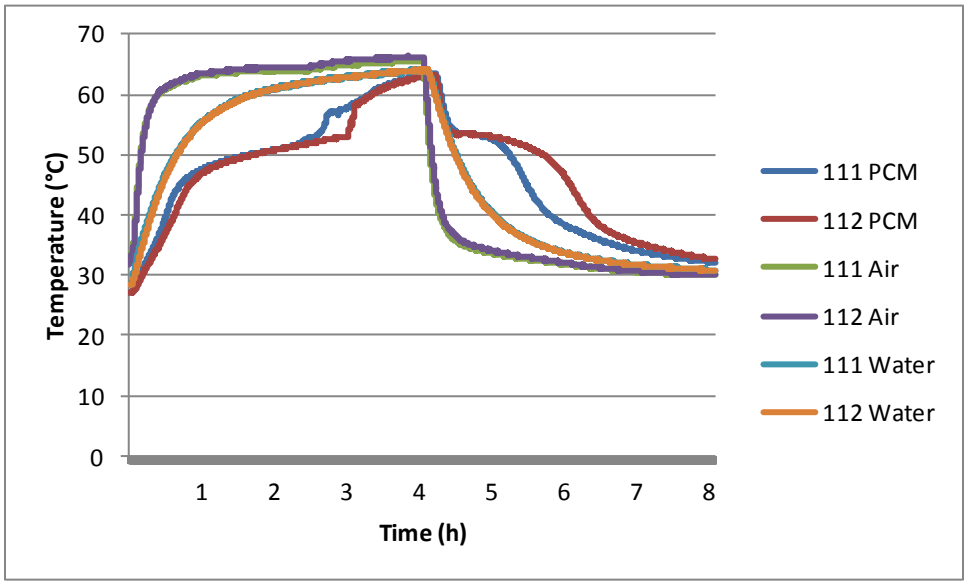

Figure 4.17: Comparison of temperatures in the middle of chamber D

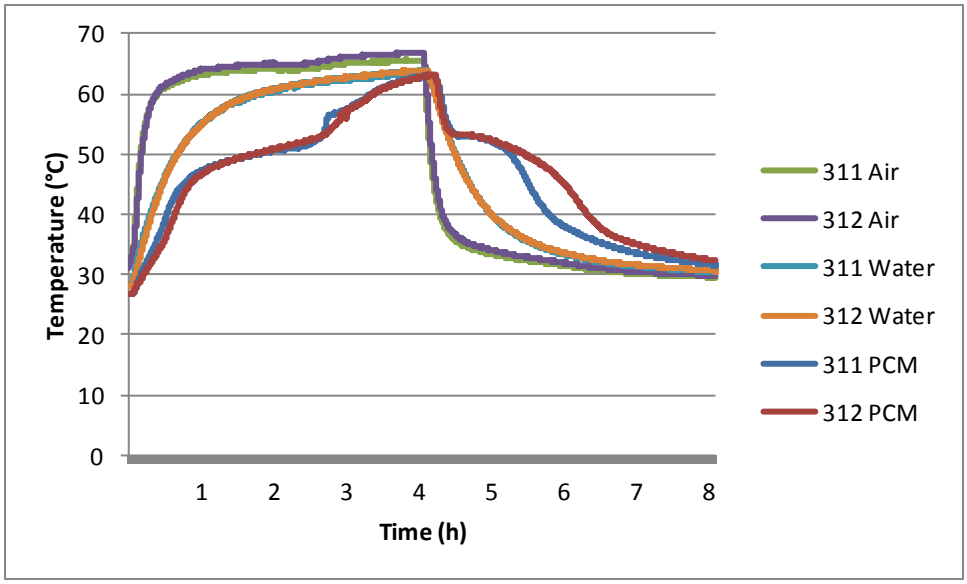

Figure 4.18: Comparison of temperatures in the one-third position of chamber D

For both Figures 4.17 and 4.18, comparing the heating curves of air and water, a higher peak temperature was attained by air at 65 °C as compared to 62 °C by water. In addition, the gradient of the heating curve of air was close to 1 which is much steeper than water. During cooling, the gradient of the temperature curve of air was also much steeper than water. Therefore, from the results air heats and cools down faster than water.

For both the graphs, comparing all three heating curves, paraffin wax and water recorded the highest temperature at 62 °C. Phase change was also observed for paraffin wax over the range of 46- 53 °C while phase change was not observed for both water and air. In addition, the gradient of the temperature curve of air was the steepest followed by water then paraffin wax. For cooling, phase change was observed again for paraffin wax at 53 °C but not observed for air and water. Also, the cooling curve gradient followed the trend of the heating curve.

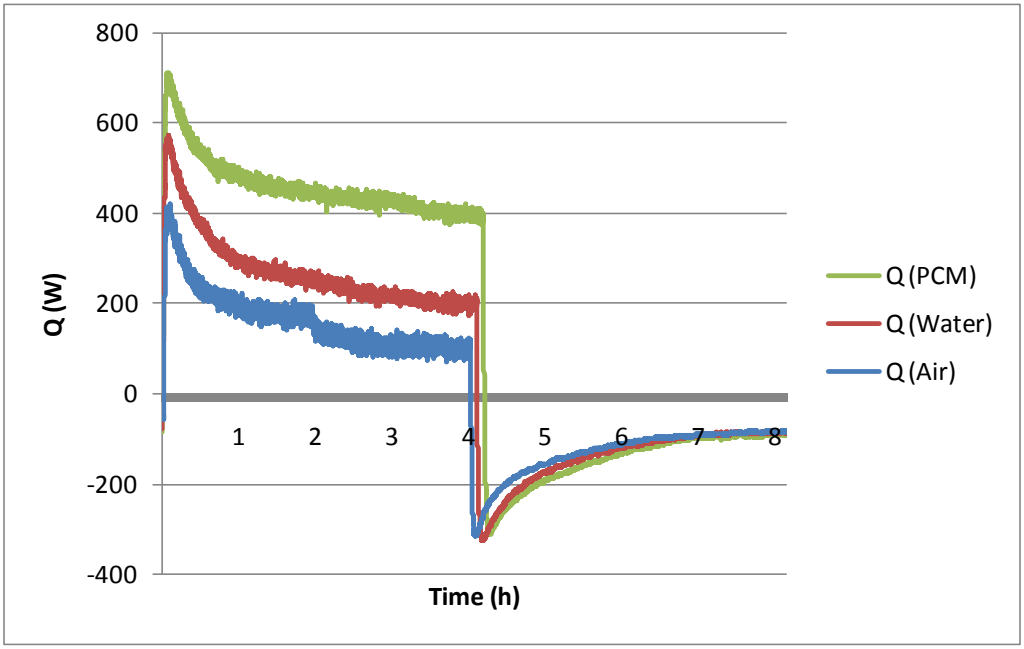

Figure 4.19: Energy stored per unit time of PCM, water, and air

As shown from Figure 4.19, during charging, the most energy stored per unit time was PCM followed by water then air. During discharging, the amount of energy discharged was relatively similar for all the materials. From this results, paraffin wax was the ideal choice over water and air as it had the most energy stored per unit time during charging. In conclusion, for this experiment's temperature range, paraffin wax was able to undergo phase change unlike air and water. In addition, paraffin wax had the highest energy stored per unit time during charging. Therefore, paraffin wax was chosen over water and air.

4.5 Summary

In this chapter, the hot air thermal energy storage with PCMs is presented and the thermal energy storage unit is evaluated under different working conditions. The PCM chambers in the designed TES unit were tested experimentally. From the results, due to the non-uniform temperature and air flow distribution, chamber D was more efficient and optimal at various

working conditions. The efficiency of the designed TES unit and its performance under various working conditions were investigated experimentally, the fan speed and heater powers were analyzed and based on the experimental results, at low fan speed and high heater powers, phase change was achieved by the PCM in the TES unit in chamber D. Instantaneous heat transfer rate was calculated from the experimental results. Based on the results, the effects of heater powers were more significant as compared to fan speed. At 2 kW, the amount of energy stored per unit time was higher than at 1 kW only when comparing at the same heater power was the effects of fan speed significant. The usage of PCM in a TES unit was also tested experimentally. Both water and air were used in comparison with paraffin wax. Based on the experimental results, both air and water did not undergo phase change unlike paraffin wax and therefore, paraffin wax achieved its goal by undergoing phase change. In addition, by calculating the instantaneous heat transfer rate, the amount of energy stored per unit time was obtained. From the results, PCM managed to store the most energy per unit time during charging as compared to water and air.

Chapter 5: Numerical Simulation of the Thermal Energy Storage Unit

5.1 Introduction

This chapter presents the numerical simulations based on the experiment in Chapter 5. A Two-D numerical simulation was conducted and its results were compared with the experiment results before carrying out the Three-D numerical simulation. The average temperatures of the outlet air and positions inside PCMs in the simulation results were compared with the corresponding experiment data in order to verify the numerical model. The validity of the numerical model allows us to trust the simulation study on the final design of the TES system.

5.2 Two-Dimensional Numerical Simulation

5.2.1 Geometry and Model Introduction

This numerical simulation was carried out through commercial simulation software, COMSOL Multiphysics (version: 5.1), which is created based on the finite element method. Geometry is needed as the first step of the simulation. Captured from the experiment setup, an air duct, and three PCM chambers, along with their five aluminum chambers, were built in COMSOL, as shown in Figure 5.1. Considering the symmetry characteristic of the geometry, only half was built to save the computational cost.

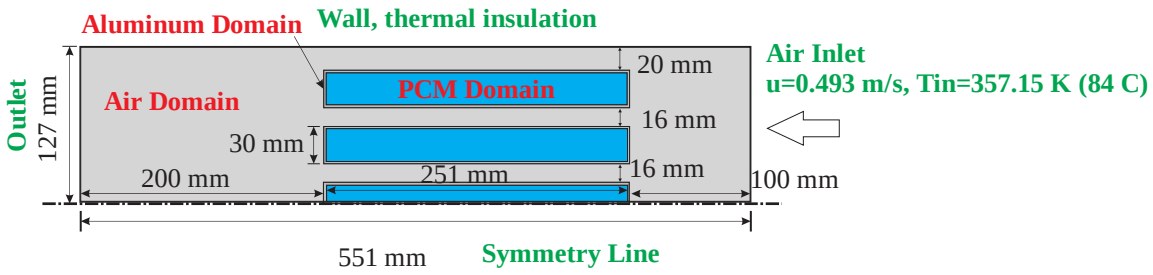

Figure 5.1: Geometry built for the two-dimensional numerical simulation

To simulate the air flow across the chambers and the heat transfer process in the air, aluminum cases and the inside PCM, both computational fluid flow (CFD) model and heat transfer model are needed. Since the Reynolds number was calculated to be 4237 based on the boundary condition shown later, it is reasonable to apply the Turbulent flow *k*-ε model in the air flow domain, and the heat transfer model was applied in the whole domain. Both the two models are embedded inside COMSOL Multiphysics. The specific governing equations for Turbulent flow *k*-ε model are shown in Equations (5.1) to (5.6). Equations (5.7) to (5.8) present the heat transfer governing equations used in the aluminum domain and air flow domain. In detail, the turbulent viscosity, μ_T, is modeled in Equation (5.5), where C_μ is a constant. Equation (5.3) presents the transport equation for *k* reads in the *k*-ε model, where the P_k is the production term. Equation (5.4) presents the transport equation for ε reads. The constants involved in these equations, C_μ, C_{e1}, C_{e2}, σ_k, σ_ε, are set as the default values, 0.09, 1.44, 1.92, 1.0, 1.3 according to the COMSOL manual.

$$\rho\frac{\partial u}{\partial t}+\rho(u\cdot\nabla)u=\nabla\cdot[-\rho I+(\mu+\mu_T)(\nabla u+(\nabla u)^T]+F \tag{5.1}$$

$$\rho\nabla\cdot(u)=0 \tag{5.2}$$

$$\rho\frac{\partial k}{\partial t}+\rho(u\cdot\nabla)\varepsilon=\nabla\cdot[(\mu+\frac{\mu_T}{\sigma_k})\nabla k]+P_k-\rho\varepsilon \tag{5.3}$$

$$\rho\frac{\partial\varepsilon}{\partial t}+\rho(u\cdot\nabla)k=\nabla\cdot[(\mu+\frac{\mu_T}{\sigma_\varepsilon})\nabla\varepsilon]+C_{e1}\frac{\varepsilon}{k}P_k-C_{e2}\rho\frac{\varepsilon^2}{k},\varepsilon=ep \tag{5.4}$$

$$\mu_T=\rho C_\mu\frac{k^2}{\varepsilon} \tag{5.5}$$

$$P_k=\mu_T[\nabla u:(\nabla u+(\nabla u)^T)] \tag{5.6}$$

$$d_z\rho C_p u\cdot\nabla T+\nabla\cdot q=d_zQ+q_0+d_zQ_p+d_zQ_{vd} \tag{5.7}$$

$$q=-d_zk\nabla T \tag{5.8}$$

Ignoring viscous dissipation and pressure work put the general heat equation into Equation (5.9), where the ρ is density, C_p is the specific heat capacity, *T* is the absolute temperature, *u* is the velocity vector, Q contains heat sources other than viscous dissipation. The heat transfer interface use Fourier's law of heat conduction, which states the conductive heat flux, q, is proportional to the temperature gradient, as shown in Equation (5.10).

The heat transfer model applied in this study specifies the properties of a phase change material according to the apparent heat capacity formulation. Instead of adding a latent heat L in the energy balance equation when the material reaches its phase change temperature T_{pc}, it is assumed that the transformation occurs in a temperature interval, $T_{pc}-\Delta T/2$ and $T_{pc}+\Delta T/2$. In this interval, the material phase is modeled by a smoothed function θ, representing the fraction of phase before transition, which is equal to 1 before $T_{pc}-\Delta T/2$ and to 0 after $T_{pc}+\Delta T/2$. The density, ρ, and the specific enthalpy, *H*, are expressed by Equation (5.11), where the phase 1 and phase 2 indicate a material in phase 1 or in phase 2, respectively. Differentiating with respect to temperature, this equality provides the following formula for the specific heat capacity, as shown in Equation (5.12). The mass fraction, α_m, is defined from

ρ_{phase1} , ρ_{phase2}, and θ according to Equation (5.14). It is equal to -1/2 before transformation and 1/2 after transformation. The apparent heat capacity, C_p, used in the heat equation, is given by Equation (5.12). The effective thermal conductivity reduces to Equation (5.13). Natural convection was not considered at this stage, which meant it was assumed there was only heat conduction in the liquid PCM, instead of convection and conduction.

$$\rho C_p \frac{\partial T}{\partial t} + \rho C_p \vec{u} \cdot \nabla T = \nabla \cdot (k \nabla T) + Q \tag{5.9}$$

$$q = -d_z k \nabla T \tag{5.10}$$

$$\rho = \theta \rho_{phase1} + (1-\theta)\rho_{phase2} \tag{5.11}$$

$$C_p = \frac{1}{\rho}(\theta \rho_{phase1} C_{p,phase1} + (1-\theta)\rho_{phase2} C_{p,phase2}) + L\frac{\partial \alpha_m}{\partial T} \tag{5.12}$$

$$k = \theta k_{phase1} + (1-\theta) k_{phase2} \tag{5.13}$$

$$\alpha_m = \frac{1}{2}\frac{(1-\theta)\rho_{phase2} - \theta \rho_{phase1}}{\theta \rho_{phase1} + (1-\theta)\rho_{phase2}} \tag{5.14}$$

The model assumes that mass is always conserved, which means that the density and the velocity must be related through Equation (5.15).

$$\frac{\partial \rho}{\partial t} + \nabla \cdot (\rho \vec{v}) = 0 \tag{5.15}$$

The boundary conditions in this model are also shown in Figure 5.1, along with the geometry. The symmetry boundary condition was applied in the centerline of the duct. In the air flow region, air inlet velocity was set at 0.493 m/s and its inlet temperature was defined at 357.15 K, following one of the experiment working conditions. The upper wall was considered with well thermal insulation. A predefined outlet boundary condition was defined at the duct outlet.

For the whole region, a room temperature, which is 303.15 K (30 ℃), was set as the initial temperature condition.

Three materials were applied in this simulation: air, aluminum and the PCM, which was the paraffin wax. The thermal properties of air and aluminum were predefined in COMSOL. The thermal properties of paraffin wax were defined manually and the specific values are shown in Table 5.1 below.

Table 5.1: Thermal properties of paraffin wax defined

PCM	Paraffin wax
Density	775 kg/m^3
Conductivity	0.25 W/m ⋅K
Heat capacity at constant pressure	2384 J/kg ⋅K
Phase change temperature range	322.615-328.765 K
Latent heat	126.2 kJ/kg

5.2.2 Mesh Generation

Comparing to ICEM CFD, COMSOL has a simpler mesh generation strategy. The triangular mesh was applied in the air region and aluminum region. Boundary layers were employed on the interfaces between air and aluminum. To have a better melting front prediction, a dense quadrilateral mesh was generated in the PCM region. The total elements generated in this mesh were 30140, which included 18237 triangular elements and 11903 quadrilateral elements. The generated mesh for the whole domain is shown in Figure 5.2, and mesh details about the PCM and aluminum cases are presented in Figure 5.3.

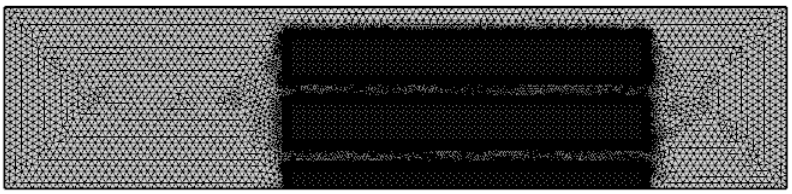

Figure 5.2: Mesh generated for the whole computational domain

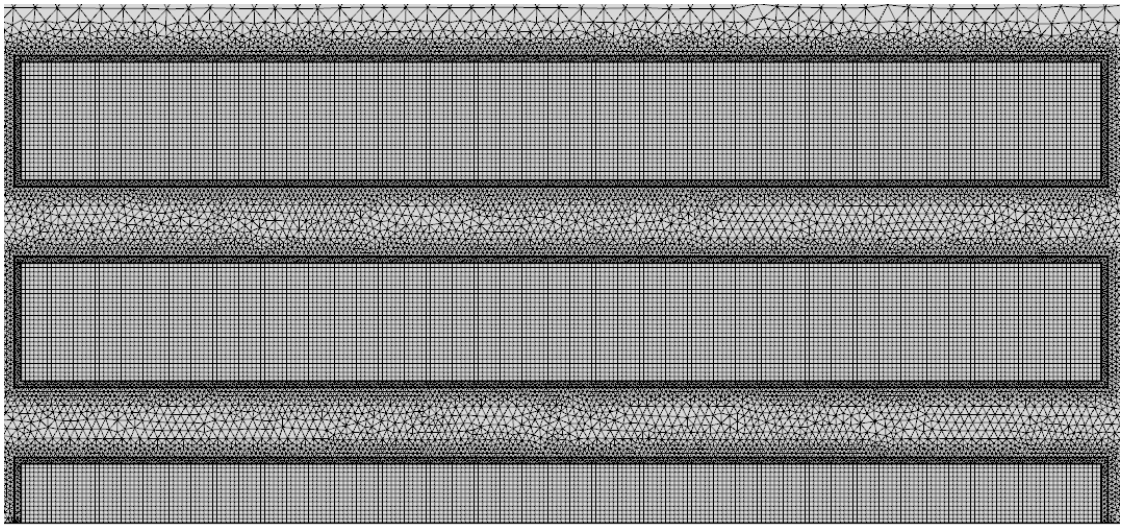

Figure 5.3: Mesh details about the PCM and Al case

5.2.3 Mesh Independent Study

Mesh independent study was carried out to investigate the effect of mesh elements. Four different meshes were generated and the numbers of mesh elements are 12094, 16663, 30140, and 56037 respectively. Under the same working condition of RPM 25, 2 kW, the four meshes were applied in the simulation. The corresponding results are compared, especially the outlet air average temperature and PCM temperature at location (200, 46). The results are shown in Figure 5.4 to Figure 5.6.

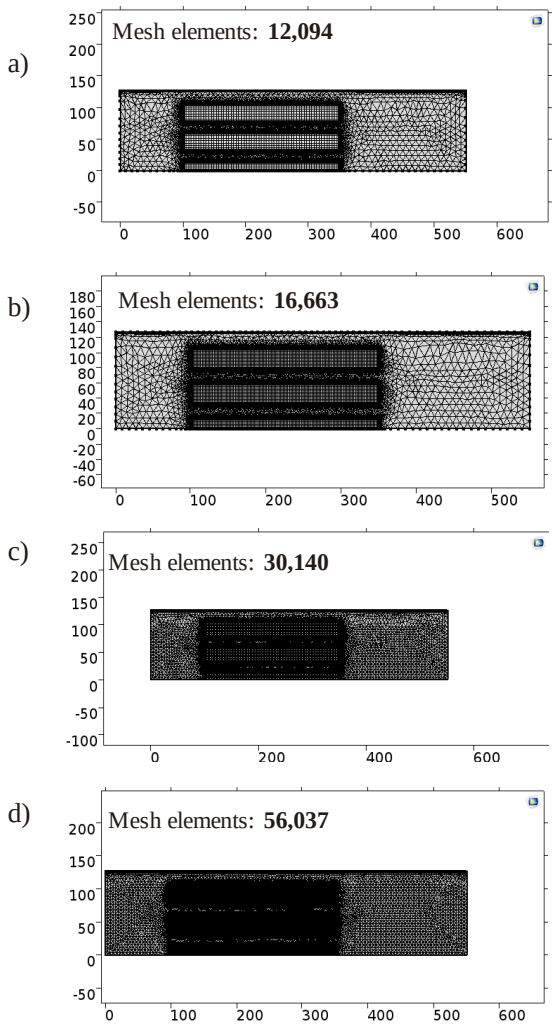

Figure 5.4: Meshes generated for grid independence study

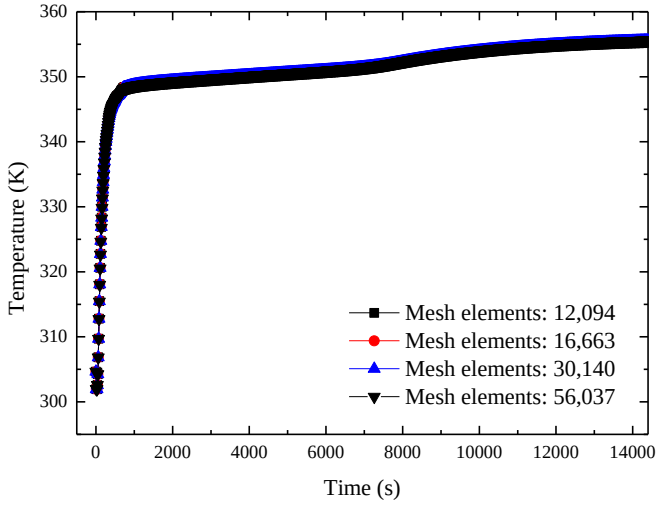

Figure 5.5: Air outlet temperature histories in cases with three different mesh elements

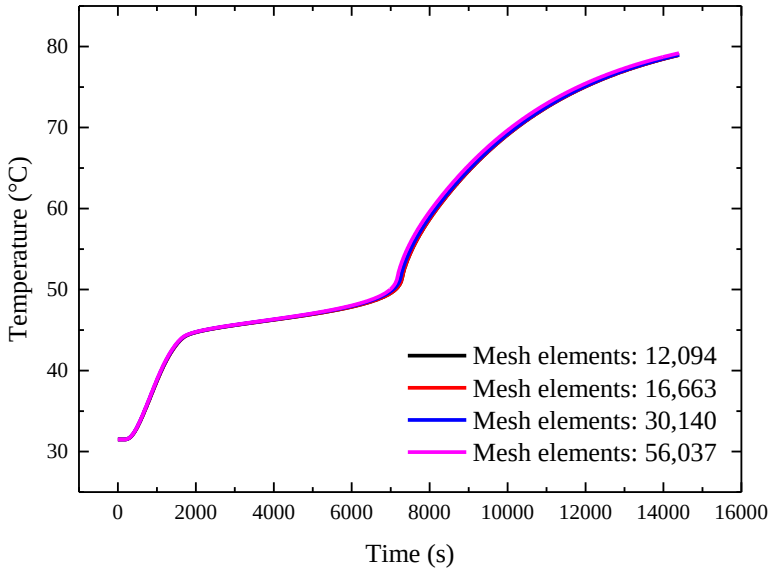

Figure 5.6: PCM temperature at position (200, 46)

5.2.4 Results and Discussion

A time-dependent study was carried out in this simulation and the simulated time period was 14400 s, following the experiments in Chapter 4. The solver setting was kept default for the simulation. Different from ANSYS Fluent, there is no need to provide an investigation point before the simulation running. In COMSOL, the temperature, velocity and pressure data for the whole domain are saved automatically after the simulation.

5.2.4.1 Velocity Contour and Stream Line Analysis

Figure 5.4 presents the steady air flow velocity contour and the streamline achieved from the simulation results. Although it is a time-dependent study, air flow becomes steady after a short period of simulation in the air region. It is because of the stable air flow inlet and fixed geometry. From the velocity contour, it can be found that the air flow velocity increases after flowing into the gaps between PCM, and decreases after leaving the gaps. In the initial segment of the air

flow in the PCM gaps, there exists a boundary layer developing region, which is the small blue region in Figure 5.4 near the inlet of the PCM gaps. While at the outlet, due to non-uniform air flow distribution and the sudden pressure increase, several vortexes exist and one larger vortex near the bottom symmetry line. Based on the analysis, several improvements were proposed for the consideration of future work. Firstly, a return guide vane can be added on the front side of the chamber, in order to smooth the sudden pressure drop in the inlet part causing by the crush of air and PCM chamber. Secondly, the whole PCM chamber geometry may be modified into a hydraulic form in order to make the air flow more uniform.

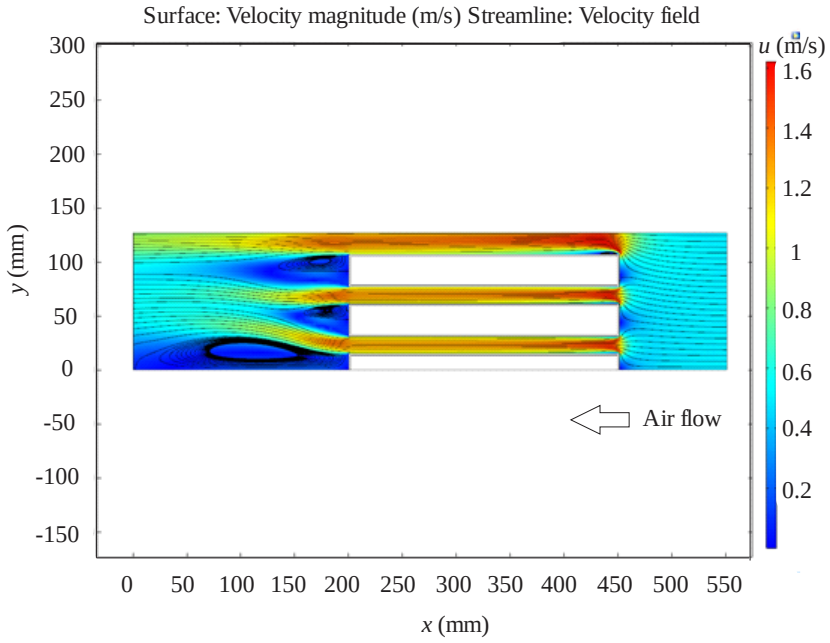

Figure 5.7: Velocity contour and streamline achieved from the simulation results

5.2.4.2 Temperature Contour Analysis

Figure 5.5 presents three temperature contours at 1000 s, 5000 s, 10000 s respectively. From the temperature contours, it is found that in the air region, the temperature becomes more uniform with time going on. This is because the temperature differences between aluminum cases, PCM,

and hot air are decreasing with time, and thus the heat transfer rate between air and PCM decreases. With the animation of the temperature contours, it can also be found that the heat transfer in the middle part of the PCM is slow than the heat transfer process in the boundary. This is easy to conclude; however, it has an important meaning for the design of PCM encapsulation geometry.

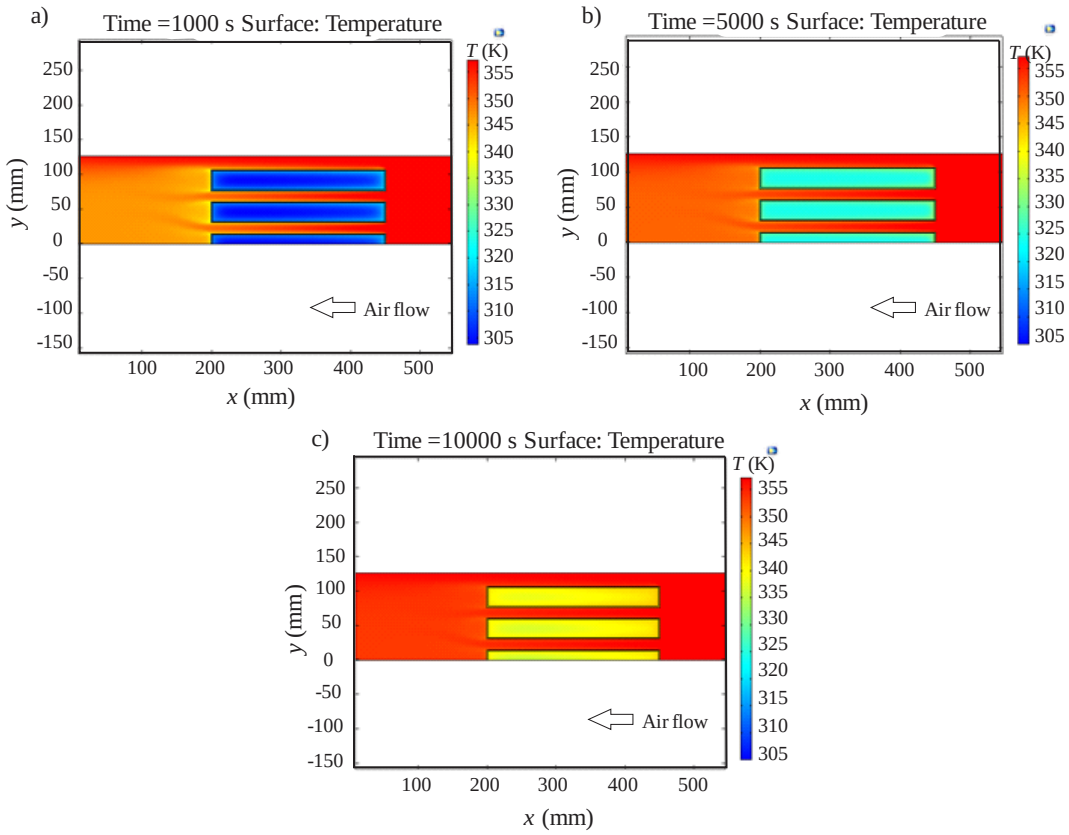

Figure 5.8: Temperature contours of the whole domain at 1000 s, 5000 s and 10000 s respectively

5.2.4.3 Phase Indicator Contour Analysis

Figure 5.6 presents the phase indicators of the PCM domain at 1000 s, 5000 s, 10000 s respectively. The three PCM chambers appear similar results at the three-time points. From the simulation, the PCM is under solid state at 1000 s, under phase transition at 5000 s, and under completely liquid state at 10000 s. An interesting finding is that the PCM melting front inside the

chamber is a “hydraulic form” shape. PCM melts faster at the front side near the air flow inlet than the back side near the air flow outlet. One of the possible reasons for this phenomenon may be because of the decreased heat transfer rate from the front side to the back side of the PCM chambers.

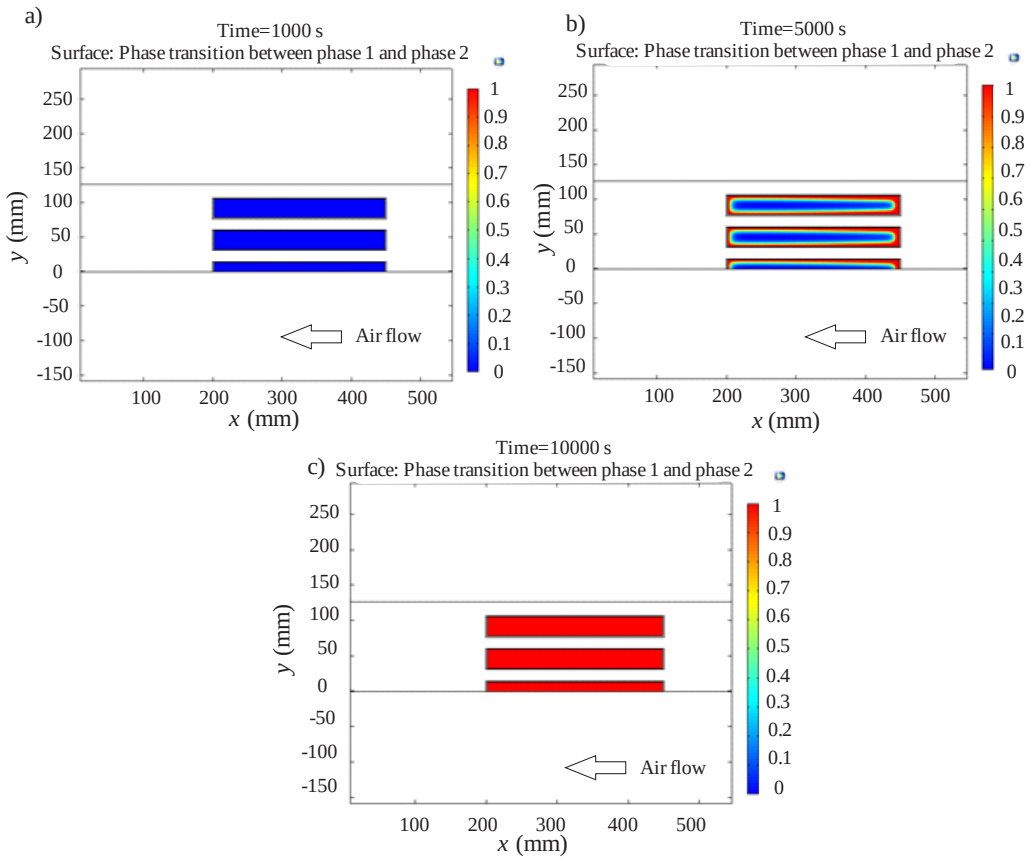

Figure 5.9: The Phase indicator contours of the PCM domain at 1000 s, 5000 s and 10000 s respectively

5.2.4.4 Validation of the Numerical Model

To verify the numerical model, the temperature data of the simulation with the experimental results at both a position inside PCM and the air outlet were compared. Figure 5.7 presents the simplified geometry diagram and the red spot in the chamber B is the position for comparison.

Under the coordinate systems in Figure 5.7, the location of the red spot is (283.7,46). Two temperature results inside PCM from the experiment are used for comparison. The comparison is shown in Figure 5.8. In Figure 5.8, Experiment Results 1 is the test point at the 2/3 Height of the aluminum case in Z-direction and Experiment Results 2 is the test point at the 1/3 Height of the aluminum case in Z-direction. The simulation and the experiment results agree relatively well with the trends. From Figure 5.8, PCM melts faster in the two experiment results. Also, the curve of the numerical simulation results is more stable than the experiment results. The "sudden jump" of temperature appeared at the end of melting process in both the experiment results nor in the simulation results.

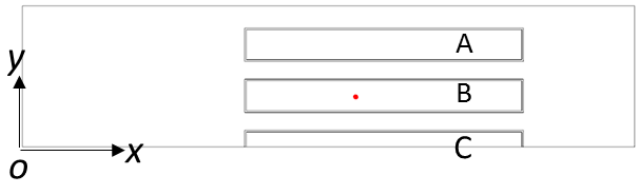

Figure 5.10: The simplified geometry diagram

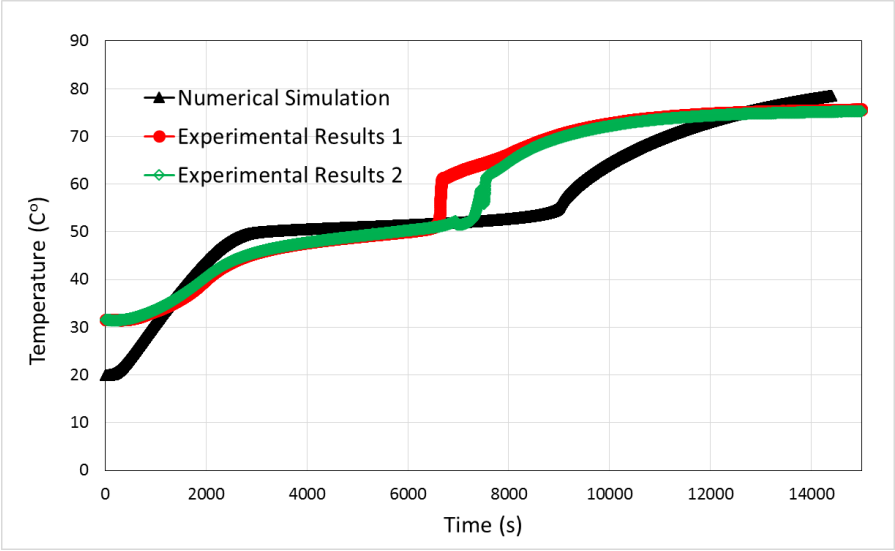

Figure 5.11: Simulation temperature profiles compared with experimental results inside PCM

Except for the temperatures inside PCM and the temperature difference between the inlet and outlet air, the calculated instantaneous heat transfer rate during the charging process is also compared. The comparison is shown in Figures 5.9 and Figure 5.10. In both Figures 5.9 and 5.10, a stable region appears, which is caused by the latent heat of the PCM. Comparing to the sensible heat storage sections in the start and at the end of the curve, the involvement of the latent heat during the PCM melting has increased the PCM's energy storage density, thus making the temperature difference become more stable during phase change period. This is the reason for the appearance of the stable region in Figures 5.9 and 5.10. Also, the stable region appeared in the experiment results curves, although with a less time. What's more, the temperature difference in the simulation is less than the experiment results, while the heat transfer rate curves agree well with each other.

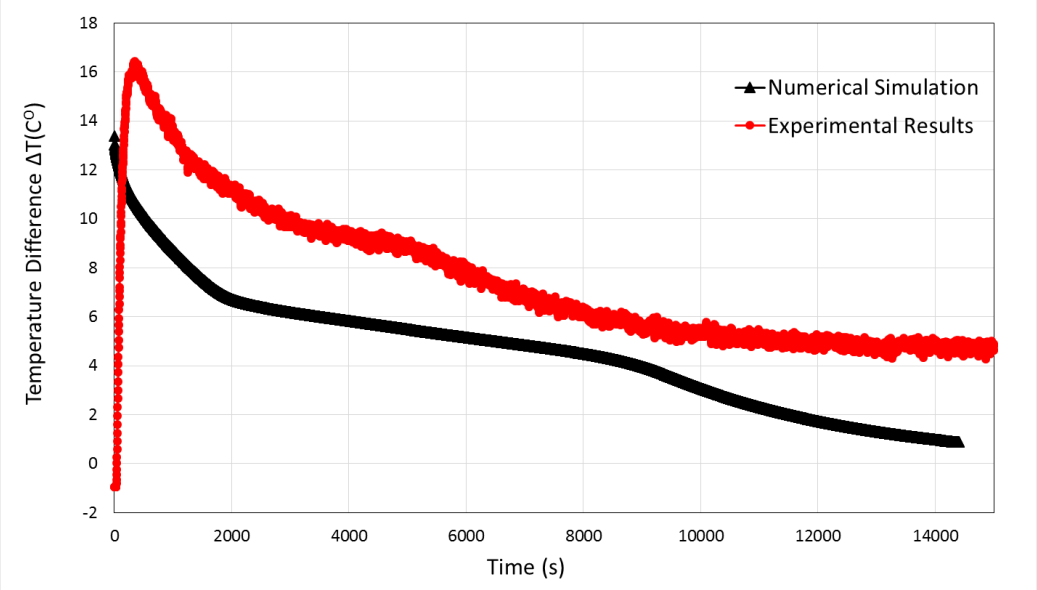

Figure 5.12: Temperature difference between inlet and outlet during charging process

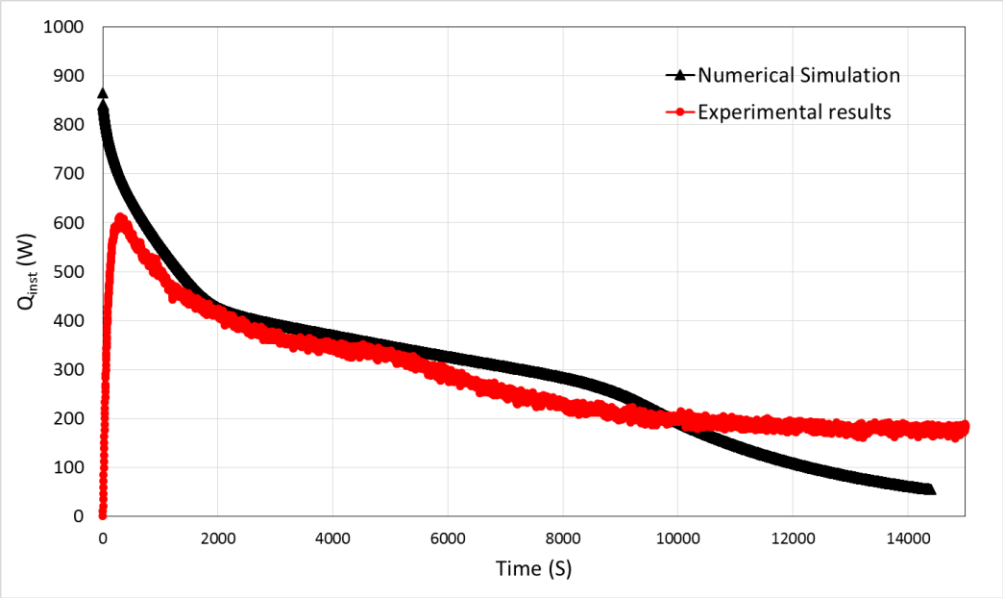

Figure 5.13: Instantaneous heat transfer rate during the charging process

In a short summary, the two-dimensional simulation relatively well predicted the thermal storage performance of the TES unit. Without the natural convection considered, the predicted phase change process is slower than the experiment results. Besides, the temperature "sudden jump" phenomenon also did not appear in the simulation results. The instantaneous heat transfer rates of the simulation results fit well with the experiment results. From which, this numerical model can be verified. However, to further investigate the effect of natural convection, a three-dimensional simulation with natural convection considered is needed.

5.3 Three-Dimensional Numerical Simulation

5.3.1 Geometry and Model Introduction

Based on the PCM chamber geometry in the experiment, an equivalent three-D PCM chamber was built in COMSOL. Considering the limited computational resources, only one

chamber was built instead of the whole TES unit. Figure 5.11 presents the geometry model of the partial duct and one PCM chamber with its aluminum case. Especially, the height of this geometry model is 250 mm along the z direction.

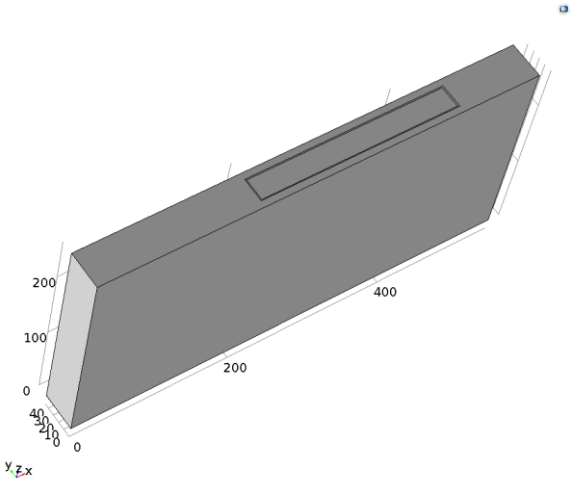

Figure 5.14: Geometry built for the three-dimensional numerical simulation

Same as the Two-D simulation, the materials involved in this Three-D simulation are still air, aluminum and the PCM, which is the paraffin wax. The thermal properties of paraffin wax applied have been shown in Table 5.2. The whole computational domain is thus divided into three regions: the air, the aluminum case and the PCM regions.

Different from the Two-D simulation model, natural convection, or body force was considered. A volume force was used to simulate the effects of density and gravity on the movement of the liquid PCM. The volume force was calculated as follows:

$$F = g\rho\alpha(T - T_0) \tag{5.16}$$

The thermal conductivity and density of PCM were assumed to be constant.

5.3.2 Mesh Generation

The number of elements in the mesh greatly affect the computational cost. To make the mesh have a more reasonable distribution, the mesh sweep strategy was adopted in the *z* direction. The generated mesh is presented in Figure 5.12. In the *x*-*y* plane of the geometry model, a free triangular elements generation strategy was applied. The total number of mesh elements is 147648.

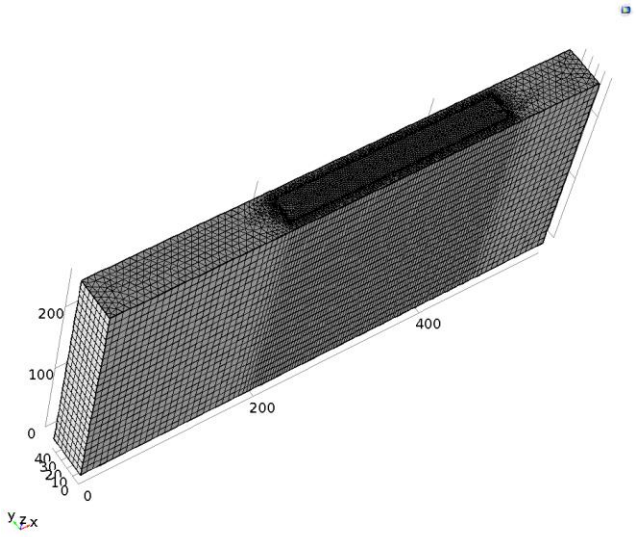

Figure 5.15: Mesh generated for the whole computational domain

Similar to the reasons stated before, this simulation adopted the maximum mesh that could be achieved right now and also ensure the iteration converging. A finer mesh would be hard to achieve considering the current computational ability. Thus to make sure of current simulation validity, the available denser mesh was applied in the important parts like the interfaces and boundaries.

5.3.3 Results and Discussion

A time-dependent study was carried out and the computational time was set to be 14400 s. Figure 5.13 presents the computational results of temperature and velocity field contours at 6000 s and 7200 s respectively. The two contours expressed that the PCM was under the melting process. It could be seen from the contours that the PCM at the start of the chamber along the flow direction melt first and the upper part of PCM melt faster than the lower part. This finding fits the existence of the natural convection, which enhances the heat transfer process inside the PCM during melting. Besides, generally, the PCM melt from parts near the chamber sidewalls to the center except the top sidewall and the bottom wall. Based on this, it can be found that in the heat transfer process of hot air to the PCM inside the chamber, the contact heat transfer from the metal wall to the PCM nearby and the convection heat transfer inside the liquid PCM is more efficient than heat conduction inside the solid PCM. This is also the reason why researchers are working on the PCM conductivity enhancement ways and how adding fins helps the heat transfer inside the PCM.

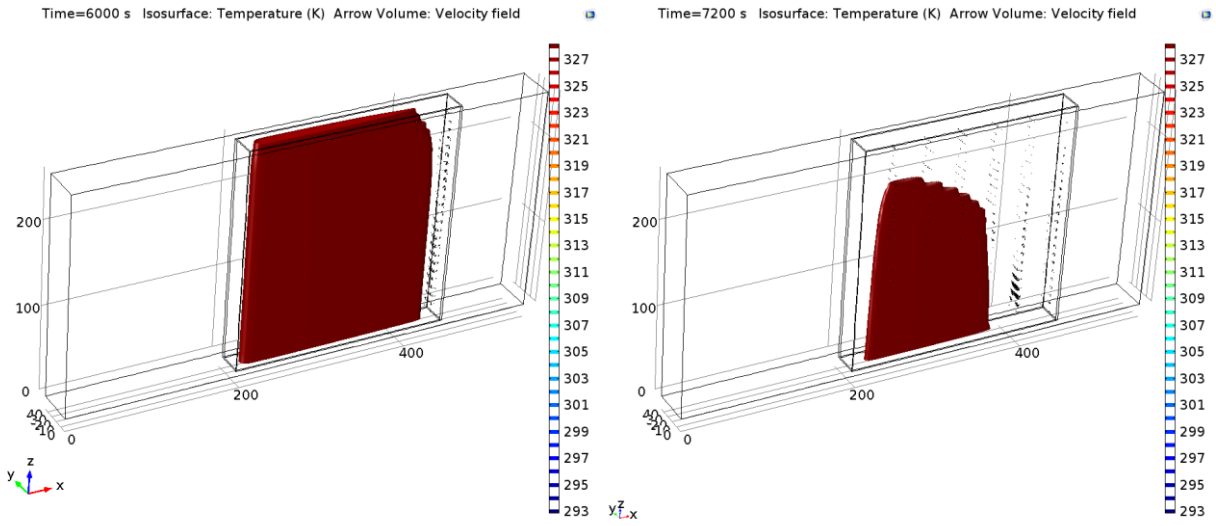

Figure 5.16: Temperature and velocity field contours at 6000 s and 7200 s respectively

It is interesting to see how the simulation results change after involving with natural convection at the same position. In the Two-D simulation part, the numerical simulation temperature profiles were compared with experiment results at the same position. The same comparison is made in Figure 5.14, where the temperatures profiles of two locations inside the PCM from both the Two-D and the Three-D simulations are compared with the experiment results. The two locations in the Three-D domain is (299.5, 23, 84) and (299.5, 23, 167). Most obviously, it was found that the "sudden jump" appeared in the Three-D simulation. With this evidence, it can be concluded that this "sudden jump" phenomenon is due to the existence of natural convection inside liquid the PCM. The assumption can be made that the temperature jump would happen under the low heat conduction inside the solid PCM and the strong liquid convection inside liquid PCM, thus there would exist a temperature gradient between the liquid PCM and the solid PCM near the melting front. Another similar trend that the Three-D simulation fit the experimental results is that the upper PCM would melt faster than the lower part. Although the experiment results have a relative higher melting rate, the temperature increasing trends agree well with each other. This comparison verifies the Three-D numerical model, also make the PCM system simulation more convincing.

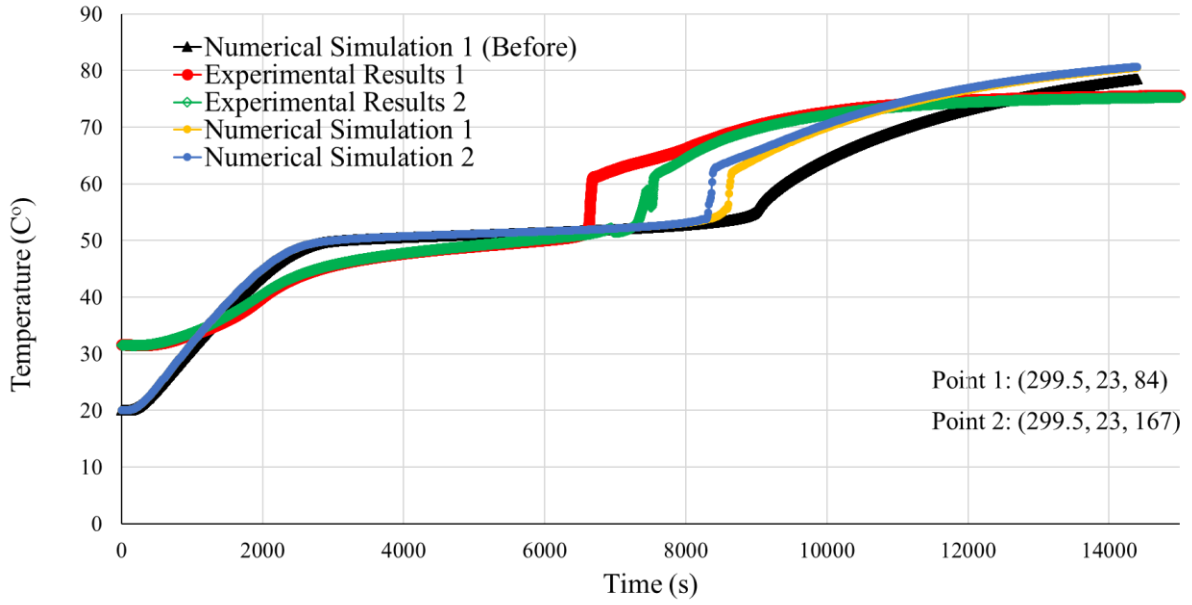

Figure 5.17: The Two-D and Three-D simulation temperature profiles compared with experimental results inside PCM

5.4 Summary

This chapter explores the Two-D and the Three-D numerical simulations of a PCM TES unit. Both of the simulation studies are time-dependent and coupling of fluid flow and heat transfer. The natural convection inside liquid PCM was considered in the Three-D numerical simulation. The numerical simulation results were compared with experimental results. It was found that with the natural convection considered, the temperature profiles of the PCM were more close to the experiment results. A special phenomenon, “sudden jump” of temperature at the end of PCM melting was successfully simulated. The numerical models were verified through the comparison.

Chapter 6: Design of A Final Thermal Energy Storage System

6.1 Introduction

Current the TES system in the congregation cycle requires a heat exchanger that can charge and discharge heat from the PCM at the same time. To fulfill this requirement, a prototype of the heat exchanger was proposed. Figure 6.1 shows the schematic of this design. In this design, the selected PCM is stored in the shell side. Hot exhaust air will go through the channel part between each gap of two aluminum cases, and the pin and fins in airside will enhance the heat transfer from the exhaust air to the PCM. As to the discharge cycle, the heat transfer fluid will flow through the tubes, and extract heat from the PCM to heat up the working gas of the Stirling engine.

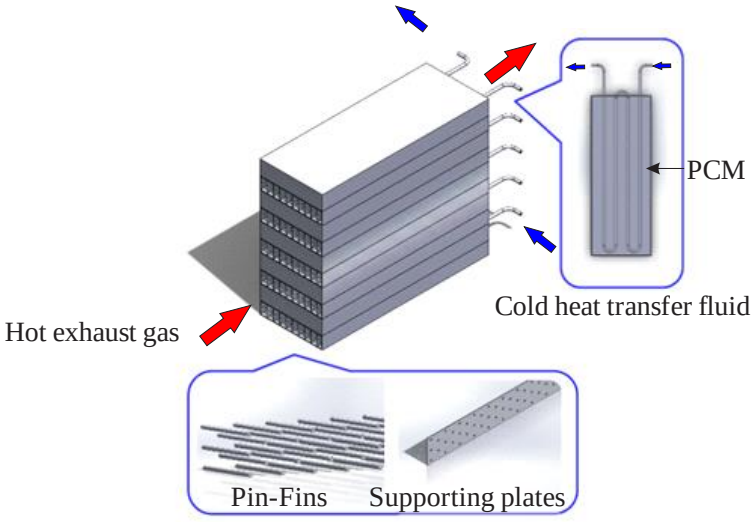

Figure 6.1: The heat exchanger design for thermal storage system

To realize the energy converting function in the cogeneration cycle, the latent heat TES system should include three parts: the duct for the hot exhaust gas, the tubes for the cold heat

transfer oil and the chambers for the PCM. A proper design for combing the three parts together shall meet the requirements as follow:

1) Easy to manufacture;
2) Enough heat transfer rate for the system;
3) Enough high heat transfer oil outlet temperature;
4) Short charging time for PCMs to melt;
5) Enough large TES capacity;
6) PCMs are in phase change temperature range during system steady working condition;

The design of the latent heat storage system above is based on the design of the small TES unit in Chapter 4. A tube for oil is embedded into the PCM chamber to discharge the thermal energy stored in the PCMs. As a preliminary step, a theoretical model is built for the steady working condition. Various parameters, including the inlet temperature and the mass flow rate of the exhaust gas, the inlet temperature and the mass flow rate of the heat transfer oil, and the geometric parameters like the PCM chamber thickness, the oil tube diameter are evaluated based on the model. The model output is compared with the design requirements. A group of proper parameters is selected and the design is numerically evaluated through verified model in Chapter 5.

6.2 System Theoretical Model and Parameters Study

In order to simplify the heat transfer process, the latent heat storage system is treated as a one-dimensional model. During the steady working condition of the thermal energy storage system, there exists a balance between the charging process and the discharging process. The

simplified heat transfer process is shown in Figure 6.2. The steady state working condition can be described by the following group of equations:

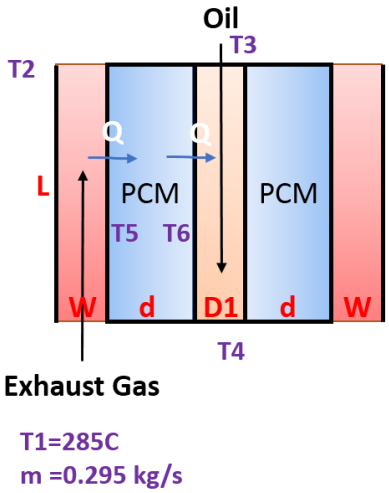

Figure 6.2: One-dimensional heat transfer process in the latent heat thermal storage system

$$\dot{Q} = C_{p,gas}\dot{m}_{gas}(T_{gas,in} - T_{gas,out}) \tag{6.1}$$

$$\dot{Q} = h_{gas}A_{gas}(\frac{T_{gas,in} + T_{gas,out}}{2} - T_5) \tag{6.2}$$

$$\dot{Q} = k_{PCM}A_{gas}\frac{T_5 - T_6}{d_{PCM}} \tag{6.3}$$

$$\dot{Q} = C_{p,oil}\dot{m}_{oil}(T_{oil,out} - T_{oil,in}) \tag{6.4}$$

$$\dot{Q} = h_{oil}A_{oil}(T_6 - \frac{T_{oil,in} + T_{oil,out}}{2}) \tag{6.5}$$

The solution is as following:

$$T_{gas,out} = \frac{T_{gas,in}\left(\frac{2C_{p,gas}\dot{m}_{gas}}{h_{oil}A_{oil}} + \frac{C_{p,gas}\dot{m}_{gas}}{C_{p,oil}\dot{m}_{oil}} + \frac{C_{p,gas}\dot{m}_{gas}}{h_{gas}A_{gas}} + \frac{C_{p,gas}\dot{m}_{gas}d_{PCM}}{kA_{gas}} - \frac{1}{2}\right) + T_{oil,in}}{\frac{2C_{p,gas}\dot{m}_{gas}}{h_{oil}A_{oil}} + \frac{C_{p,gas}\dot{m}_{gas}}{C_{p,oil}\dot{m}_{oil}} + \frac{C_{p,gas}\dot{m}_{gas}}{h_{gas}A_{gas}} + \frac{C_{p,gas}\dot{m}_{gas}d_{PCM}}{kA_{gas}} + \frac{1}{2}} \tag{6.6}$$

$$T_5 = \frac{T_{gas,in} + T_{gas,out}}{2} - \frac{C_{p,gas}\dot{m}_{gas}(T_{gas,in} - T_{gas,out})}{h_{gas}A_{gas}} \tag{6.7}$$

$$T_6 = \frac{C_{p,gas}\dot{m}_{gas}d_{PCM}}{kA_{gas}}(T_{gas,in} - T_{gas,out}) + T_5 \tag{6.8}$$

$$T_{oil,out} = T_{oil,in} + 2\frac{C_{p,gas}\dot{m}_{gas}}{C_{p,oil}\dot{m}_{oil}}(T_{gas,in} - T_{gas,out}) \tag{6.9}$$

$$\dot{Q}_{perchamber} = 2C_{p,gas}\dot{m}_{gas}(T_{gas,in} - T_{gas,out}) \tag{6.10}$$

$$\dot{Q}_{TES} = N\dot{Q}_{perchamber} \tag{6.11}$$

where *N* is the number of the PCM chambers in the thermal energy storage unit, $\dot{Q}_{TES}$ is the total net heat transfer rate from the exhaust gas to the heat transfer oil.

A group of baseline parameters is given to calculate the solutions, as shown in Table 6.1. The corresponding working conditions are summarized in Table 6.2. It is reasonable to assume the exhaust gas as air, based on the gas component analysis. The thermal properties of the exhaust gas, the PCM (solar salt used in this calculation), and the heat transfer oil (XCKTHERM K1 used in this calculation) are listed in Table 6.3.

Table 6.1: Baseline geometric parameters for the TES system

Gas side		PCM side		Oil side	
Channel height	0.6 m	Chamber number	8	Tube outer diameter	0.008 m
Channel width	0.02 m	Chamber height	0.6 m	Tube thickness	1 mm
Channel length	1.53 m	PCM width	0.015 m	Tube inner diameter	0.006 m
Height width ratio	30	Chamber length	0.015 m	Tube length	8 m

Table 6.2: Baseline working conditions for the TES system

Gas side		Oil side	
Mass flow rate	0.295 kg/s	Mass flow rate	0.25
Gas average velocity*	4.047 m/s	Mass flow rate per tube	0.03125
Inlet temperature	285 °C	Inlet temperature	227 °C

* The velocity means the average velocity of exhaust gas in each air channel.

With the baseline parameter, the results are presented in Table 6.4. The results shown in Table 6.4 mean that current baseline parameters fit the project requirements, where the net heat transfer rate needs to be larger than 8 kW, and the PCM melting temperature is between the gas side temperature and oil side temperature, which means that the melting front of PCM is in the middle position, and the latent heat can be involved while the fluctuation occurs on the exhaust gas inlet temperature. The parameters study is carried out in order to see their effects on the PCM boundary temperatures and the net heat transfer rate for the TES system.

Table 6.3: Thermal properties of exhaust gas, PCM, heat transfer oil

Thermal properties	Thermal conductivity (W/m K)	Heat capacity (J/kg K)	Density (kg/m^3)	Kinetic viscosity (m^2/s)	Prandtl's number	Dynamic viscosity (Pa s)
Exhaust gas (250 °C)	0.0421	1034	0.675	4.1×10^{-5}	0.68	2.779×10^{-5}
PCM (221 °C)	0.45	1481	1948	-	-	
Oil (210 °C)	0.11235	2134	904.3			3.685×10^{-4}

Table 6.4: Results with baseline parameters

Exhaust gas outlet temperature	PCM temperature gas side T_5	PCM temperature oil side T_6	Oil outlet temperature	Net heat transfer rate per chamber $\dot{Q}_{perchamber}$	Net heat transfer rate for TES system $\dot{Q}_{TES}$
269.25 °C	262.16 °C	242.78 °C	243 °C	1067.3 W	8538.42 W

Figure 6.3 shows the effects of the exhaust inlet temperature on the output temperatures and the net heat transfer rate of the TES system. The exhaust inlet temperature changes from 265 °C to 290 °C. The effect of exhaust gas mass flow rate is shown in Figure 6.4. While on the oil side, the inlet temperature and the mass flow rate of oil also have influences when they change, as shown in Figures 6.5 and 6.6. Comparing to the gas inlet temperature, the oil inlet temperature has a greater influence on the PCM boundary temperatures and the net heat transfer rate of the TES system. With the increasing of the oil inlet temperature, the output temperatures increase with the net heat transfer rate of the TES system decreasing. Since the PCM oil side temperature should be below the melting point, and to keep the net heat transfer rate of the TES system large than 8 kW, the suggested oil inlet temperature is below 240 °C.

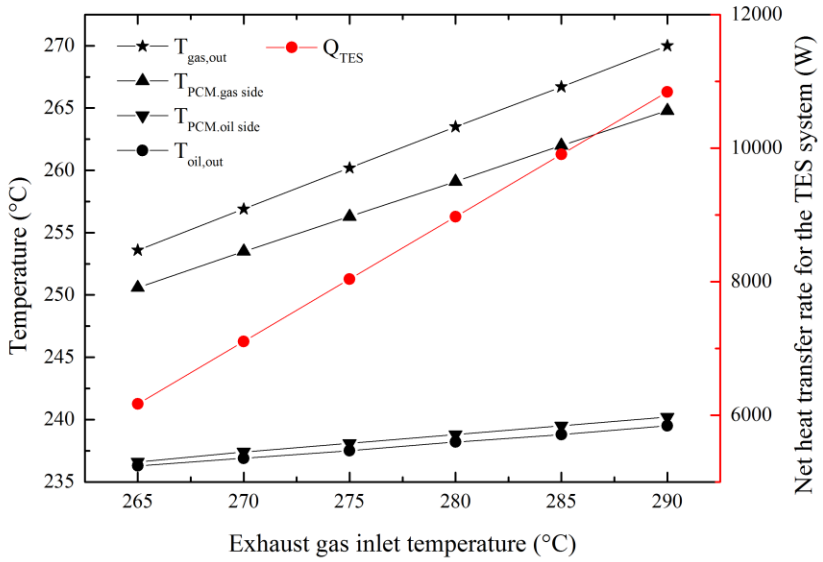

Figure 6.3: Effect of the exhaust gas inlet temperature on the output temperatures and the net heat transfer rate of the TES system

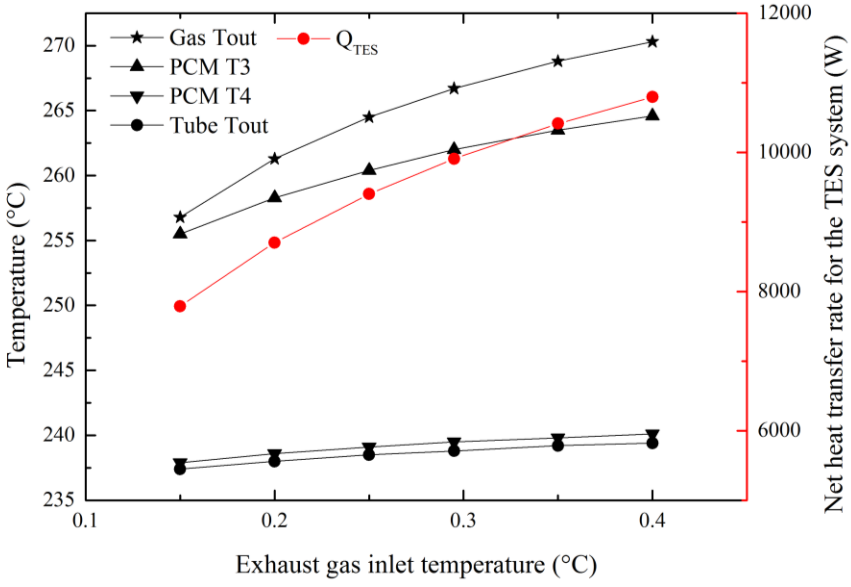

Figure 6.4: Effect of the exhaust gas mass flow rate on the output temperatures and the net heat transfer rate of the TES system

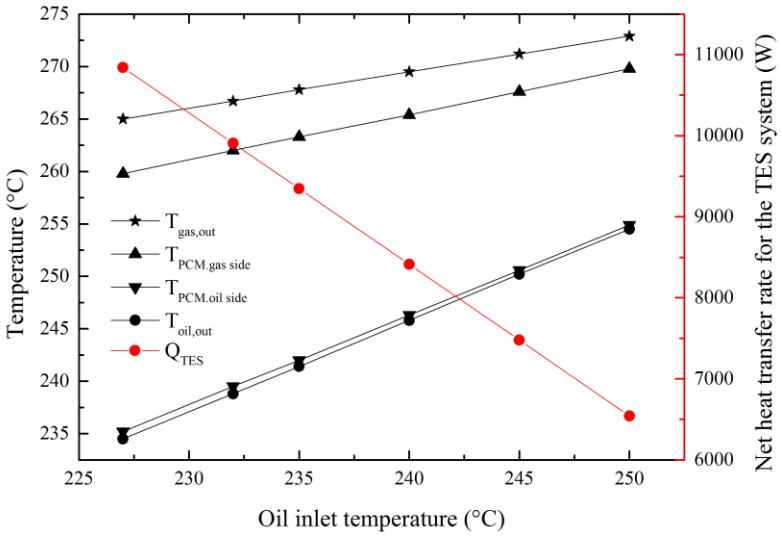

Figure 6.5: Effect of the oil inlet temperature on the output temperatures and the net heat transfer rate of the TES system

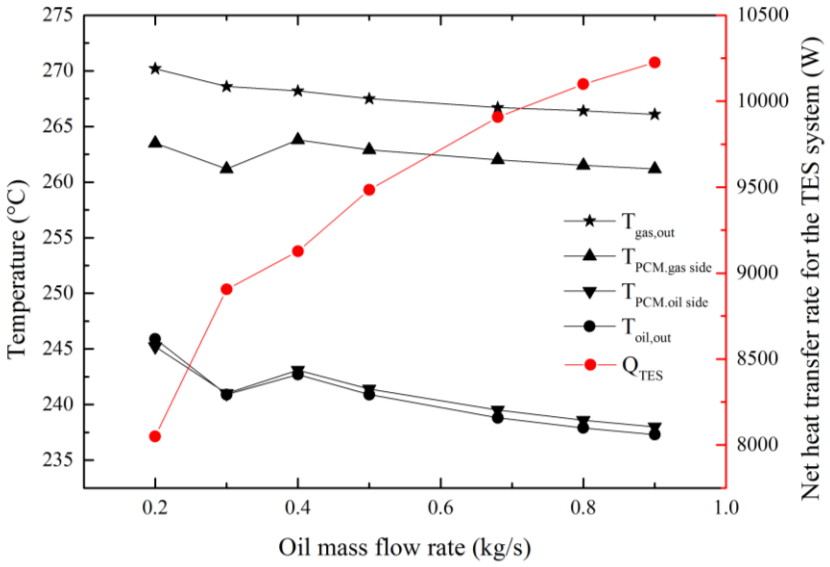

Figure 6.6: Effect of the oil mass flow rate on the output temperatures and the net heat transfer rate of the TES system

6.3 Numerical Simulation of the TES System

6.3.1 Geometry and Model Introduction

The geometry with selected parameters was built in COMSOL for the numerical investigation. Figure 6.7 presents its three parts: the oil tube, the PCM unit, and the exhaust gas channel. The design of the TES system applied the module design and only half of one module PCM unit was modeled in this simulation. In this way, the computational resources can be saved for running more cases under different working conditions. In the modeled geometry, the length of the gas duct is 2.5 m, and the length of the PCM unit is 1.5 m along the *x* direction in Figure 6.7. In the *z* direction, the height of gas channel and PCM unit is 0.6 m. Inside PCM, the length of the oil tube is 10 m long and its diameter is 2 cm.

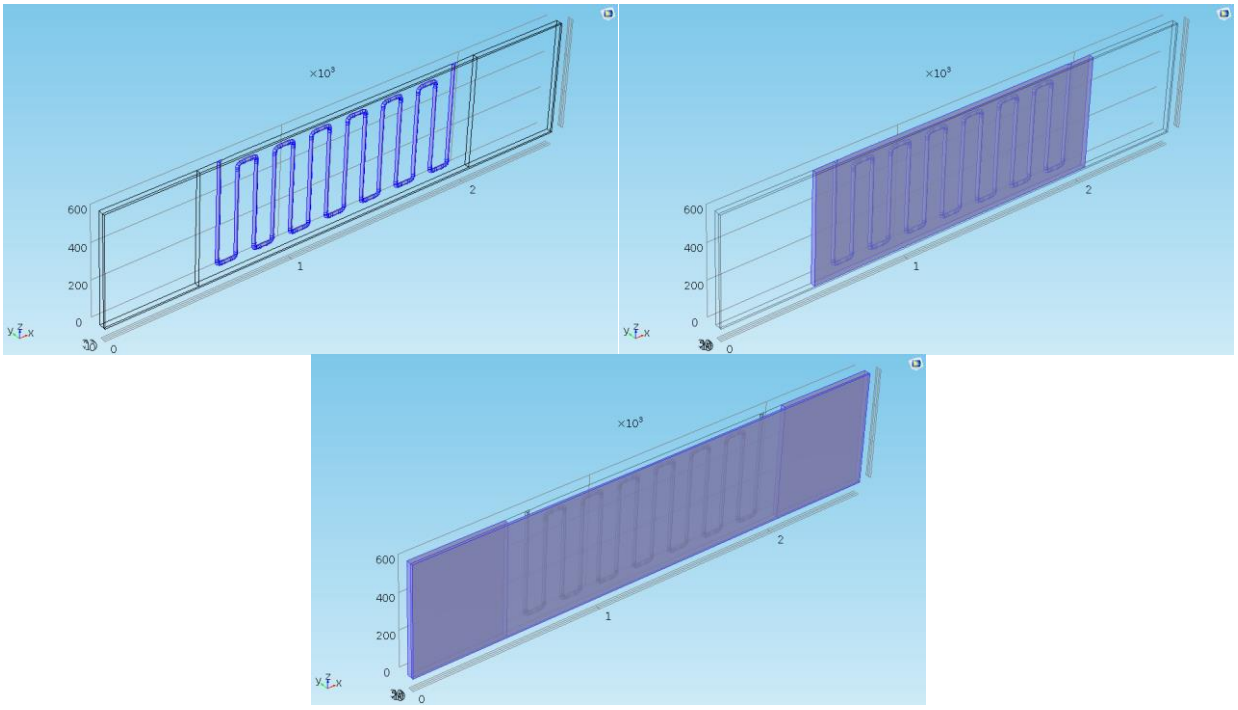

Figure 6.7: Geometry design of the TES system

The materials involved in the simulation include gas turbine exhaust gas, aluminum, and PCM, which is H250, a commercial product from PCMPRODUCT, UK. The thermal properties of this PCM are shown in Table as follows.

Table 6.5: Thermal properties of H250

Thermal properties	Melting point (℃)	Latent heat (kJ/kg)	Specific heat capacity (kJ/kg Ƙ)	Thermal conductivity (W/m Ƙ)	Density (kg/m^3)
Value	250	280	1.525	0.251	2380

The same numerical models were applied in this simulation as the Chapter 5. The momentum equation was solved for the gas region, and the continuity equation and energy equation were solved for the whole domain. The heat transfer model in COMSOL was used to simulate the phase change inside the PCM and the natural convection was not considered at this stage. The individual governing equations have been shown in Chapter 5.

The boundary conditions were set as shown in Figure 6.8. The hot exhaust gas inlet temperature was 558.15 K (285 ℃) and its mass flow rate was given by five different values, from 0.0214 kg/s to 0.035 kg/s. The inlet temperature of the oil was 499 K (225.85 ℃) and its mass flow rate was also given five values, ranging from 0.0068 kg/s to 0.020 kg/s. The symmetry boundary condition was both applied on the two sidewalls of the whole domain. The hot gas outlet temperature, the pressure drop, and the oil outlet temperature would be observed after the simulation, in order to evaluate the TES performance of this design.

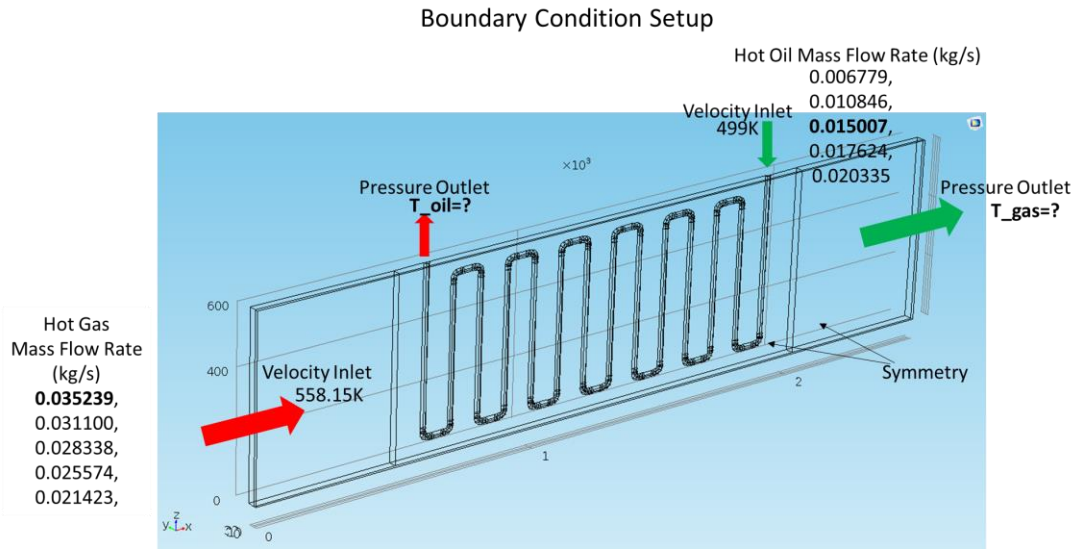

Figure 6.8: The boundary conditions set for the system simulation

6.3.2 Mesh Generation

Figure 6.9 presents the generated mesh. Due to the complexity of the geometry, a free generation tetrahedron mesh was applied. The denser mesh was adopted in the boundary layers of each two domain interfaces. Besides, the mesh was set to be denser nearby the tube wall. Comparing to the air domain, the mesh was denser in the PCM region, which would make the simulated melting front more clear and accurate. The final generated mesh included 1,117,839 tetrahedral elements, 143,369 triangular elements and 11,176 edge elements and 756 vertex elements. The average elements quality was 0.747, which was relatively higher than 0.5.

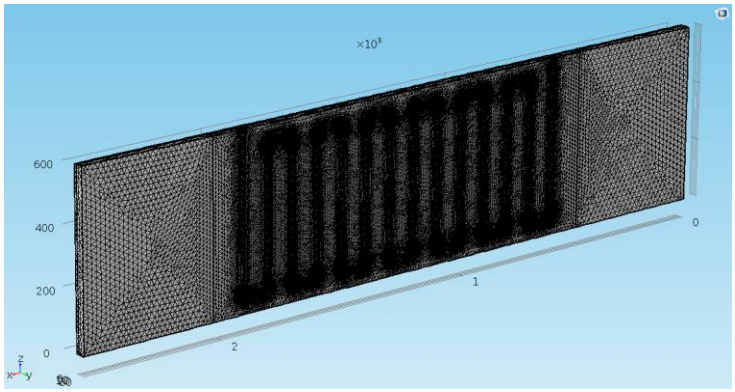

Figure 6.9: The mesh generated for the TES system simulation

6.3.3 Results and Discussion

Since the TES system has the heat input and the heat output and will always come to a steady working condition. It would be reasonable to use a steady state study to simulate its final working state. Two variables are investigated with different groups of parameters: the hot gas inlet mass flow rate and the oil inlet mass flow rate.

6.3.3.1 Effects of Hot Gas Inlet Mass Flow Rate

The hot gas inlet mass flow rate was changed while other input parameters were kept constant. Five cases were run in COMSOL using the same mesh mentioned above and the results were shown in Table 6.6. At the gas side, with the increasing of gas inlet mass flow rate, the gas outlet temperature increases, same as the pressure drop at the gas channel. The oil outlet temperature has also increased with a higher gas inlet mass flow rate, although the increasing is not as remarkable as the gas side. While the effect of hot gas inlet mass flow rate on the pressure drop at oil pipe is negligible. The pressure drop at the five working conditions is the same value as 140 Pa. The pressure drop at the gas channel in the five working conditions are satisfying as they are not more than 800 Pa, which is the limit of the gas turbine back pressure in the project.

Table 6.6: The effect of hot gas inlet mass flow rate on the output parameters

Gas Inlet mass flow rate (kg/s)	Gas Outlet Temperature (K)	Pressure Drop at Gas Channel (Pa)	Oil Outlet Temperature (K)	Pressure Drop at Oil Pipe (Pa)
0.0352	544.6	90	514.3	140
0.0311	543.1	70	514.1	140
0.0283	541.8	60	513.8	140
0.0256	540.3	45	513.6	140
0.0214	537.5	30	513.1	140

It is interesting to see how the gas inlet mass flow rate influences the PCM melting, which mainly decides the thermal storage performance. Figures 6.10 show the isothermal regions of 528-533 K, which is the melting range of PCM, at different gas inlet mass flow rates. The figures show the trend that the larger the gas inlet mass flow rate, the more PCM will be melted at the steady working condition. While it is also can be observed that the gas inlet mass flow rate mainly affects the PCM melt fraction near the oil inlet region.

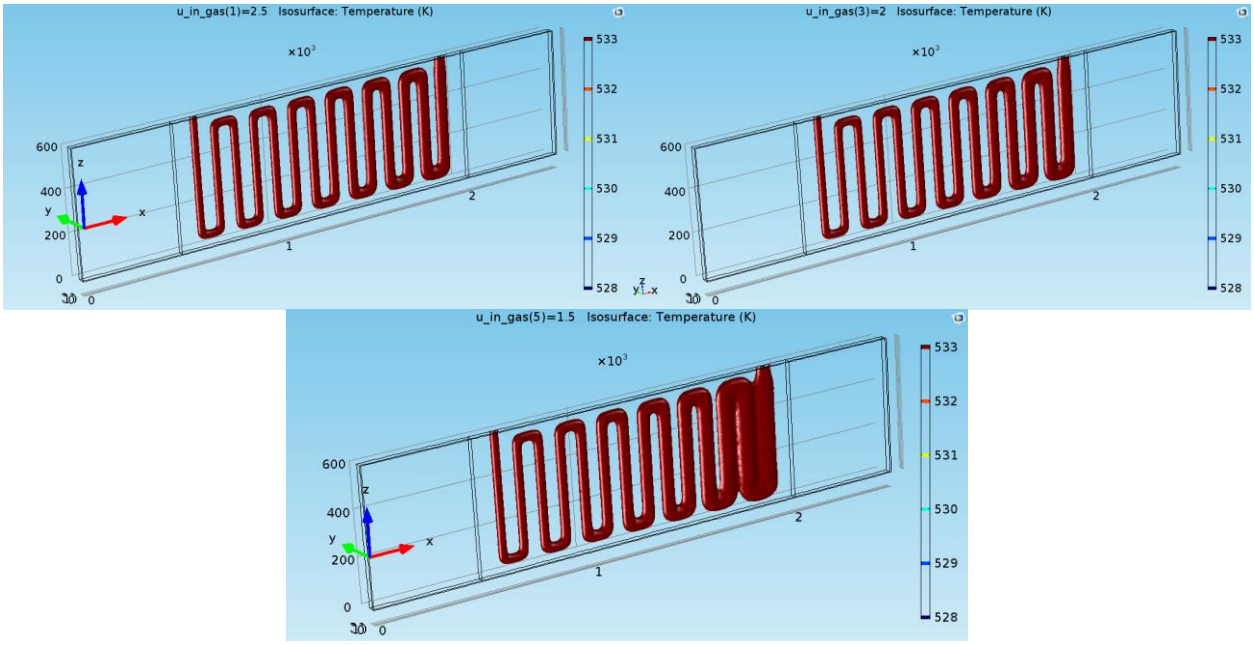

Figure 6.10: The effect of the gas inlet mass flow rate on the PCM isothermal regions

6.3.3.2 Effects of Oil Inlet Mass Flow Rate

Another five cases were run with the different oil inlet mass flow rates respectively. The oil inlet mass flow rate was changed from 0.0068 kg/s to 0.02034 kg/s in order to see its influence. The summary of the outputs is presented in Table 6.7. The increasing mass flow rate of oil absorbs more heat from the hot gas and makes the gas outlet temperature decreases. However, the pressure drop at the gas channel is not affected. The oil outlet temperature decreases from 527.92 K to 510.71 K and the pressure drop in oil pipe increases from 40 Pa to 250 Pa.

The effect of oil inlet mass flow rate on the PCM melting has also been investigated, as shown in Figure 6.11. The frozen or solid PCM, that is below the phase change temperature, is showed in the steady working conditions under three different oil inlet mass flow rates. It is shown that the oil inlet mass flow rate has a little effect on the PCM melting fraction. While the

little effect is observed near the oil outlet region. The larger the oil inlet mass flow rate is, the more PCM would be at frozen stage.

Table 6.7: The effect of hot oil inlet mass flow rate on the output parameters

Oil Inlet mass flow rate (kg/s)	Gas Outlet Temperature (K)	Pressure Drop at Gas Channel (Pa)	Oil Outlet Temperature (K)	Pressure Drop at Oil Pipe (Pa)
0.0068	546.6	90	527.9	40
0.0108	545.3	90	519.2	80
0.0150	544.6	90	514.3	140
0.0176	544.3	90	512.3	200
0.0203	544.1	90	510.7	250

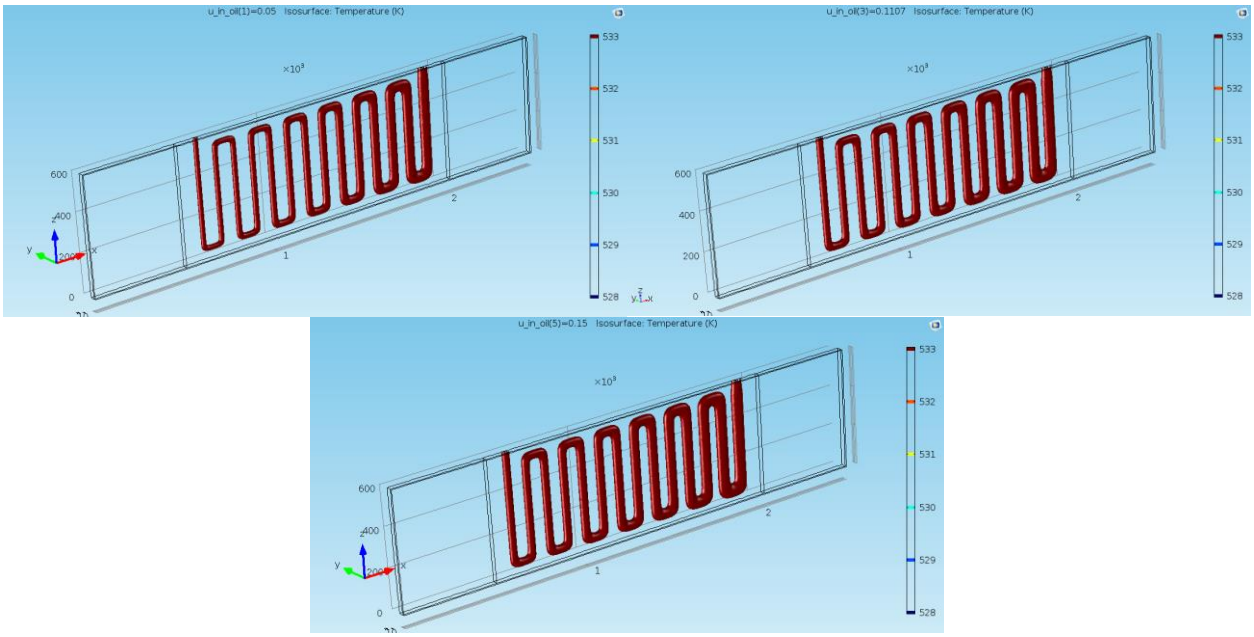

Figure 6.11: Effect of oil inlet mass flow rate on the PCM isothermal regions

Figures 6.12 and 6.13 present the temperature field of the gas domain and oil domain under the gas inlet mass flow rate of 0.035 kg/s respectively. It is found that the middle gas has a

significant temperature drop across the PCM chamber comparing with the exhaust gas near the top wall and the bottom wall. This is mainly because of the of the discharging oil flow in the middle region. Thus caused larger temperature gradient between the PCM and the gas makes the gas temperature drop more significantly. A similar phenomenon has been observed in Figures 6.14 and 6.15, where the oil inlet mass flow rate is 0.015 kg/s.

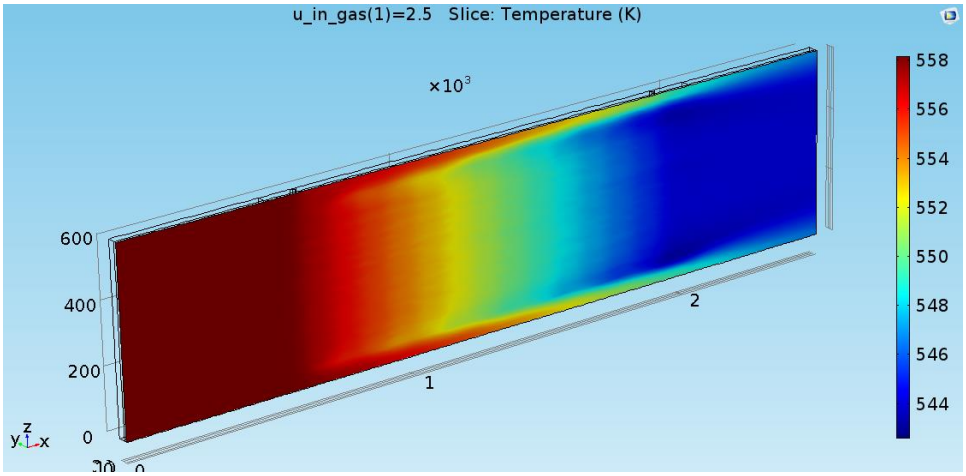

Figure 6.12: The temperature field of the gas domain under the gas inlet mass flow rate of 0.035 kg/s

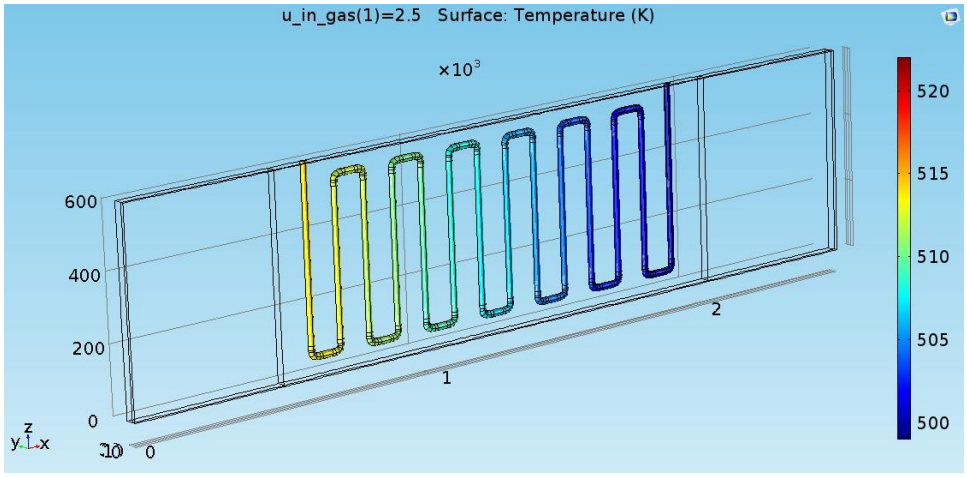

Figure 6.13: The temperature field of the oil domain under the gas inlet mass flow rate of 0.035 kg/s

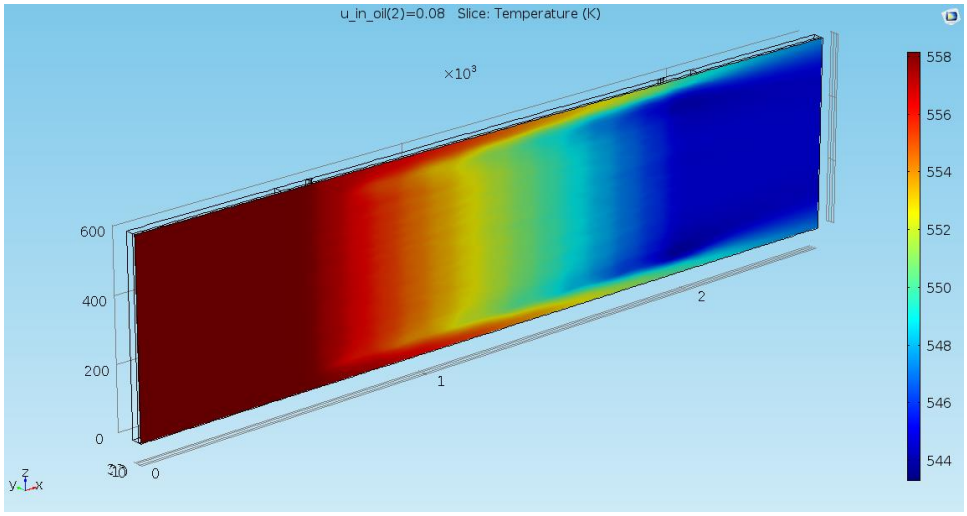

Figure 6.14: The temperature field of the gas domain under the oil inlet mass flow rate of 0.015 kg/s

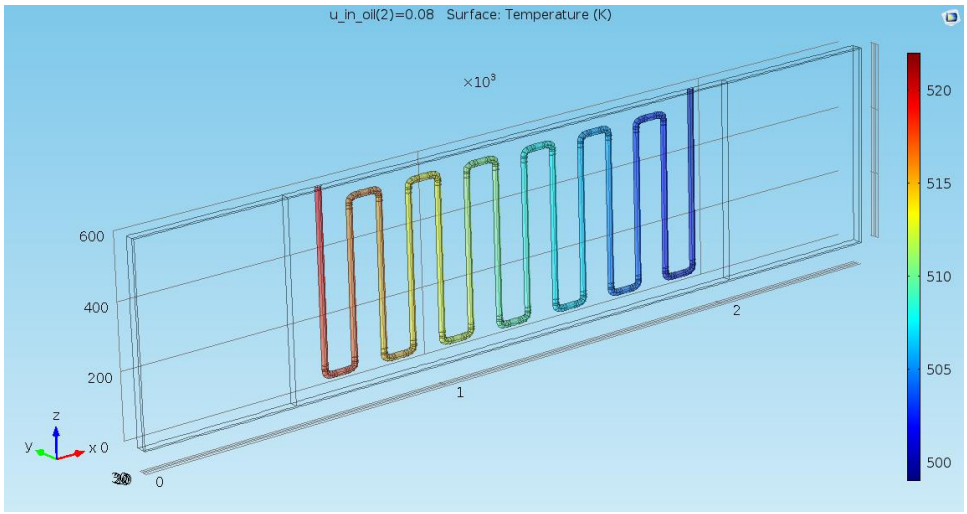

Figure 6.15: The temperature field of the oil domain under the oil inlet mass flow rate of 0.015 kg/s

6.4 Summary

In this chapter, a TES unit final design concept that can charge and discharge simultaneously was given. A one-dimensional simplified model was applied to carry out a parameter study. After that, based on COMSOL Multiphysics, one design with selected parameters was built and numerically simulated. The effects of two parameters, mass flow rates of hot gas and oil were

evaluated. The PCM melt fraction in the different steady working conditions was also discussed. Current related design results are satisfying, and furthermore, the time-dependent study related to the charging and discharging speed of the TES unit and also the effect of the natural convection on the TES system need to be carried out in the future.

Chapter 7: Conclusions and Future Work

7.1 Concluding Remarks

This thesis presents the current studies related to the development of a TES unit with PCMs in the gas turbine and the Stirling engine power cogeneration cycle. Mainly four different aspects are involved, including the thermal analysis of PCMs, the thermal storage experiment of a TES unit, the numerical simulation based on the storage experiment, and the thermal design of the finial TES unit with PCMs. The main conclusions for this thesis are summarized as follows:

1) The thermal analysis of various PCMs shows that salt and eutectic salt are better solutions for the high-temperature energy storage application. With different ratios of salts mixed, the eutectic salts can have a relatively low melting point that fit the middle high-temperature range. While the comparison of two thermal analysis methods, the DSC, and the T-history method, shows that their measurement results difference in melting point and latent heat. While in the T-history method, it was found that the smaller radius test tube and the preciser measurement of the natural convection coefficient, are two keys to achieving better and more accurate measurement results.

2) In the thermal storage experiment of the designed TES unit, its performance under various working conditions was investigated. At the lower fan speed and the higher heater power working conditions, the PCMs melt faster. While based on the results, the effect of heater power was more significant compared to the effect of fan speed. The comparison experiment was carried out with water, air and paraffin wax, and the test results show that paraffin wax, which is

the PCM in the experiment, managed to store the most energy per unit time during charging compared to sensible materials like water and air.

3) The Two-D and Three-D numerical simulation results were carried out with a time dependent solver in COMSOL Multiphysics. Both the two numerical simulation results fit well with the experiment results. However, with natural convection considered, the Three-D temperature profiles of the PCM were more close to the experiment ones. What's more, a special phenomenon, "sudden jump" at the end of the PCM melting was also only found in the Three-D simulation results, which proved that the importance of natural convection.

4) The system design study gave a final TES unit design concept that can charge and discharge simultaneously. A simplified one-dimensional theoretical parameter study was carried out. After that, one design with selected parameters was built and numerically investigated. The two inlet mass flow rate of gas and oil were changed to see their influence on the PCM melting and the TES performance. It was found that the gas inlet mass flow rate has a relative higher influence on the TES performance, while the influence of the oil mass flow rate was negligible. Also, the higher the inlet mass flow rate of gas was, the more PCM would be melt in the steady working conditions. This numerical simulation showed that the main thermal resistance existed between the gas side and the PCM.

7.2 Recommendations for Future Studies

The TES with PCMs has received extensive studies in the past decades, but the research on this topic is far from completed because of the associated complexity. Some recommendations for the future studies are listed as follows.

Regards the thermal analysis methods for PCMs, the following topics may be considered for further studies.

(1) Improvement of the T-history method: To improve the current T-history experiment design, a test chamber can be constructed to simulate the real working conditions in the industrial applications. With a test chamber, the environmental conditions could be controlled and adjusted in order to supply a more accurate and genuine representation of the actual applications. In addition, the PCMs in blocks can also be fitted into the test chamber to simulate the process of charging and discharging. The amount of energy charged or discharged should also be determined by the experimental method rather than the theoretical calculations.

(2) Application of T-history method on the middle high-temperature PCMs: From the literature review, a simple and easy experimental setup for the middle high-temperature PCMs has not been proposed. The traditional method used the water as the heating source and the experiment in this thesis used the heating block as a heating source as an improvement. An oil heating bath maybe another optional choice. A series of experiments can be done regards the effect of the tube radius, the effect of the cooling temperature and the effect of the heating method for a middle high-temperature PCM like $LiNO_3$.

(3) Literature summary for the T-history method new developments: The most recent literature review regards the T-history method is in 2013 [48]. As the T-history method was applied widely recent years, a new literature review including the recent ten years' development of the T-history method is worthwhile to be done.

Regards the TES unit design and the related experimental investigation, the following topics are worth to be explored.

(1) The effective design methodology of the TES unit: The design methodology of the TES unit in the thesis is based on a series steps, from the material characterization, the test unit experiment study, the numerical simulation with experimental validation process, to the system simulation and the corresponding parameter study. In the future study, an experimental correlation is worthwhile to be developed based on the various experiment data. In this way, it is possible to predict the TES system performance and contribute to the TES unit design field.

(2) Effective design of the PCM chambers: The PCMs are encapsulated in the aluminum chamber with plane aluminum walls. The experiments and simulations have shown that the main thermal resistance existed between the gas and the PCM. Thus it is worthwhile to experimentally and numerically investigate the effects of the following improvements on the aluminum chambers, such as adding fins on the chamber sidewalls, changing the roughness of the chamber sidewalls, changing the shapes of the chamber sidewalls.

(3) An experimental test of the TES unit with the Nano metal particle embedded PCMs: PCMs embedded with the Nano metal particles or metal foam have been proved to enhance the thermal conductivity [1]. However, not so much work has been done on the thermal storage performance test of the TES unit with the Nano metal particles or metal foam enhanced $LiNO_3$. Thus it can be considered to research on the effect of percentage of Nanoparticles and metal foam volume fraction on the PCM melting rate.

(4) An experimental test of the TES unit under simultaneously charging and discharging: Besides, current experiment is only for the charging test. In the next work, more experiments as to charging and discharging at the same time should be investigated. What's more, the heat

transfer inside the PCM during the phase change should also be investigated. The experimental data is helpful to validate the accuracy of the current phase change model.

Regards the simulation study related to the TES with PCMs, the listed topics are possible considerations.

(1) The system simulation of TES with PCMs: The system simulation in Chapter 6 is still not very complete and the storage rate needs to be further calculated from the simulation in the future. What's more, a transient study is needed to see how much time it would cost to reach the steady working condition. Besides, the following aspects may also be numerically investigated in order to further justify and improve the performance of the TES unit: the effect of time gap between the charging mode on and the discharging mode on, the effect of temperature and the mass flow rate damping at the gas inlet.

(2) Effect of the operating parameters: Since the numerical model has been validated by the experiment in Chapter 4, the effect of the operating parameters, like the gas inlet temperature, the oil inlet temperature can be done in the future numerical study. Currently in Chapter 6, only two parameters were studied, which were the gas inlet mass flow rate and the oil inlet mass flow rate.

(3) Effect of the TES unit geometrical parameters: It is of great meaning to optimize the performance of the TES unit through changing the geometrical parameters such as the gas channel thickness and the oil tube diameter under the allowable pressure drop limit. With the corresponding numerical study, the geometrical parameters of the TES unit could be optimized.

(4) Effect of the PCMs thermal conductivity enhancements: The thermal conductivities of the PCMs are relatively low and thus the thermal conductivity enhancement is important. While one PCM chamber with the different fins embedded would reach different thermal performances.

It is interesting and meaningful to numerically investigate the effect of different fins on the PCM melting rate for the further fin selection.

List of Reference

[1] İ. Dinçer and M. A. Rosen, *Thermal Energy Storage*. Chichester, UK: John Wiley & Sons, Ltd, 2010.

[2] "Efficient Use of Fossil Fuels." [Online]. Available: https://www.mhi-global.com/discover/earth/issue/history/future/efficiency.html.

[3] K. Wang, S. Dubey, F. H. Choo, and F. Duan, "Stirling engine for recovering LNG cold energy and exhaust heat," in *26th International Cryogenic Engineering Conference & International Cryogenic Materials Conference 2016, New Delhi, India.*, 2016.

[4] M. M. Farid, A. M. Khudhair, S. A. K. Razack, and S. Al-Hallaj, "A review on phase change energy storage: Materials and applications," *Energy Convers. Manag.*, vol. 45, no. 9–10, pp. 1597–1615, 2004.

[5] A. Gil, M. Medrano, I. Martorell, A. Lazaro, P. Dolado, B. Zalba, and L. F. Cabeza, "State of the art on high temperature thermal energy storage for power generation. Part 1-Concepts, materials and modellization," *Renew. Sustain. Energy Rev.*, vol. 14, no. 1, pp. 31–55, 2010.

[6] B. Zalba, J. M. Marín, L. F. Cabeza, and H. Mehling, "Review on thermal energy storage with phase change: materials, heat transfer analysis and applications," *Appl. Therm. Eng.*, vol. 23, no. 3, pp. 251–283, Feb. 2003.

[7] U. Herrmann, B. Kelly, and H. Price, "Two-tank molten salt storage for parabolic trough solar power plants," *Energy*, vol. 29, no. 5–6, pp. 883–893, 2004.

[8] T. Wang, "High Themal Energy Storage Density Molten Salts for Parabolic Trough Solar Power Generation," Ph.D. dissertation, The University of Alabama, 2011.

[9] J. Xiao, J. Huang, P. Zhu, C. Wang, and X. Li, "Preparation, characterization and thermal properties of binary nitrate salts/expanded graphite as composite phase change material," *Thermochim. Acta*, vol. 587, pp. 52–58, 2014.

[10] Y. J. Zhao, R. Z. Wang, L. W. Wang, and N. Yu, "Development of highly conductive

KNO3/NaNO3 composite for TES (thermal energy storage)," *Energy*, vol. 70, pp. 272–277, 2014.

[11] Q. Peng, J. Ding, X. Wei, J. Yang, and X. Yang, "The preparation and properties of multi-component molten salts," *Appl. Energy*, vol. 87, no. 9, pp. 2812–2817, 2010.

[12] J. M. Marin, B. Zalba, L. F. Cabeza, and H. Mehling, "Determination of enthalpy temperature curves of phase change materials with the temperature-history method: improvement to temperature dependent properties," *Meas. Sci. Technol.*, vol. 14, no. 2, pp. 184–189, 2003.

[13] B. He, V. Martin, and F. Setterwall, "Phase transition temperature ranges and storage density of paraffin wax phase change materials," *Energy*, vol. 29, no. 11, pp. 1785–1804, Sep. 2004.

[14] M. Koschenz and B. Lehmann, "Development of a thermally activated ceiling panel with PCM for application in lightweight and retrofitted buildings," *Energy Build.*, vol. 36, no. 6, pp. 567–578, 2004.

[15] A. Lázaro, B. Zalba, M. Bobi, C. Castellón, and L. F. Cabeza, "Experimental study on phase change materials and plastics compatibility," *AIChE J.*, vol. 52, no. 2, pp. 804–808, 2006.

[16] J. H. Peck, J.-J. Kim, C. Kang, and H. Hong, "A study of accurate latent heat measurement for a PCM with a low melting temperature using T-history method," *Int. J. Refrig.*, vol. 29, no. 7, pp. 1225–1232, Nov. 2006.

[17] A. F. Regin, S. C. Solanki, and J. S. Saini, "Latent heat thermal energy storage using cylindrical capsule: Numerical and experimental investigations," *Renew. Energy*, vol. 31, no. 13, pp. 2025–2041, 2006.

[18] B. Sandnes and J. Rekstad, "Supercooling salt hydrates: Stored enthalpy as a function of temperature," *Sol. Energy*, vol. 80, no. 5, pp. 616–625, 2006.

[19] M. Yamaha and S. Misaki, "The Evaluation of Peak Shaving by a Thermal Storage System Using Phase-Change Materials in Air Distribution Systems," *HVAC&R Res.*, vol. 12, no. sup3, pp. 861–869, 2006.

[20] B. Flaherty, "Characterisation of waxes by differential scanning calorimetry," *J. Appl. Chem.*

Biotechnol., vol. 21, pp. 144–148, 1971.

[21] C. Giavarini and F. Pochetti, "Characterization of pertroleum products by DSC analysis," *Analysis*, vol. 5, pp. 83–94, 1973.

[22] Y. Zhang and Y. Jiang, "A simple method, the -history method, of determining the heat of fusion, specific heat and thermal conductivity of phase-change materials," *Meas. Sci. Technol.*, vol. 10, no. 3, pp. 201–205, Mar. 1999.

[23] J. Mazo, M. Delgado, A. Lázaro, P. Dolado, C. Peñalosa, J. M. Marin, and B. Zalba, "A theoretical study on the accuracy of the T-history method for enthalpy–temperature curve measurement: analysis of the influence of thermal gradients inside T-history samples," *Meas. Sci. Technol.*, vol. 125001, pp. 1–8, 2015.

[24] C. Rathgeber, H. Schmit, P. Hennemann, and S. Hiebler, "Calibration of a T-History calorimeter to measure enthalpy curves of phase change materials in the temperature range from 40 to 200 °C," *Meas. Sci. Technol.*, vol. 25, no. 3, p. 35011, 2014.

[25] G. Buttitta, G. Serale, and Y. Cascone, "Enthalpy-temperature evaluation of slurry phase change materials with T-history method," *Energy Procedia*, vol. 78, pp. 1877–1882, 2015.

[26] S. Liu, Y. Li, and Y. Zhang, "Mathematical solutions and numerical models employed for the investigations of PCMs' phase transformations," *Renew. Sustain. Energy Rev.*, vol. 33, pp. 659–674, 2014.

[27] N. Shamsundar and E. M. Sparrow, "Analysis of Multidimensional Conduction Phase Change Via the Enthalpy Model," *J. Heat Transfer*, vol. 97, no. 3, p. 333, 1975.

[28] N. Das, Y. Takata, M. Kohno, and S. Harish, "Melting of graphene based phase change nanocomposites in vertical latent heat thermal energy storage unit," *Appl. Therm. Eng.*, vol. 107, pp. 101–113, 2016.

[29] C. Bonacina, G. Comini, A. Fasano, and M. Primicerio, "Numerical solution of phase-change problems," *Int. J. Heat Mass Transf.*, vol. 16, no. 10, pp. 1825–1832, 1973.

[30] G. Comini, S. Del Guidice, R. W. Lewis, and O. C. Zienkiewicz, "Finite element solution of non-linear heat conduction problems with special reference to phase change," *Int. J. num. Meth. Engng.*, vol. 8, no. 3, pp. 613–624, 1974.

[31] Q. He and W. N. Zhang, "a Study on Latent Heat Storage Exchangers With the High Temperature Pcm," *World Renew. Energy Congr. VI*, no. January 2000, pp. 1044–1047, 2000.

[32] J. Buschle, W. D. Steinmann, and R. Tamme, "Analysis of steam storage systems using Modelica," *Aerospace*, pp. 235–242, 2006.

[33] Z. X. Gong and A. S. Mujumdar, "Cyclic heat transfer in a novel storage unit of multiple phase change materials," *Appl. Therm. Eng.*, vol. 16, no. 10, pp. 807–815, 1996.

[34] H. Cui, X. Hou, and X. Yuan, "Energy analysis of space solar dynamic heat receivers," *Sol. Energy*, vol. 74, no. 4, pp. 303–308, 2003.

[35] H. Cui, Y. Xing, Y. Guo, Z. Wang, H. Cui, and X. Yuan, "Numerical simulation and experiment investigation on unit heat exchange tube for solar heat receiver," *Sol. Energy*, vol. 82, no. 12, pp. 1229–1234, 2008.

[36] C. Guo and W. Zhang, "Numerical simulation and parametric study on new type of high temperature latent heat thermal energy storage system," *Energy Convers. Manag.*, vol. 49, no. 5, pp. 919–927, 2008.

[37] B. Yimer and M. Adami, "Parametric study of phase change thermal energy storage systems for space application," *Energy Convers. Manag.*, vol. 38, no. 3, pp. 253–262, 1997.

[38] M. J. Kabbara and N. B. Abdallah, "Experimental Investigation on Phase Change Material based Thermal Energy Storage Unit," *Procedia Comput. Sci.*, vol. 19, no. Seit, pp. 694–701, 2013.

[39] Y. Zhang, K. Du, M. a. Medina, and J. He, "An experimental method for validating transient heat transfermathematical models used for phase change materials(PCMs) calculations," *Phase Transitions*, vol. 87, no. 6, pp. 541–558, 2014.

[40] S. Thapa, S. Chukwu, A. Khaliq, and L. Weiss, "Fabrication and analysis of small-scale thermal

energy storage with conductivity enhancement," *Energy Convers. Manag.*, vol. 79, pp. 161–170, 2014.

[41] F. Kuznik, J. Virgone, and R. Reisdorf, "Experimental investigation of thermal behaviour of phase change materials under dynamic thermal effects," 2006. [Online]. Available: http://www.aivc.org/resource/experimental-investigation-thermal-behaviour-phase-change-materials-under-dynamical-thermal.

[42] D. Kearney, U. Herrmann, P. Nava, B. Kelly, R. Mahoney, J. Pacheco, R. Cable, N. Potrovitza, D. Blake, and H. Price, "Assessment of a molten salt heat transfer fluid in a parabolic trough solar field," *J. Sol. Energy Eng. Trans. ASME*, vol. 125, no. 2, pp. 170–176, 2003.

[43] D. A. Brosseau, P. F. Hlava, and M. J. Kelly, "Testing Thermocline Filler Materials and Molten - Salt Heat Transfer Fluids for Thermal Energy Storage Systems Used in Parabolic Trough Solar Power Plants," *Sol. Energy Eng-Trans ASME*, vol. 127, no. 127, pp. 109–16, 2005.

[44] NETZSCH Co., "Potassium Nitrate — Phase Transitions." [Online]. Available: https://www.netzsch-thermal-analysis.com/en/materials-applications/organics/potassium-nitrate-phase-transitions/.

[45] G. J. Janz, U. Krebs, H. F. Siegenthaler, and R. P. T. Tomkins, "Molten Salts: Volume 3 Nitrates, Nitrites, and Mixtures: Electrical Conductance, Density, Viscosity, and Surface Tension Data," *J. Phys. Chem. Ref. Data*, vol. 1, no. 3, pp. 581–746, 1972.

[46] X. Zhang, K. Xu, and Y. Gao, "The phase diagram of LiNO3 – KNO3," *Thermochim. Acta*, vol. 385, pp. 81–84, 2002.

[47] A. Bejan, *Convection heat transfer, Fourth Edition*. John Wiley & Sons, Ltd, 2013.

[48] A. Solé, L. Miró, C. Barreneche, I. Martorell, and L. F. Cabeza, "Review of the T -history method to determine thermophysical properties of phase change materials (PCM)," *Renew. Sustain. Energy Rev.*, vol. 26, pp. 425–436, 2013.

Appendix A: The Phase Diagram for The $LiNO_3$-KNO_3 System

Figure A-1 presents the phase diagram for the $LiNO_3$-KNO_3 system in the literature [46]. While Figure A-2 shows the DSC curve of KNO_3 in literature [44].

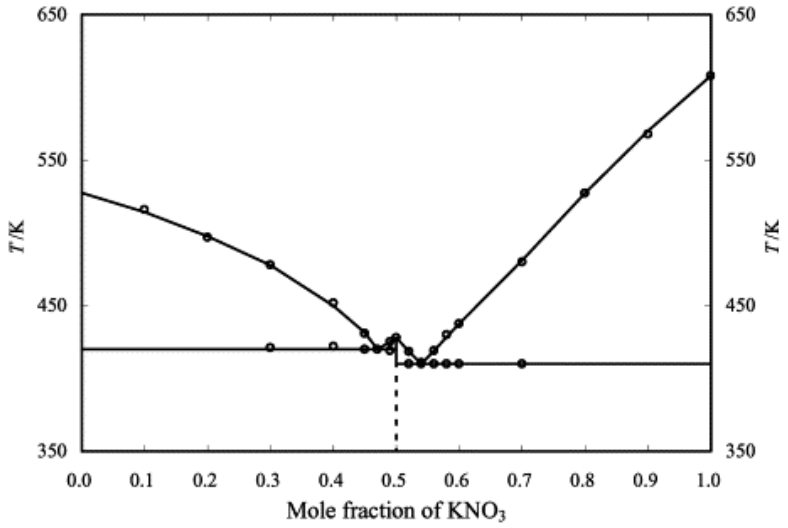

Figure A-1: The phase diagram for the $LiNO_3$-KNO_3 system [46]

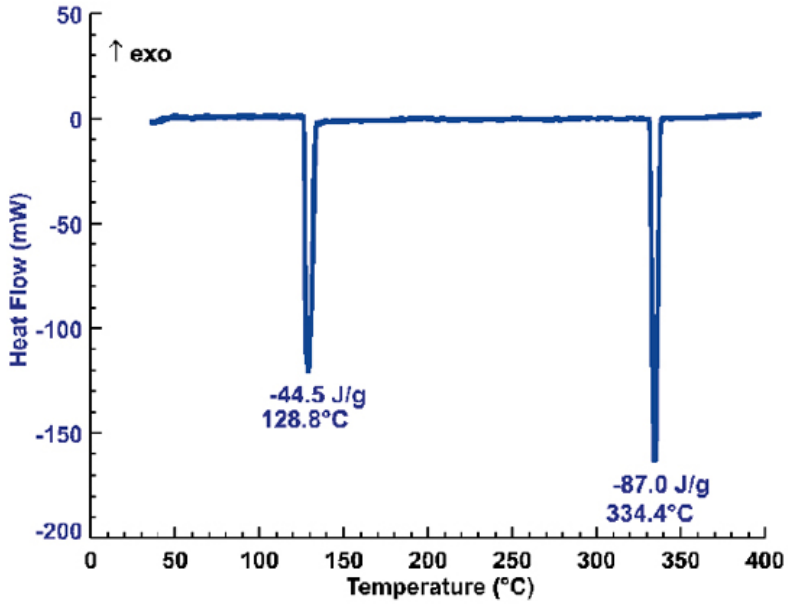

Figure A-2: DSC curve measured in literature [44]

Appendix B: T-History Experiments for 0.5 KNO_3 and 0.6 KNO_3

The another four cycles of T-history experiments for the 0.5 KNO_3 and the 0.6 KNO_3 are presented in Figures B-1 and B-2. While the Figure B-3 shows the cooling curve for the 0.5 KNO_3.Table B-1 shows the comparison of the latent heat results achieved from both the T-history experiment and the DSC test.

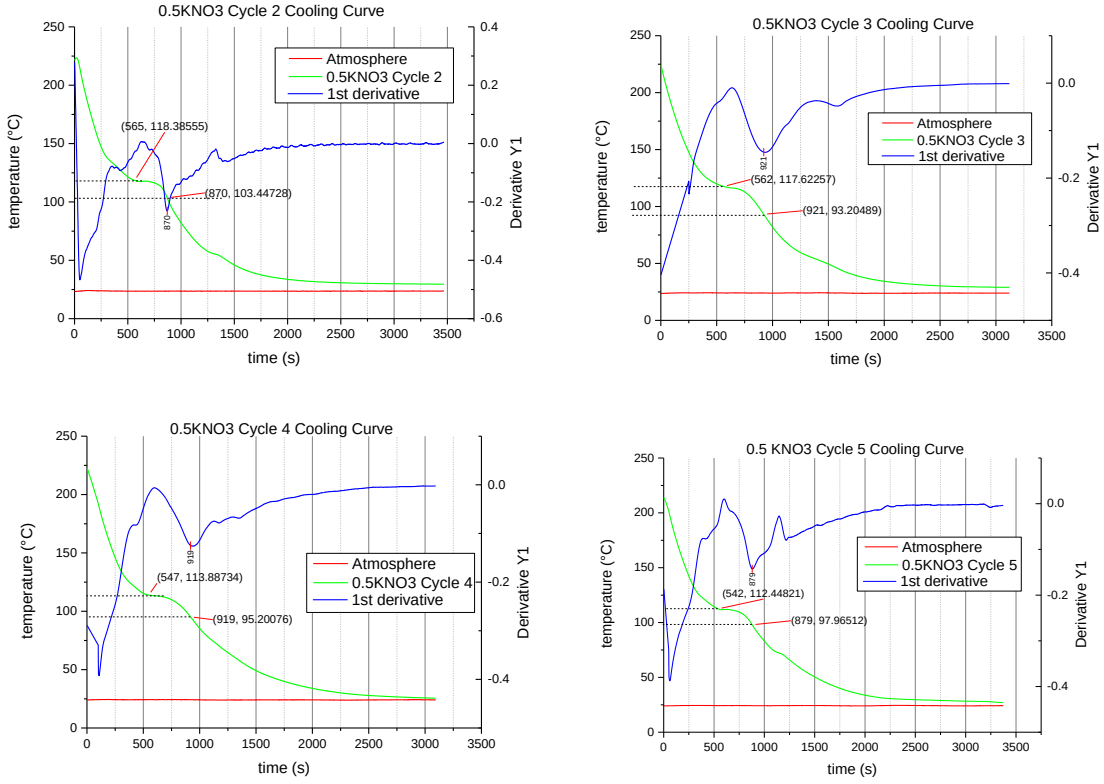

Figure B-1: Cycle 2 to cycle 5 of the T-history experiments for KNO_3

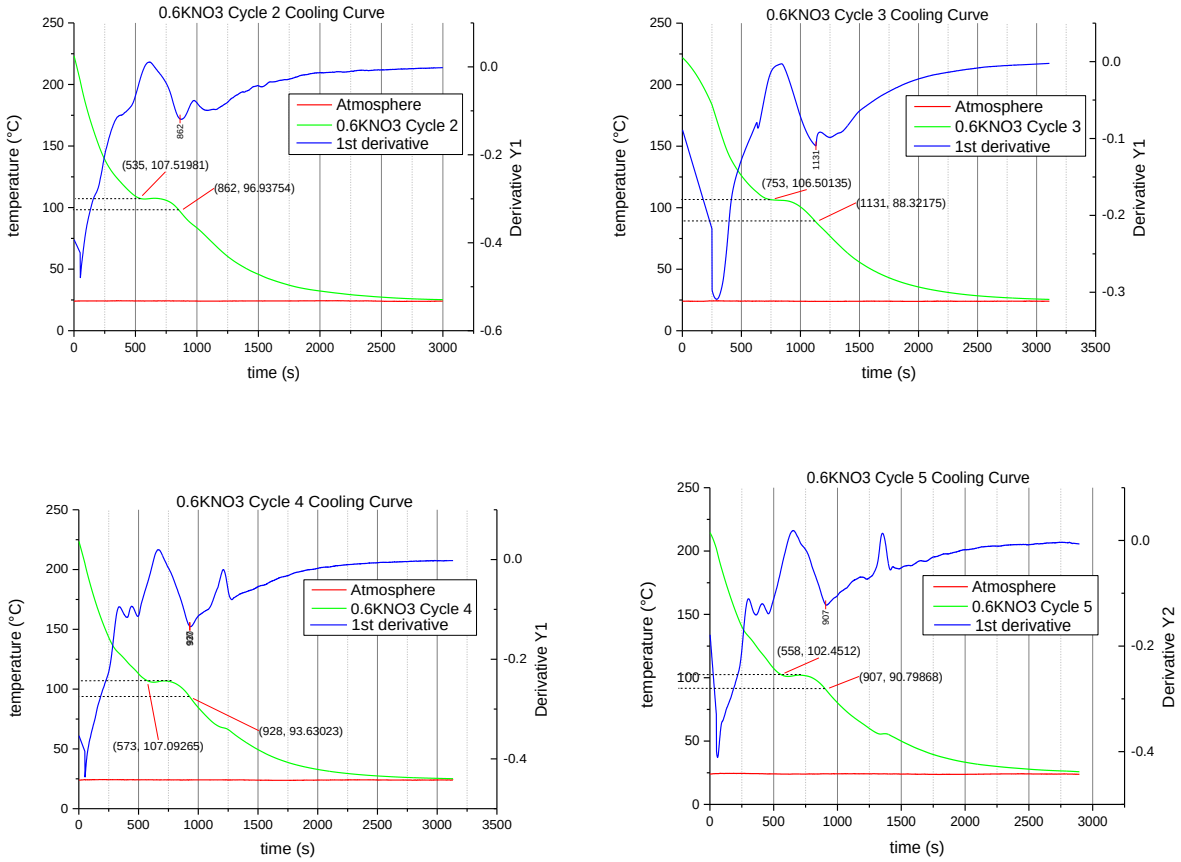

Figure B-2: The cycle 2 to cycle 5 of the T-history experiments for 0.6 KNO_3

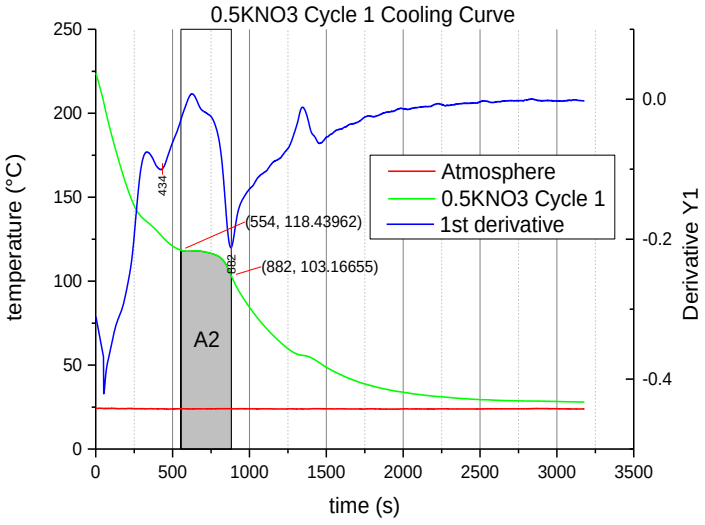

Figure B-3: The cooling curve for 0.5KNO_3

Table B-1: The heat of fusion comparison

Test Cycle	Heat of Fusion (kJ/kg)
1	86.14
2	80.46
3	88.91
4	89.77
5	81.84
Average	85.43
DSC's Result	118.68

Table B-2: Measured thermophysical properties of paraffin during the thermal cycle test [1]

No. of cycles	Melting temperature /°C	Latent heat of fusion /J·g^{-1}
0	52.9	133.66
100	52.2	122.49
500	49.6	146.80
1000	50.0	125.06
1500	50.3	114.66

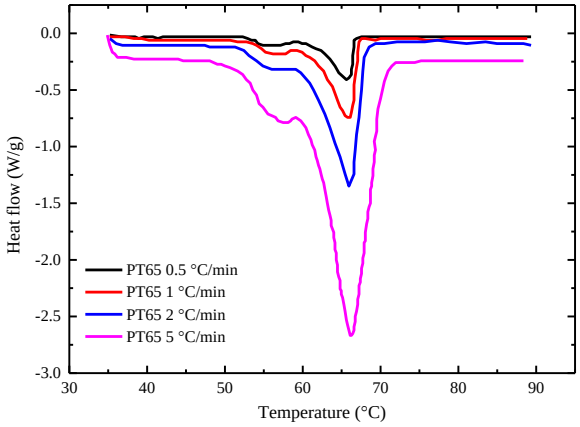

Figure B-4: The effect of heating rates on DSC measurements [2]

Table B-3 Thermocouple (T.C.) calibration results

Standard T.C. Average Reading (℃)	Test T.C. 1 (℃)	Test T.C. 2 (℃)	Test T.C. 3 (℃)
29.96	29.81	29.64	29.57
44.87	44.51	44.80	44.10
59.86	59.72	59.07	59.11
75.19	74.66	74.65	74.23
89.97	89.40	89.94	89.12
74.91	74.28	74.80	74.77
61.12	60.4	60.74	61.78
45.58	44.93	44.70	45.89
30.31	29.37	29.84	30.69
Error	±0.94	±0.87	±0.96

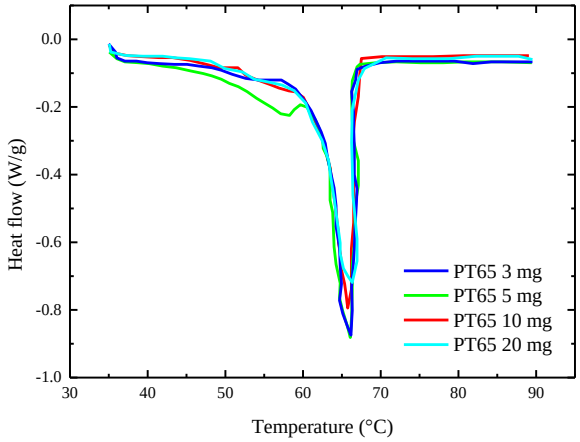

Figure B-5: The effect of sample mass on DSC measurements [2]